J/ψ Production in d+Au and p+p Collisions at $\sqrt{s} = 200$ GeV

Dong Jo Kim

The Graduate School
Yonsei University
Institute of Physics and Applied Physics

J/ψ Production in d+Au and p+p Collisions at $\sqrt{s} = 200$ GeV

A Dissertation
Submitted to the Department of Physics
and the Graduate School of Yonsei University
in partial fulfillment of the
requirements for the degree of
Doctor of Philosophy

Dong Jo Kim

June 2004

This certifies that the dissertation of Dong Jo Kim is approved.

Thesis Supervisor: Ju Hwan Kang

Young Joon Kwon

Su Houng Lee

Koan Sik Joo

Il Hung Park

The Graduate School

Yonsei University

June 2004

Acknowledgements

I would like to first gratefully acknowledge my adviser Professor Ju.Kang, for his guidance and support in the work leading up to this dissertation. I acknowledge the dissertation committee for their contribution of this manuscripts. It was so fortunate to be a collaborator of the PHENIX Experiment in RHIC since 1998. I finished my researches as a member of the Heavy-Ion Research Group in BNL and Yonsei, participating in PHENIX muon arm construction and analysis with world-wide PHENIX collaborations. I worked on the muon arm detector construction (hardware and software development for wire-tension measurement and wire-winding) during the master course and software development(calibration database and cluster-fitting improvement) in the beginning of the Ph.D course. While I was staying at BNL since RHIC run3(2002-2003) running, even though I worked on the muon analysis, I worked as a PHENIX calibration specialist dring run3 d+Au data-taking period and a PHENIX calibration Manager to get all the subsystem calibrations done during the run3 p+p period. Also I was a active member of the PHENIX production(Data reconstruction) team after the run3 data-taking, all PHENIX analyzers used the outcome from that production. Those kinds of the contributions to the PHENIX collaboration were really appreciated by the collaboration, by doing this I was also able to enhance my analysis skills and understanding of most of the PHENIX subsystems. I really appreciated Tom Hemmick and Jan Rak to give me such a valuable opportunity. I thank PHENIX muon people for their valuable work especially Michael J. Leitch(LANL), Melynda Brooks(LANL), Raphael Granier de Cassagnac(LLR-Ecole Polytechnique), Vince Cianciolo(ORNL), Patrick L. McGaughey(LANL) , David M Lee(LANL), David Silvermyr(ORNL), James L. Nagle(Univ. of Colorado), Hiroki Sato(Kyoto Univ.), MinJung Kweon(Korea Univ.), Xiaorong Wang(Georgia State Univ) and other PHENIX members. I acknowledge all the members in Yonsei Nuclear physics Lab. who always were supportive of all my activities.

Finally I thank my families and God who encouraged and supported me with their endless concern and love.

ABSTRACT

J/ψ Production in d+Au and p+p Collisions at $\sqrt{s} = 200$ GeV

DongJo Kim
Institute of Physics and Applied Physics
The Graduate School
Yonsei University

The J/ψ measurements from RHIC have been made at $\sqrt{s} = 200$ GeV in both p+p and d+Au collisions. J/ψs have been clearly identified through their dilepton decay in four spectrometers of the PHENIX experiment: two central arms covering the mid-rapidity region of $|\eta| < 0.35$ and two forward muon arms. The vertex and the event centrality are measured by beam-beam counters lying at $3 < |\eta| < 3.9$. Details of the muon channel measurements are presented based upon a 2.74nb^{-1} d+Au and 350 nb^{-1} p+p integrated luminosity obtained in the third run period at RHIC(2003).

The transverse momentum distributions above 2 GeV/c from p+p collision are reasonably well described by the color-octant model(COM). The average transverse momentum of the J/ψ's, $\langle p_T \rangle$ values of 1.85 $\pm$ 0.46(stat) $\pm$ 0.16(sys) GeV/c (central arm) and 1.78 $\pm$ 0.27(stat) $\pm$ 0.16(sys) GeV/c (muon arm), with a combined value of 1.80 $\pm$ 0.23(stat) $\pm$ 0.16(sys) GeV/c are obtained in p+p collisions.

The differential cross sections have been extracted from both muon and electron channel measurements and the total cross section $\sigma_{J/\psi} = 3.99 \pm 0.61$(stat) $\pm$ 0.58(sys) $\pm$ 0.40(abs) μb has been extracted by fitting both measurements in p+p collisions. The rapidity distribution shape is consistent with most of the available PDF(Parton Distribution Function)s. COM

calculations are able to reproduce the $\sqrt{s}$ dependence of the cross section using color octet matrix elements with a reasonable choice of QCD parameters.

The ratio of J/ψ production in d+Au collisions to p+p collisions as a function of rapidity is extracted and it shows consistency with shadowing at low x and less suppression at larger x and the p_T differential cross section distributions exhibit broadening which is comparable with the results from the lower energy experiment [18].

At forward rapidity (small x values in the gold nucleus, or the shadowing region), no strong centrality dependence is observed, while a strong enhancement from peripheral to central collisions is observed at backward rapidity. The theoretical calculations [19] with different amounts of inhomogeneous shadowing and antishadowing at these rapidities show that the predictions are qualitatively consistent with the data at forward rapidity, while they do not show the observed steep rising shape at backward rapidity.

Key Words: J/ψ, RHIC, PHENIX, Color-octant model, Shadowing

Contents

List of Figures

List of Tables

Chapter 1

Introduction

The production of J/ψ 's has been of great interest to the heavy ion community since Matsui and Satz originally predicted that the suppression of J/ψ production in heavy ion collisions could be a signature of quark gluon plasma(QGP) formation [1]. The interest continued to remain high as the NA50 collaboration produced the first J/ψ measurements in heavy ion collisions which seemed to show a significant suppression in central collision [2].

Since those measurements became available, there have been theoretical calculations with and without QGP formation which have been able to match the NA50 results, high-lightening the difficulty of making an absolute statement of QGP existence or not. Given the uncertainty of the interpretation of the data, the heavy ion community has anxiously awaited data from RHIC to see what J/ψ production will tell us. The first results from Au+Au collision in Run2 from the PHENIX collaboration [78] did not have enough statistics to distinguish among various production models which predicted everything from suppression to modest or large enhancement.

In order to determine whether J/ψ production in heavy ion collision is different from the production in the absence of QGP, it is critical to have a solid baseline from p+p and p+A (or d+A) collisions to constrain the effects already present for cold nuclear matter. Previous studies at lower energy [2] which have claimed to see QGP relied heavily on such a baseline. Clearly this baseline measurement is also essential at RHIC. In addition to their connection to A+A physics, p+A measurement is crucial to understand

cold nuclear matter effects such as gluon shadowing, transverse momentum broadening, parton energy loss or absorption.

1.1 Heavy ion physics

Since the discovery of quarks in the 1960s, the core questions in nuclear and particle physics have evolved dramatically. The nucleus had long been viewed as a densely packed assembly of neutrons and protons bound together by a strong force carried by pions and other mesons. We now understand that these "elementary" particles are themselves made up of more fundamental point-like constituents: quarks (and anti-quarks) bound together through interactions mediated by gluons. Quantum chromodynamics (QCD), the current theory of the strong interactions, is a field theory of quarks and gluons. It forbids the appearance of free quarks or gluons, but their existence is taken to play a fundamental role in the nature of matter. Protons, neutrons, pions, and the elaborate array of other hadrons discovered in the last half-century are thought to be understood in terms of their constituent quarks and gluons. But at extremely high energy densities, QCD predicts a new form of matter, consisting of an extended volume of interacting quarks, anti-quarks, and gluons. This is the quark-gluon plasma (QGP). It is predicted to come into existence at temperatures and densities more extreme than any we know of in the present natural universe. Such extreme conditions, however, are thought to have existed a few microseconds after the Big Bang. Up to now the experiments(see table 1.1) at CERN and BNL have tried to create the QGP in the highest-energy collisions of heavy nuclei ever achieved under laboratory conditions. The scrutiny of this new state of matter might answer some of the key questions of nuclear and particle physics.

Getting clear and unambiguous experimental evidences for QGP formation is a difficult task. The main problem is that even if the QGP is formed in a laboratory experiment, it is an extremely short-lived state, which quickly turns into normal matter through the inverse hadronization phase transition. The observables which have been proposed in relativistic heavy-ion collisions are discussed briefly in the following section1.1.2.

Site	Accelerator	Type	Start	p[AGeV/c]	beam	$\sqrt{s}$[GeV/A]
BNL	AGS	fixed target	1986 1992	14.5 1.8-11.5	Si Au	5.4 2.3-4.8
CERN	SPS	fixed target	1986 1994	200 158	S,O Pb	19 17
BNL	RHIC	collider	2000	30-100	Au	60-200
CERN	LHC	collider	2007	2700	Pb	5400

Table 1.1 Table of different accelerators in ultra-relativistic heavy-ion collisions and their characteristics: p is the momentum of a nucleon inside a nucleus(in the laboratory frame), and $\sqrt{s}$ is the energy per nucleon in the center-of-mass frame of the nucleus-nucleus collision.

1.1.1 Deconfinement

Quantum-ChromoDynamics(QCD), the fundamental theory of strong interactions, describes hadronic matter as an ensemble of quarks and anti-quarks confined inside hadrons and interacting through gluon exchange. Gluons own null mass and a colour charge, and are associated with the local colour symmetry $SU(3)$. The interaction among two coloured particles is characterized by the coupling constant for strong interactions

$$\alpha_s(Q^2) = \frac{12\pi}{(33-2f)ln(\frac{Q^2}{\lambda^2_{QCD}})} \tag{1.1}$$

where f is the number of flavours and $\lambda_{QCD} \sim 200MeV$ is the scale of the QCD. The coupling constant increases with growing transferred momentum Q(inversely proportional to the distance between the constituent quarks $r \sim \frac{1}{Q}$). For this reason, in ordinary matter quarks are confined inside hadrons. By contrast, at very short distances, quarks and gluons act as nearly free particles(asymptotic freedom).

Fig 1.1 shows the energy density as a function of temperature as calculated from Lattice QCD [27]. Current calculation indicate that the transition happens around a critical temperature $T_c = 150 - 180MeV$, which corresponds to an energy density about 0.3-1.01 GeV/fm^3 [4, 27]. Calculations indicate a significant change in behavior of the system over a small change in temperature including restoration of a approximate chiral symmetry. As the temperature exceeds the critical temperature T_c, the quark

binding potential deviates from the vacuum potential and decrease to zero, indicating that the interaction among partons becomes very weak above the critical temperature.

1.1.2 QGP signatures

Even if the QGP is produced in a laboratory experiment, its identification is difficult because of its short lifetime(order of $10^{-32}s$). It would be interesting to directly access to the thermodynamic variables of the system during the collision, but this is experimentally impossible. Hence we have to rely on indirect measurements of QGP formation. A clear signature of the transition from ordinary matter to a deconfined medium must allow to establish if the medium is deconfined or not. Furthermore it must be present in the early phase of the transition and keep its information through the system evolution until its detection. The observables in relativistic heavy-ion collisions can be divided into three classes which are discussed in the reference [6]: hard, electromagnetic and soft probes.

- Hard probes provide a direct test of colour deconfinement in nuclear collisions because they are created early in the collision, and due to the finite size of the reaction fireball and their relatively small reinteraction cross section, they decouple early. The dissociation pattern of quarkmonia and the energy loss of hard jets depend on the confinement status of the medium in question: in both cases, this is based essentially on the hardening of gluons no longer confined to hadrons. Since J/ψ dissociation requires hard gluons, the anomalous J/ψ suppression recently observed in Pb-Pb collisions could be a first indication of deconfinement [2].

- Electromagnetic probes, in particular low mass dileptons, can be used as direct test for in-medium changes of hadron properties. Such modifications are expected at the onset of chiral symmetry restoration and thus constitute a way to address this aspect of the quark-hadron transition. The presently observed low-mass dilepton enhancement could be a first instance of such an effect for the ρ; however, an alterna-

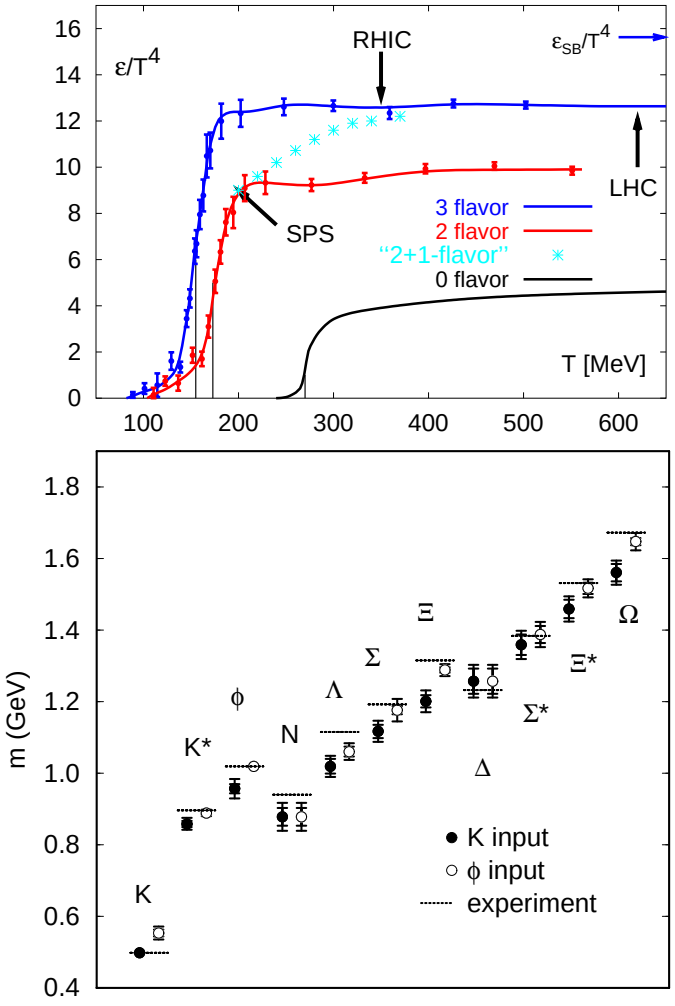

Figure 1.1 Lattice QCD results for the energy density ε/T^4 as a function of the temperature (MeV)(top). Note the arrow on the right side indicating the level for the Stefan-Boltzmann limiting case. Hadronic masses calculated via lattice QCD compared with the experimentally determined spectra.(bottom)

tive explanation through interaction broadening of the ρ-width so far remains also tenable.

- Soft probes test equilibration and the presence of collective effects at freeze-out, i.e., at the end of the strong interaction. They are related to signals produced in physical processes with small momentum transfer. They appear when the density of the medium has dropped enough to allow the existence of hadrons, that is in the hadronic final stage of the system evolution. Nevertheless they can also provide indirect information on the earlier(deconfined) stages of the collision. Recent studies of hadron abundances are in quite good agreement with a composition as given by a thermal resonance gas; so far, however, some strangeness suppression still remains. The broadening of transverse momentum spectra observed in p-A and A-B collisions agree well with random walk rotations of the collision axis [17]. Species equilibration as well as p_T-broadening in nuclear collisions do not seem understandable in simple hadronic terms; however, a consistent partonic description is also still lacking.

1.1.3 The evolution of the medium

The evolution of the medium created in relativistic heavy-ion collisions may be viewed as evolving through the following stages as shown by the space-time diagram with the longitudinal coordinate z and the time coordinate t, as shown in Fig 1.2 according to the model proposed by Bjorken.

1. In the first instants($\tau \leq 1fm/c$) a lot of collisions among partons give rise of a big number of quarks and gluons.

2. The gas of quarks and gluons evolves to the point of thermodynamic equilibrium: this is the QGP phase(its duration is estimated to be of the order of some fm/c).

3. In the mixed phase the system expands, because of the high plasma pressure, with the consequent temperature drop: some quarks combine again and form hadrons. Plasma of quarks, gluons and hadronic gas coexist in this phase, which last about 10 fm/c.

4. As the temperature decreases, the hadron formation prevails once more(phase of interacting hadronic gas).

5. At the freeze-out point hadrons decouple and, as free particles, leave the collision region($\tau \sim 20 - 30 fm/c$).

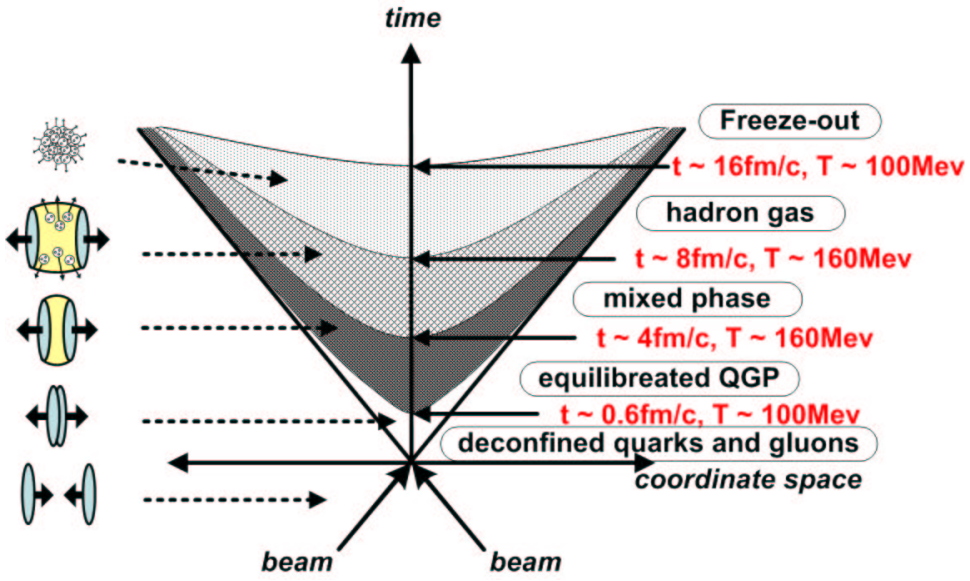

Figure 1.2 Space-time picture of a central nucleus-nucleus collision according to the Bjorken model. The times and temperatures for different phase are taken from [5]

1.1.4 The Energy Density

A basic requirement to drive the QCD transition and create QGP is to have a sufficient energy density available. From the lattice description, the required density is the order of 1 GeV/fm^3. Establishing that this density is created in the collision systems(SPS or RHIC) is an important step to study the creation of QGP.

The Bjorken model

The ions used in heavy-ion collisions are ultra-relativistic objects, and they are subjected to the Lorentz contraction whose factor is about 10 at 200GeV/c per nucleon. According to the Bjorken calculations [8], at very high energies, ions are partially transparent. Immediately after the collision, we can distinguish two so called "fragmentation" regions, one corresponding to the target, the other one to the projectile.

These two regions surround a central rapidity region, very excited, where many of the particles produced in the collision are emitted from. It is inside this region that the plasma of quarks and gluons can more likely appear. The space-time evolution of the collision has been studied by Bjorken. This description makes use of an hydrodynamic model with the following assumptions:

- the energy of the collision is high enough to generate a plateau in the rapidity distribution of the produced particles in the central rapidity region: $dN/dy = constant$.
- the baryonic number is zero in the central rapidity region, i.e. the total baryonic number is concentrated in the fragmentation regions.

According to the Bjorken model, the initial energy density released during the collision is estimated by [8] :

$$\epsilon = \frac{1}{S_\perp \tau_0}(\frac{dE_T}{dy})_{y=0} \tag{1.2}$$

where $S_\perp$ is the transverse intersecting area of the two nuclei in the collision, $\tau \approx 1 fm/c$ is the proper time of the plasma formation, $\lfloor \frac{dE_T}{dy} \rfloor_{y=0}$ is the total transverse energy of the particles produced per rapidity unit around $y_{cm} = 0$. The energy density estimated in this way for central Pb-Pb collisions at 158AGeV/c is $3.2 \pm 0.3 GeV/fm^3$ [9]. This value is comparable to the one determined by QCD calculation for the plasma existence conditions [10].

1.1.5 Collision Geometry and Centrality

Collision Geometry

A basic concept of the Glauber model and some variables which were used to determine the centrality at the PHENIX experiment will be shown in several correlation plots. To get a simple picture of the relation between the model calculation and physical observable from the PHENIX BBC and ZDC detector, the Fig.1.5 shows the charged particle's correlation in the BBC and ZDC from p-p to Au-Au collision. Details of the PEHNIX centrality determination in d+Au collision is described in Appendix C.

Glauber model of nucleus-nucleus collisions

The galuber model [11] provides a quantitative geometrical description of nucleus-nucleus collisions, treated as a superposition of nucleo-nucleon collisions. The projectile nucleons traverse the target nucleus following straight line trajectories and undergoing several collisions with the nucleons of the target. The only physical inputs are the elementary nucleon-nucleon inelastic cross-section and the density distribution inside the nuclei.

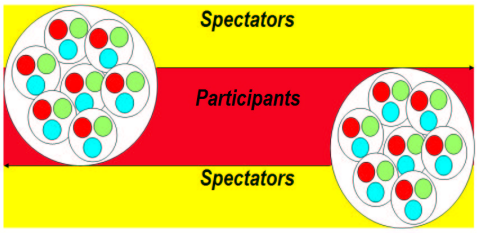

Figure 1.3 A geometric illustration of nuclear collision.

The Galuber model assumes that the basic nucleon-nucleon cross-section is the same throughout the passage of a nucleon. After a collision, a struck nucleon may become excited and subsequently interact with other nucleons with a different cross-section. The total nucleon-nucleon cross-section in the range 3GeV $< \sqrt{s} <$ 100 GeV is approximately 40mb, and the inelastic part is about 30mb. A small fraction of the inelastic cross-section ($\sim$ 6%) is due

to diffractive dissociation processes. Since elastic or diffractive dissociation collisions lead to a small loss of energy, a nucleon suffering elastic or diffractive collisions can be treated as undergoing no collision at all. Therefore only non-diffractive inelastic collisions are considered and it is assumed σ_{in} = 30 mb.

The density distribution ρ inside the nuclei is assumed to follow a Woods-Saxon distribution:

$$\rho(r) = \frac{\rho_0}{1 + e^{\frac{r-R}{a}}} \tag{1.3}$$

with

$$r = (1.12A^{1/3} - 0.86A^{-1/3})fm, \rho_0 = 0.169/fm^3, a = 0.54fm \tag{1.4}$$

where r is the distance from the center of the nucleus. R is 6.40fm for a Au nucleus which is very close to 6.38fm, the measured value from eA scattering[ref]. "a" is called the diffusivity, and controls the thickness of the nucleus skin. The density profile for a Au nucleus is shown in Fig 1.4. The integral $\int_0^\infty \rho(r)4\pi r^2 dr = 197$, is the total number of nucleons in a Au nucleus.

There are several general aspects regarding relativistic nucleus-nucleus collisions which are worth to point out. First, due to the large size of the nucleus multiple scattering occur so that a nucleon in one nucleus may collide with many nucleons in the other nucleus. In this process an enhanced fraction of the initial energy carried by nucleons is deposited in the collision region. Meanwhile, nucleons lose energy and slow down. Second, only the nucleons in the overlapped region of the two nuclei participate in the collisions. These nucleons are usually called "participants" or "wounded nucleons", the rest that do not participate in the collision are called "spectators". The overlap region has a preferred direction, which is represented by the vector that connects the centers of the nuclei. The magnitude of the vector is referred as the "impact parameter", which controls the size of the overlap region and the number of participants and represents the centrality of the collision. The plane defined by the beam axis(z) and $\vec{b}$ is called "reaction plane", which represents the relative orientation of the colliding nuclei.

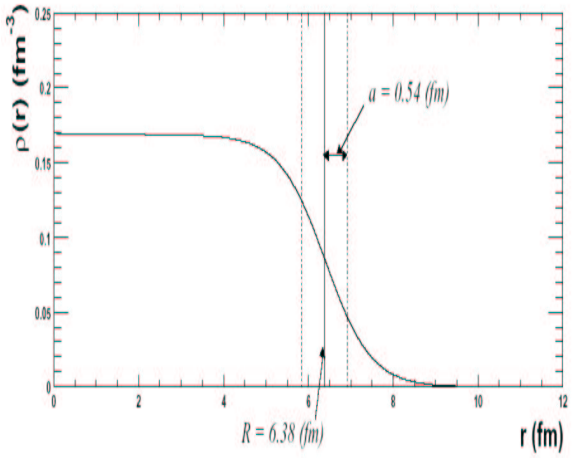

Figure 1.4 Woods-Saxon nuclear density profile for a Au nucleus as a function of the distance r from the nucleus center

Centrality

The dependence of multiplicity upon the number of participants can be established by selecting different centrality cuts. The results is shown in Fig.1.1.5; one can see that the multiplicity per participant pair increases with centrality, but not quite as fast as it would if the NN collisions were independent. If we decompose the multiplicity measured in NN collisions at some energy $\sqrt{s}$ into a fraction $X(s)$ coming from "hard" processes, and the remaining fraction $1-X(s)$ coming from "soft" processes, and assume that in nuclear collisions "hard" processes are incoherent and thus scale with the number of collisions, whereas "soft" processes scale with the number of participants [14], we come to the following simple parameterization [16]

$$\frac{dn_{AA}}{d\eta} = [(1-X(s)) < N_{part} > + X(s) < N_{coll} >] \frac{dn_{NN}}{d\eta} \qquad (1.5)$$

which describe the data quite well. In the framework of perturbative QCD approach, one has to assume that the coefficient $X(s)$ is proportional to the mini-jet production cross section, and thus grows with energy reflecting the

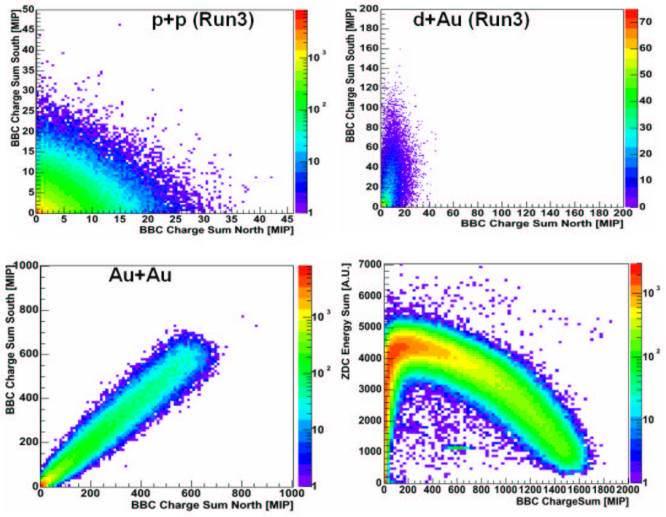

Figure 1.5 Typical BBC charge sum and ZDC energy from the different collision system ; p+p(top left), d+Au(top right), ,Au+Au(bottom left : BBC south and north charge sum), Au+Au(bottom right:BBC charge sum and ZDC energy sum)

growth of the parton distributions at small Bjorken x, X(s) $\sim [xG(x)]^2$, with $x \sim 1/\sqrt{s}$. Therefore one expects [64] that the centrality dependence should become increasingly steep as the $\sqrt{s}$ increases. This increase is not seen in Fig1.1.5, which in the lower panel shows that the ratio of the distributions at $\sqrt{s} = 200GeV$ and $\sqrt{s} = 130GeV$ is consistent within error bars. The almost constant ratio appears consistent with the prediction [15, 16] based on the ideas of parton saturation, where the increase of multiplicity stems from the running of the QCD coupling constant determining the occupation number $\sim 1/\alpha_s$ of gluons in the classical field.

The centrality dependence of charged hadron multiplicity at various RHIC injection energy shown in Fig1.8.

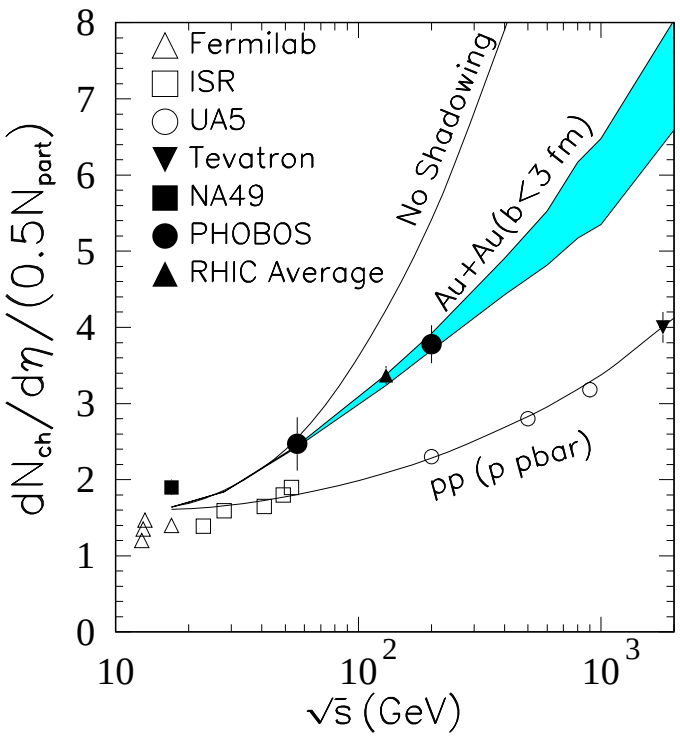

Figure 1.6 The multiplicity as a function of energy for heavy ions and for $p\bar{p}$. Figure from Li and Wang [63] showing the expected rise (the "No Shadowing" line) in multiplicity per participating nucleon pair with increasing beam energy, compared to the data observed at RHIC. The shaded band is a pQCD calculation which invokes substantial nuclear shadowing of gluons in order to reduce the multiplicity to match the data.

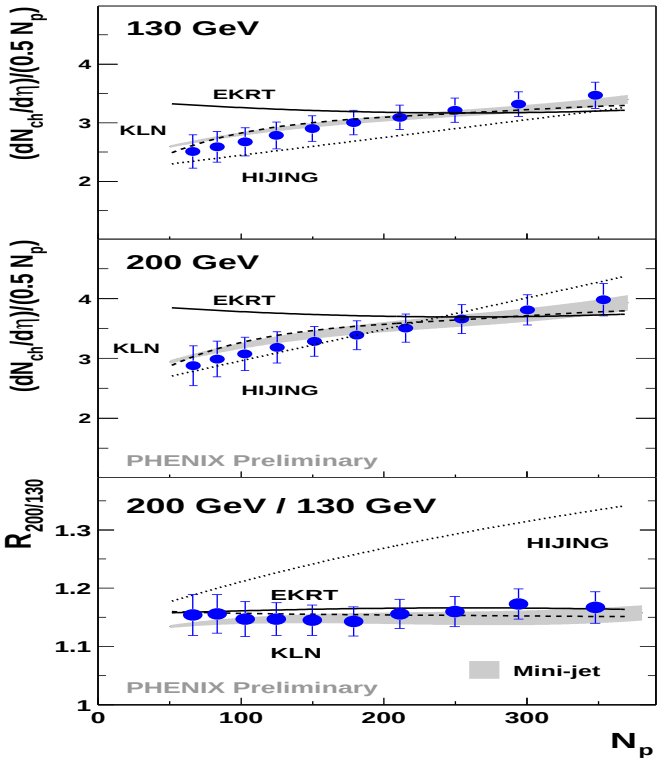

Figure 1.7 Multiplicity per participant nucleon pair, as a function of centrality, for $\sqrt{s_{NN}}$ =130 GeV and 200 GeV Au+Au collisions as measured in PHENIX; compared to theoretical predictions available in 2002. "HIJING" is a pQCD-based model [67], while "KLN" features gluon saturation in the initial state [68]; "EKRT" assumes saturation in the final state [69, 70].

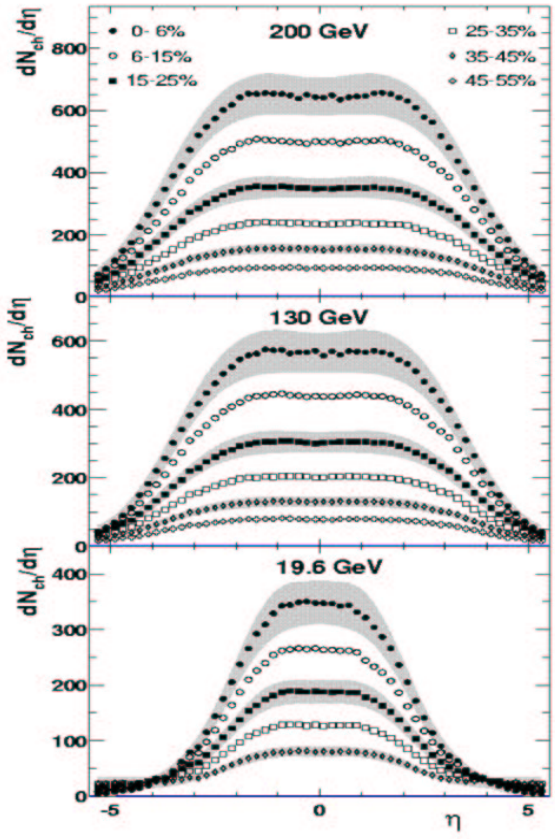

Figure 1.8 Pseudo-rapidity distributions of charged particles from AuAu collisions at various energy(PHOBOS collaboration)

1.1.6 J/ψ suppression

Several signals has been proposed as signatures of the formation of a deconfined state of matter in heavy ion collisions. In particular, Matsui and Satz [1] predicted that the formation of QGP would screen the colour binding potential, preventing the c and $\bar{c}$ quarks to form charmonia states and therefore leading to a measurable suppression of the J/ψ yield.

The signature is particularly interesting because the $c\bar{c}$ states, composed of heavy quarks, can only be produced at the earliest stages in the collision evolution, from hard processes which happen early enough to prove the formation of QGP. A hadron placed into a deconfined medium will dissolve into its quark constituents. If the medium expands, cools off and eventually hadronizes, normal hadrons will now reappear and, in case of an expansion in thermal equilibrium, not carry any information about the earlier stages. But the situation for a J/ψ is quite different in QGP. The J/ψ is a bound stage of the heavy c and $\bar{c}$ quark , which each have a mass of about 1.5GeV. The J/ψ has a mass of about 3.1 GeV; with a radius of about 0.3fm it is much smaller that the usual light hadrons. It has a binding energy of about 0.64GeV, which is much larger than the typical hadronic scale $\lambda_{QCD} \simeq 0.2GeV$. The J/ψ is produced quite rarely in hadronic collisions at present energies, in about one out of 10^5 events. However through its decay into dimuons, it is rather easily detectable in suitably triggered experiments. If the QGP is sufficiently hot, a J/ψ will also melt in it. However, its constituents, the c and the $\bar{c}$ now separate and never meet again. Since the production of more than one $c\bar{c}$ pair per collision is very strongly excluded, the c must combine with a normal antiquark at hadronization, the $\bar{c}$ with a normal quark, leading a D and a $\bar{D}$ respectively. If nuclear collisions produce a deconfining medium, then such collisions must also lead to a suppression of J/ψ production [1]. A schematic diagram of the J/ψ production in a N-N collision is shown in Fig.1.9 (Seen in the CM frame, the preformed J/ψ must subsequently travel through a fireball of dense matter formed in the collision as shown in Fig.1.9. The path in dense matter varies depending on the impact parameter, allowing one to evaluate the interaction(absorption) strength. This effect is particularly strong in most central collision of nuclei).

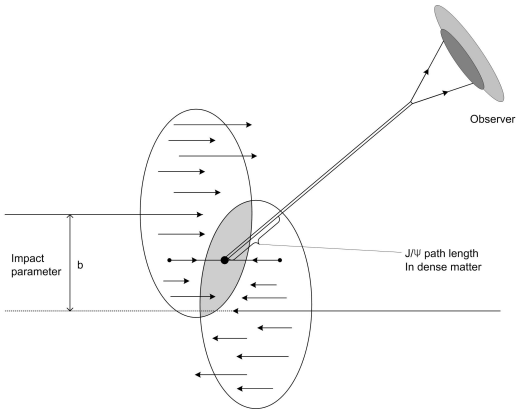

Figure 1.9 The CM picture of initial moments of nuclear collision and an illustration of the path traveled by J/ψ in dense matter.

At the CERN SPS, the NA38 and NA50 experiments have extensively studied J/ψ production in nucleus-nucleus collisions, to establish a detailed production pattern that can be used to prove the existence of the deconfined phase predicted by QCD. By January of 2000 the NA50 collaboration at CERN had completed a systematic study of J/ψ production in Pb-Pb collisions at a beam energy of 158 GeV per nucleon extending the previous study of the NA38 for p+A, S+U reactions. In the collisions with the largest energy densities, an "anomalous" J/ψ suppression was observed that did not follow the conventional picture [3]. In Fig 1.10a the ratio of measured J/ψ to that expected from the conventional picture(see the Fig. 1.10b) is plotted as a function of the energy density achieved in the collision. If the absorption of the J/ψ were only due to the "normal" nuclear absorption, the data would follow the dashed line. But the data clearly deviate from this expectation at the energy density above 2.5 GeV/fm^3. Furthermore, the onset of this deviation is relative abrupt and the structure in the deviation is consistent with a multistage mechanism of this additional suppression. On February 19, 2000, CERN made a press release declaring that a new state of matter had been created in the SPS collisions.

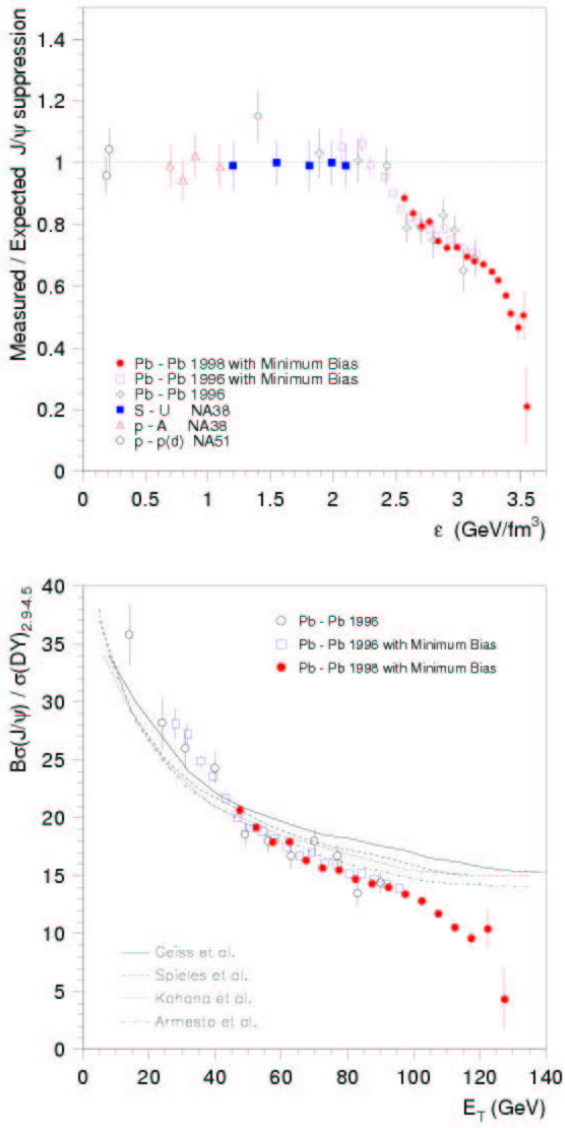

Figure 1.10 a)The J/ψ anomalous suppression as a function of the energy density reached in the collision. Suppression is obtained from the measured cross-section divided by the values expected from nuclear absorption(up). b)Comparison between the NA50 Pb-Pb data and several conventional calculation of J/ψ suppression(down).

1.2 Theoretical models of J/ψ production

The suppression of the J/ψ yield in relativistic heavy-ion collisions is a possible signature for the formation of the QGP because of the J/ψ should dissolve in the QGP, due to the colour screening [1]. The suggestion has stimulated the experimental research to measure the J/ψ production in the heavy-ion collisions and various theoretical models have been proposed to interpret the experimental results.

To verify this prediction, one has to exclude what are generally called "conventional" mechanisms, covering all the possible ways to suppress the J/ψ production without introducing deconfinement. Together with the absorption in nuclear matter and by hadronic comovers mentioned above, other possible sources of the J/ψ suppression can be the nuclear shadowing of the parton distribution function [149], the medium induced energy loss of the incident partons leading to the $c\bar{c}$ production [77] or more in general the in-medium modifications of the $c\bar{c}$ production process [76]. In a realistic model of the J/ψ production in p+A and A+B collisions, all these effects should be included.

1.2.1 J/ψ production in hadron-hadron collisions

Current theoretical and experimental knowledge of hadro-production of charmonia is described in the following.

Production of J/ψ and other charmonia in hadron-hadron collisions is understood in the following framework based upon the QCD factorization theorem [88]. Figure 1.11 shows an example of Feynman diagram for hadro-production of J/ψ. According to the factorization theorem, the cross section to produce a charmonium ψ in a collision of hadron A and B, $\sigma(AB \to \psi X)$ can be factorized into:

- $f_{a/A}(x, Q)$: Probability for a parton a to be found in a hadron A, called a Parton Distribution Function (PDF), where x is a momentum fraction of a to A and Q is a scale for the parton interaction,
- $f_{b/B}(x, Q)$: Probability for a parton b to be found in a hadron B and

- $\sigma(ab \to \psi X)$: Cross section for the partonic subprocess $ab \to \psi X$, where ψ is produced in the hard scattering of the parton a and b,

and written as

$$\sigma(AB \to \psi X) = \sum_{ab} \iint dx_1 dx_2 f_{a/A}(x_1, Q) f_{b/B}(x_2, Q) \sigma(ab \to \psi X).$$

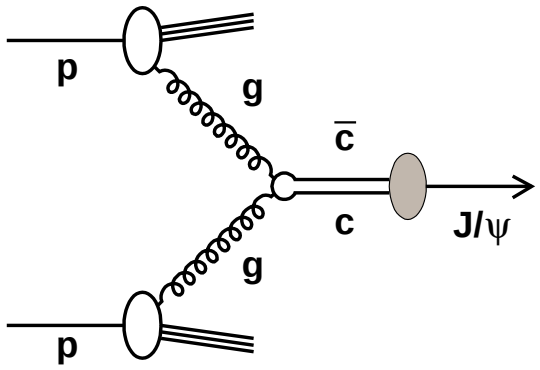

Figure 1.11 An example of J/ψ hadro-production. In this example, a J/ψ meson is produced in the subprocess $g + g \to J/\psi$ in a p+p collision. The oval between the $c\bar{c}$ pair and the J/ψ represents the formation of the J/ψ from the $c\bar{c}$ pair which is a non-perturbative phenomenon.

Following 2→1 subprocesses contribute to low-p_T (transverse momentum) production of ψ ($\lesssim$ 1 GeV/c):

- $g + g \to \psi$ and
- $q + \bar{q} \to \psi$,

where q and g denote a quark and a gluon respectively. Figure 1.11 is an example of the $g+g \to \psi$ subprocess. Medium and high p_T ψ's are produced in the following 2→2 subprocesses:

- $g + g \to \psi + g$,
- $g + q \to \psi + q$ and
- $q + \bar{q} \to \psi + g$.

At RHIC energies ($\sqrt{s}$ = 200 to 500 GeV) $g + g$ and $g + q$ subprocesses contribute to cross sections significantly.

Production of ψ from initial partons is further separated into two steps: production of a $c\bar{c}$ pair in the hard scattering of the initial partons (**step 1**) and hadronization of a charmonium ψ from the $c\bar{c}$ pair (**step 2**). This is possible since energy scales for each step are well separated, that is, $2M_c \sim 3$ GeV (M_c is the charm quark mass) for **step 1** and $\Lambda_{QCD} \sim 0.2$ GeV for **step 2** which is the inverse of a typical hadron size. The cross section for **step 1** can be calculated using perturbative QCD. On the other hand, the probability for **step 2** is not calculable with it, because it is a non-perturbative phenomenon. There are some theoretical models for charmonium production each of which assumes a different assumption and treatment on **step 2**.

The color-evaporation model (CEM) or the semi-local duality approach [89, 90], born in the 1970s, simply ignores the color and other quantum numbers of $c\bar{c}$ pairs and assumes a certain fraction of them, which is needed to be determined from experimental data, forms each charmonium state through multiple soft-gluon emissions as illustrated in Fig. 1.12. The CEM describes experimental data on low-p_T or p_T-integrated results well, where the soft gluon picture is expected to be valid. For example, the CEM describes J/ψ's total cross sections in both hadro-production and photo-production at lower energies [91]. Also the CEM prediction of zero polarization (spin-alignment) of J/ψ's is consistent with the lower-energy experiments where low-p_T contribution is dominant [120], but contradicts to the CDF data at medium and high p_T [124].

A more sophisticated model born in the 1980s, the color-singlet model (CSM) [92, 93], requires a $c\bar{c}$ pair to be the color-singlet state and have the same quantum numbers as the charmonium to be formed. Figure 1.13 shows an example of the lowest order production of a J/ψ with the CSM where the $c\bar{c}$ pair should be in $^{2s+1}L_J = {}^3S_1$ and the color-singlet state as the J/ψ. It should be noted that an additional hard-gluon emission is

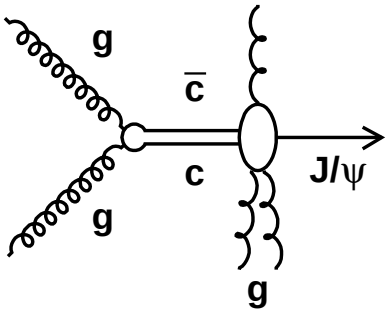

Figure 1.12 A schematic diagram for J/ψ production from gluon fusion with the color-evaporation model. Incoming protons are omitted in the figure. Multiple soft-gluon emissions destroy the information on quantum numbers of the $c\bar{c}$ pair.

necessary to conserve the C-parity. The CSM can unambiguously predict production cross sections for each charmonium without any free parameters and has explained p_T distributions of J/ψ production at ISR energies ($\sqrt{s}$ = 30 to 63 GeV) reasonably well [92]. However the CSM failed to explain p_T differential cross sections of the Tevatron data in p+$\bar{\text{p}}$ collisions at $\sqrt{s}$ = 1.8 TeV by large factors (30 $\sim$ 50) [122]. CSM predictions do not agree either with the total cross sections at lower energies by a factor of about 20 [99].

To explain these discrepancies, the color-octet model (COM) [94] has been developed in the 1990s based upon the non-relativistic QCD framework [95]. The COM allows the formation of a charmonium from a color-octet $c\bar{c}$ pair with one or some soft gluon emissions. Figure 1.14 shows an example of the lowest order production of a J/ψ with the COM from the gluon fusion subprocess. The $c\bar{c}$ pair, which is in $^1S_0$ (or ^3P_J) and the color-octet state, forms a J/ψ with a soft gluon emission. Using appropriate color-octet matrix elements, which are additional free parameters needed to be extracted from experimental data, the COM has successfully reproduced p_T distributions at CDF [96–98] as shown in Fig. 1.15 and total

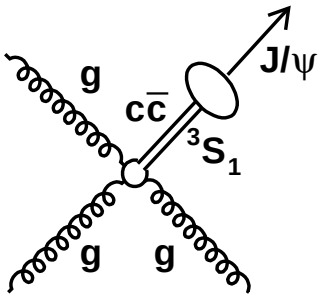

Figure 1.13 An example of the lowest order diagram for direct J/ψ production from gluon fusion with the color-singlet model. Incoming protons are omitted in the figure. The $c\bar{c}$ pair is in the color-singlet state.

cross sections at lower-energy experiments [99–101]. COM predictions for the relative yields for each charmonium state (for example, χ_c to direct J/ψ ratio) are also consistent with the experimental data [100], which will be discussed in Appendix B. However extraction of these matrix elements is still controversial and therefore large ambiguities are left for the prediction with the COM.

Hadro-production data on J/ψ and other charmonia are available in both fixed-target experiments and collider experiments in a wide energy range (6.1 GeV $\leq \sqrt{s} \leq$ 1.8 TeV) [102–125]. Measurements of such as total and p_T-differential cross-sections, polarization, and relative yields of each charmonium have promoted better understanding of production mechanism. However more data on different observables at different energies are required since currently none of the theoretical models can successfully explain all the experimental data at all energies.

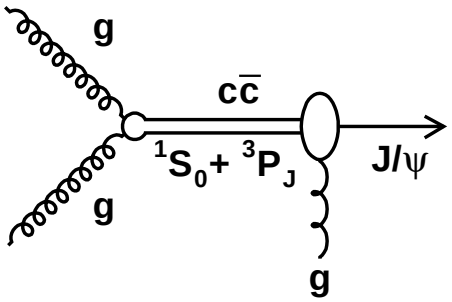

Figure 1.14 An example of the lowest order diagram for direct J/ψ production from gluon fusion with the color-octet model. Incoming protons are omitted in the figure. The $c\bar{c}$ pair is in the color-octet state.

1.2.2 Nuclear Shadowing

Proton-nucleus collisions not only provide important baseline information for the study of QCD at high temperatures, they also address the fundamental issues of the parton structure of nuclei. Since the discovery of the EMC effect in the 1980's, it is clear that the parton-level processes and structure of a nucleon are modified when embedded in nuclear matter [141].

These modifications reflect fundamental issues in the QCD description of the parton distributions, their modifications by the crowded nuclear environment of nucleons, gluons and quarks, and the effect of these constituents of the nucleus on the propagation and reactions of energetic partons that pass through them. Of particular interest is the depletion of low momentum partons (gluons or quarks), called shadowing, which results from the large density of very low momentum partons. For gluons at very low momentum fraction one can associate with them, following the uncertainty principle, a large distance scale. These high-density gluons then will interact strongly with many of their neighbors and by gluon recombination or fusion are thought to promote themselves to larger momentum fraction, thereby depleting small values of x. In recent years a specific model for these processes,

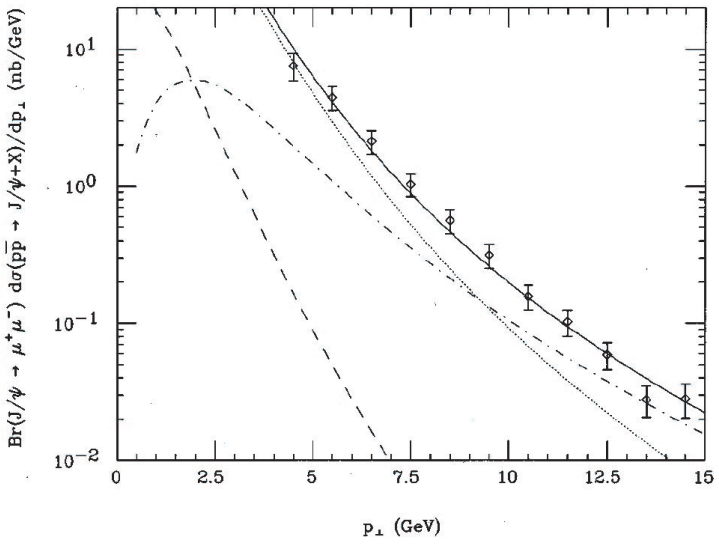

Figure 1.15 Transverse momentum differential cross sections for prompt (excluding b-quark decays) J/ψ production measured by the CDF experiment compared with theoretical predictions. The dashed curve depicts the direct color-singlet contribution. The dot-dashed curve illustrates the contribution of the ${}^3S_1$ octet state of the $c\bar{c}$ pairs and the dotted curve denotes the combined contribution of the ${}^1S_0$ and ${}^3P_J$ octet states. The solid curve equals the sum of the color-singlet and color-octet contributions. All curves are multiplied by the muon branching ratio $B(J/\psi \to \mu^+\mu^-)$.

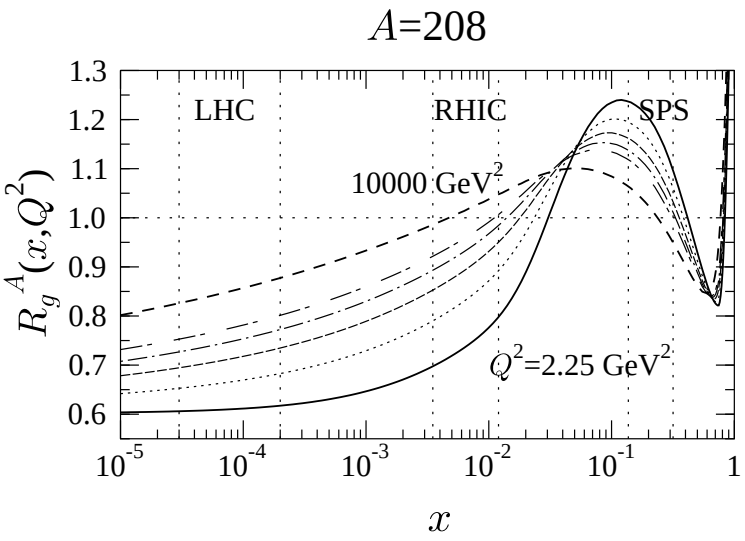

Figure 1.16 Scale evolution of the ratio $R_g^A(x, Q^2)$ for an isoscalar nucleus A=208 according to EKS98 [21, 22]. The ratios are shown as functions of x at fixed values of Q^2 equidistant in $\log Q^2$: 2.25 GeV^2 (solid), 5.39 GeV^2 (dotted), 14.7 GeV^2 (dashed), 39.9 GeV^2 (dotted-dashed), 108 GeV^2 (double-dashed), and 10000 GeV^2 (dashed). The regions between the vertical dashed lines show the dominant values of x_2 probed by muon pair production from $D\overline{D}$ at SPS, RHIC and LHC energies.

called gluon saturation, which affects both the asymptotic behavior of the nucleon gluon distributions as x approaches zero and the modification of this behavior in nuclei, i.e. shadowing, has been discussed extensively by McLerran and collaborators [24–26]. At RHIC energies many of the observables accessible to PHENIX sample regions of very small x where nuclear shadowing is thought to be quite strong. However, theoretical predictions of the amount of shadowing differ by factors as large as three. For example, in the production of J/ψ in the large rapidity region covered by the PHENIX muon arms, as shown in Fig 1.17, models from Eskola et al. [22] predict

only a 30% reduction due to gluon shadowing, while those of Frankfurt and Strikman [23] or Kopeliovich [20] predict up to a factor of three reduction. Results from the measurements of the just-completed d+Au run should help to clarify how much shadowing is present, but increased statistics from higher luminosity runs and more definitive measurements with enhanced detectors capable of making more exclusive measurements in several channels will be necessary to test the theory with sufficient power to constrain the underlying QCD processes.

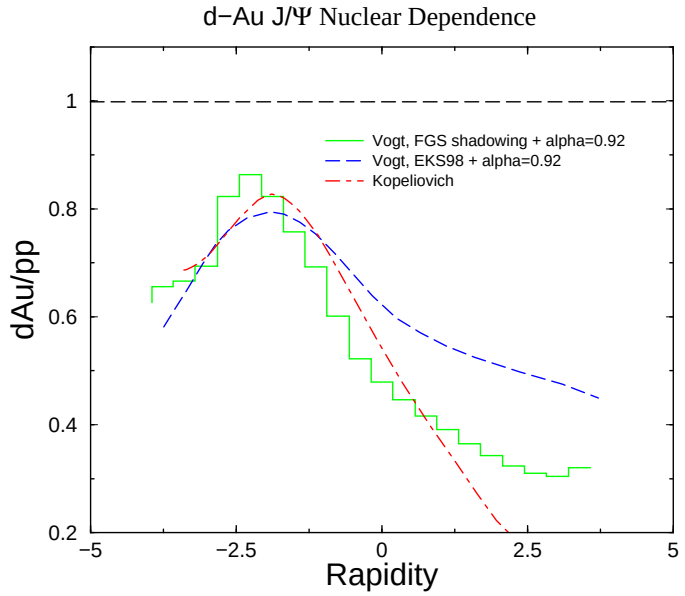

Figure 1.17 Rapidity dependence of shadowing in the nuclear dependency of J/ψ production for three different shadowing models [20, 22, 23]. The first two curves, green dot-dashed and blue dashed, are calculations from Vogt using the shadowing prescriptions from Frankfurt & Strikman [23] and Eskola [22]. Since Vogt did not include nuclear absorption in these calculations we have added a rapidity-independent absorption factor corresponding to α = 0.92. The last model is that of Kopeliovich [20].

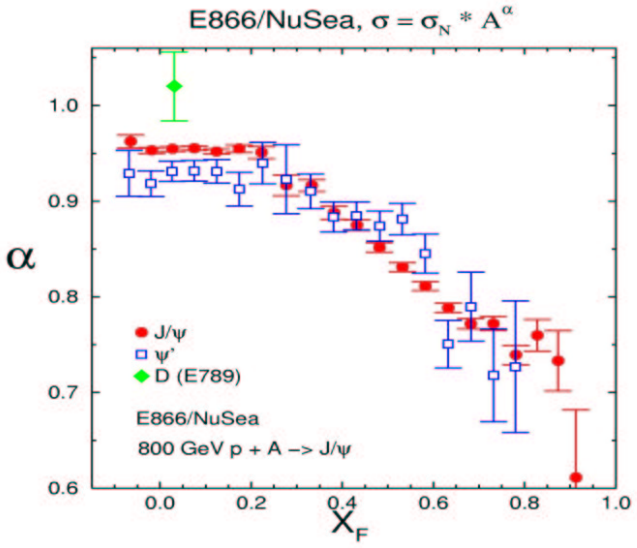

Figure 1.18 α for the J/ψ(red closed circles), $\psi\prime$(open squares) and open charm(green closed circle) versus x_F. α is extracted from $\sigma_A = \sigma_N A^\alpha$. 1.$J/\psi$ and $\psi\prime$ similar at large x_F where they both correspond to a $c\bar{c}$ traversing the nucleus. 2.but $\psi\prime$ absorbed more strongly than J/ψ near mid-rapidity($x_F = 0$) where the resonances are beginning to be hadronized in nucleus. 3.open charm not suppressed($x_F = 0$)

1.2.3 Nuclear absorption

The nuclear dependence of hard processes including J/ψ production is usually parameterized as a power law:

$$\sigma_{pA} = \sigma_{pp} A^\alpha \tag{1.6}$$

The exponent α implicitly contains all nuclear effects, both in the final state(absorption or dissociation) and in the initial state(nuclear modifications of the parton distribution functions). In case there are no initial state effects, the case $\alpha = 1$ is for a particle that once produced does not interact with the surrounding medium. This is true for example for muon pairs produced in the Drell-Yan process but it is not true for the J/ψ. In fact

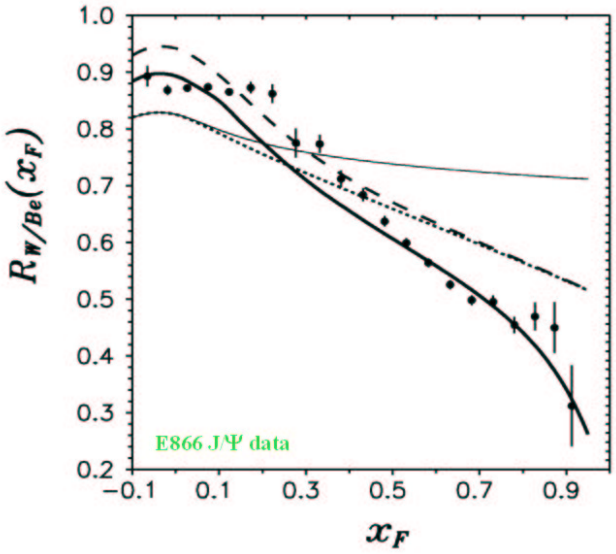

Figure 1.19 Tungsten to beryllium cross section ratio for J/ψ as a function of x_F. The thin solid curve represents contribution of quark shadowing and final state attenuation for χ production. The dotted curve includes also gluon shadowing. The dashed curve includes anti-shadowing and the final solid line includes energy loss

the J/ψ, being an hadron, strongly interacts with the surrounding medium. The expected α is therefore smaller than 1.

Different experiments measured the $\alpha_{J/\psi}$ in proton-nucleus collisions. Unfortunately the α values only marginally agree with each other. Moreover when p+p data are considered together with p+A data, the resulting α values are often inconsistent with a fit to the proton-nucleus data. A careful measurement with small statistic and systematic error would therefore be of the greatest importance. In fact the measured α value can be used to extract an effective cross section of the J/ψ with the nuclear matter.

In more theoretical point of view which was described in the previous section, J/ψ production passed through the three-step process $gg(q\bar{q}) \rightarrow (c\bar{c})_8 \rightarrow (c\bar{c})_1 g \rightarrow J/\psi$. The pre-resonance state $(c\bar{c})_1 g$ takes a time $\tau_8 \approx$

0.3fm to convert to a fully formed J/ψ, by absorbing the collinear gluons. It may happen that this pre-meson state interacts with the nucleons of the target and the projectile and it is absorbed before becoming a physical resonance. The nuclear absorption is taken into account by all the models trying to describe J/ψ suppression in collisions from p+A to A+B. In p+A collisions the pre-resonance absorption is the only relevant process to take into account in order to understand the experimental results, while in A+B collisions other additional mechanisms are required to explain the data.

The cross-section for the nuclear absorption of the $(c\bar{c})_1 g$ state in nuclear matter can be theoretically estimated but also derived from experimental p+A data. In A+B collisions, the probability that the $c\bar{c}$ pair survives the interactions with the nuclear matter is the product of the survival probability for interactions with the target nucleons and, for nucleus-nucleus collisions, with the projectile nucleons.

$$S^{abs}_{J/\psi} \sim exp\{-\int_{z_A}^{\infty} dz \rho_A(z) \sigma^{abs}_{J/\psi-N} \int_{z_B}^{\infty} dz \rho_B(z) \sigma^{abs}_{J/\psi-N}\} \qquad (1.7)$$

where ρ is the nuclear density and $\sigma^{abs}_{J/\psi-N}$ is the absorption cross-section for the J/ψ-nucleon interactions. $z_A(z_B)$ represents the formation point of the pre-resonance within the projectile nucleus A(B). Note that $S^{abs}_{J/\psi}$ =1 for $\sigma^{abs}_{J/\psi-N}$=0. In p+A collision only the first probability is considered.

Since the J/ψ travels through the surrounding nucleons, an appropriate variable to parametrize the measured J/ψ yield is the number of nucleons it can potentially interact with. The number can be calculated as the product ρL, where ρ is the average nuclear density and L is the lenght of nuclear matter the $c\bar{c}$ state traverses while escaping from the interaction region. The L variable is a relativistic invariant quantity. As an approximation the charmonium survival probability can therefore be parametrized as exp(-$\sigma_{abs}\rho$L).

1.2.4 Charmonium absorption by hadronic comovers

In nucleon-nucleon collisions the hadrons produced along with the $c\bar{c}$ pairs are called "comovers". These comoving secondaries, formed after $\tau_0 \sim 1 - 2fm$(greater than the typical formation time of a J/ψ from a colour

octant state, $\tau_8 \sim 0.3fm$) from the collision time, can interact with the final charmonium state and destroy it, via the inelastic reaction

$$J\psi + h \rightarrow D\bar{D} + X \tag{1.8}$$

This produces an additional suppression of the produced J/ψ, which was studied to explain the experimental J/ψ suppression without requiring deconfinement [81]. The probability that the J/ψ survives an interaction with comovers [66] is:

$$S^{com}_{J/\psi} \sim exp\{-\int d\tau < \sigma_{J/\psi-com} \cdot v > \rho_{com}(\tau)\} \tag{1.9}$$

where ρ_{com} is the comover density at time τ, $\sigma_{J/\psi-com}$ is the J/ψ absorption cross-section in the comover medium and v(~ 0.6) is the J/ψ velocity relative to the comovers. Note that, if $\sigma_{J/\psi-com} = 0$, the survival probability $S^{com}_{J/\psi}$ is 1. The product $\sigma_{J/\psi-com} \cdot v$ is averaged over all the possible comovers and their relative energy [81]. $S^{com}_{J/\psi}$ is treated as an adjustable parameter by different models, which include also the nuclear absorption [81]. In these calculations the values found for $S^{com}_{J/\psi}$ range from 0.4mb to 3mb. All these different approaches [71–74] lead to a monotonic increase of the J/ψ suppression with increasing centrality and comover density. They can produce the J/ψ suppression observed in NA50 J/ψ data from p+A to central S-U collisions, where no deconfinement is expected, but fail in the description of central Pb+Pb data [75].

1.2.5 Coalescence

The previous discussion of J/ψ production and suppression has been limited to that of directly produced charmonium. More recent models have predicted that at RHIC energies the increased total charm production will allow the binding of uncorrected $c\bar{c}$ pairs. These models are motivated by the production estimates of 10 $c\bar{c}$ pairs at RHIC energies in a central Au+Au collision. Only a small fraction of these charm pairs would evolve into a J/ψ while most will dissociate. At lower energies if a $c\bar{c}$ pair is created, it is very unlikely that they would find each other again to recombine

as charmonium. However, at full RHIC energies it is possible that uncorrelated charm and anti-charm could combine to form charmonium. There have been four slightly different approaches to explore this component of production

- Gazdzicki and Gorenstein [57] have demonstrated that purely statistical model of charmonium formation at QCD hadronization can account for the centrality dependence of J/ψ yields at full SPS energies. This model does not make any reference to the dynamic origin of the $c\bar{c}$.

- Braun-Munzinger and Stachel [58] use a statistical model assuming a fireball of T = 160 MeV and baryochemical potential of 266 MeV. Like the previous model, all charm is produced in the initial hard scattering and must be free to move within a deconfined QGP. Therefore, the charm component is not in chemical equilibrium with the medium. A charm-quark fugacity modifies the open and hidden charm thermal weights appropriate for the number of primordial $c\bar{c}$. This model thus requires an accurate assessment of total charm production and understanding of the system at the time of hadronization.

- The model Thews et al. [59] differs from previous models in that the dynamic evolution of the QGP fireball. The medium is assumed to be a ideal gas of free gluons and light quarks. In this model, the J/ψ is suppressed by interactions with the free thermal gluons. However, the reverse reaction is also possible. As the fireball evolves the rates of these competing processes are then integrated over the life of the QGP to determine the J/ψ yield.

- Grandchamp and Rapp [60] utilize a two-component model to combine direct production component and the model of Braun-Munzinger and Stachel for the statistical production. This allows the same model to be applied to SPS energies as well as RHIC and the relative importance of these contributions can be evaluated. This model will be further discussed below.

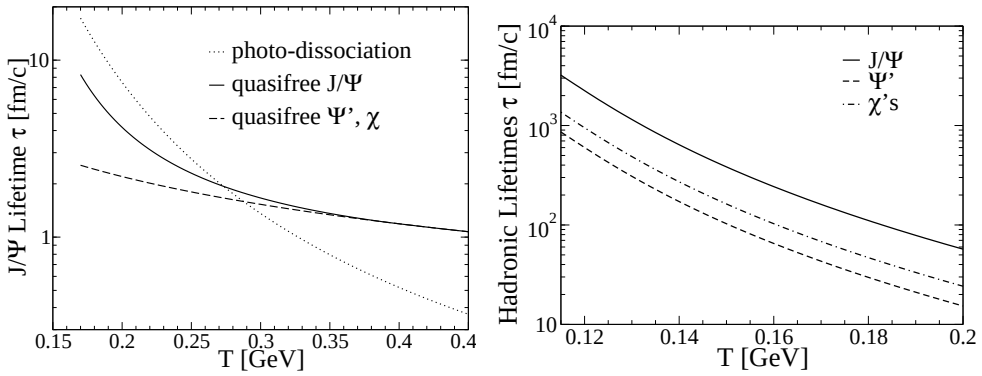

Figure 1.20 The lifetimes of the J/ψ and its relevant feed-down states within QGP(left) and hadronic gas(right) as function of temperature [61].

The model of Granchamp and Rapp has a strength in its applicability to CERN and RHIC energies. There are two sources of J/ψ production considered. First, the direct J/ψ's are produced by the primordial nucleon-nucleon collisions then subjected to dissociation in the QGP followed by the dissociation in the hadronic phase. Second, statistical recombination of independently produced c and $\bar{c}$ at the hadronization of the medium may form the J/ψ. Since they are not formed until hadronization, they are not subjected to dissociation in the QGP but may still be dissociated by comovers. Note that this model does not invoke any additional charm production in the QGP phase.

Within the QGP the primary dissociation mechanism is "quasifree" destruction arising from the in-medium modification to the charmonium binding energy. Within the hadronic phase the primary means of dissociation is due to inelastic collisions with π and ρ mesons since these are the most abundant in the hadron gas. These cross sections are produced using a SU(4) effective theory but in good agreement with the more rigorous quark-exchange model. These dissociation mechanisms can be evaluated over a range of temperatures within both media to determine a lifetime of both the J/ψ and its relevant feed-down states, ψ', X_c as shown in Fig 1.20. The left panel shows the lifetimes within the QGP. At high temperatures all the

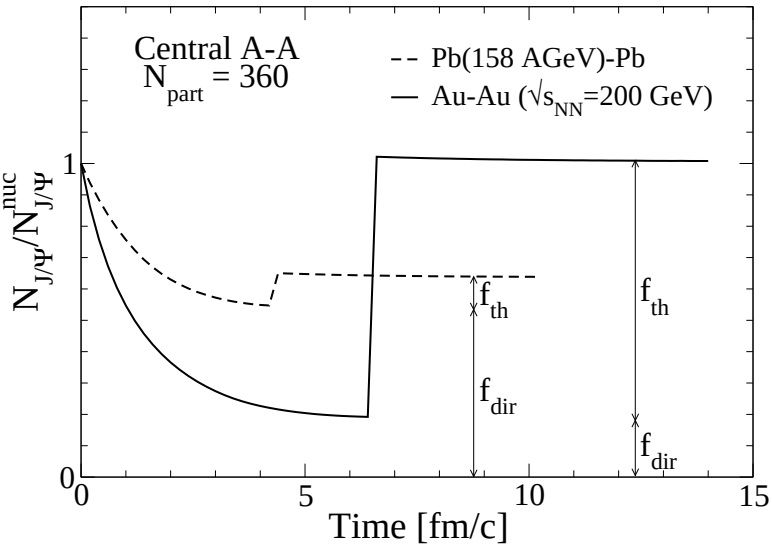

Figure 1.21 The time evolution of the J/ψ population using the two component production model [61].

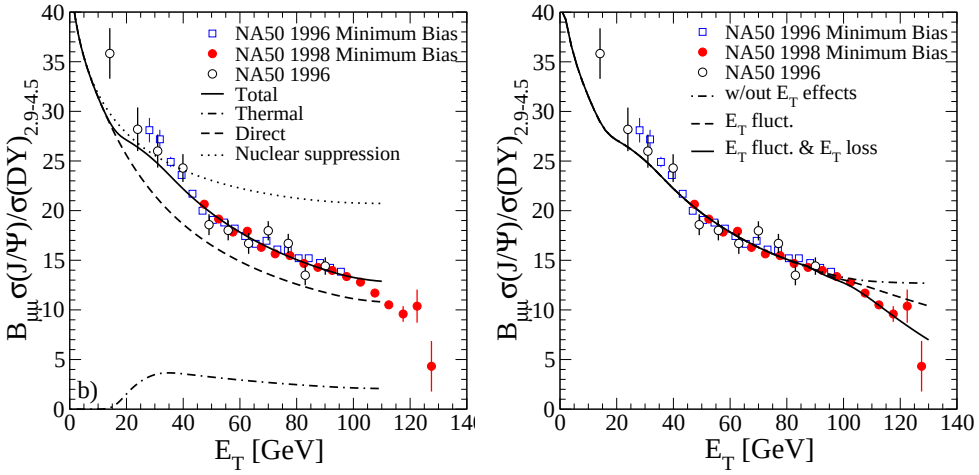

Figure 1.22 The CERN comparison with the two component production model of Grandchamp and Rapp without(left) and with(right) an accounting of the transverse energy fluctuations for the most central event [61]. Results of the two-component model without (dot-dashed line) and with additional inclusion of transverse energy fluctuations (dashed line) and trigger energy loss (full line), for the centrality dependence of the $B_{\mu\mu}\sigma^{J/\Psi}/\sigma^{DY}$ ratio in Pb(158 AGeV)-Pb collisions.

considered states have very similar lifetimes while at lower temperatures the more tightly bound J/ψ has a greater lifetime than the more weakly bound states. Assuming a fixed initial J/ψ and open charm production rate, the J/ψ population can be evaluated as dissociation occurs within the cooling QGP, closed charm is recovered through hadronization, and dissociation occurs again in the expanding hadronic fireball. This time evolution is diagrammatized in Fig 1.21. A comparison of the model with the CERN NA50 data reveals a remarkably good agreement as demonstrated in 1.22. In the left panel the first inflection in the data which is often attributed to the first melting of the J/ψ feed down states is in this model a result of the onset of the contribution of statistical production. At SPS only a small fraction of the observed J/ψ are created statistically.

1.2.6 The Drell-Yan reference

The process used as a reference, in the J/ψ suppression study is the Drell-Yan process which produces opposite sign muon pairs in the same invariant mass range of the J/ψ. The main features of this process is given in this section. The Drell-Yan production of lepton pairs is given by the annihilation of a quark and anti-quark of the same flavour through the emission of a virtual photon in a hadron-hadron interaction at the leading order. Fig 1.23 shows the Drell-Yan process at the leading order.

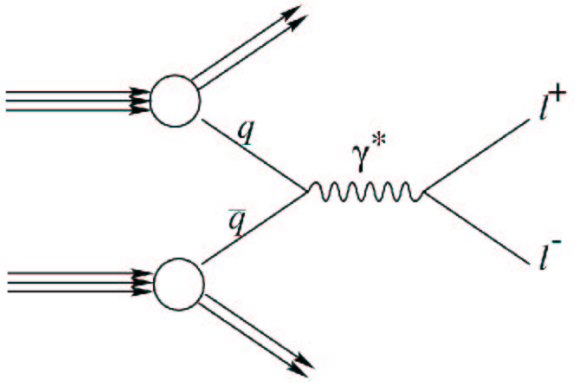

Figure 1.23 Leading order diagram of the Drell-Yan process

The elementary cross-section of the quark-antiquark annihilation in a lepton pair can be expressed as

$$q_i\bar{q}_i \rightarrow \gamma^* \rightarrow l^+l^- \tag{1.10}$$

is calculated as

$$\frac{d\sigma}{d\Omega}|_{cms} = \frac{4}{16}\alpha^2\frac{e_i^2}{M^2}(1 + cos^2\theta) \tag{1.11}$$

and if it is integrated over the solid angle can be written as

$$\sigma_i(q_i\bar{q}_i \rightarrow \gamma^* \rightarrow l^+l^-) = \frac{4}{3}\pi\alpha^2\frac{e_i^2}{M^2} \tag{1.12}$$

where e_i is the electric charge of the quark flavour i(e_u = +2/3,e_d = -1/3,..), M is the mass of the virtual photon(or the invariant mass of the lepton pair produced by its decay) and α is the fine structure constant. If we take into account the probability of finding the quark and the anti-quark of flavour i in the two colliding hadrons, in the framework of the parton model the cross-section can be evaluated as:

$$\frac{d\sigma^2}{dx_1 dx_2} = \frac{1}{3}\frac{4\pi\alpha^2}{3M^2}\Sigma_i e_i^2[f_i^A(x_i)\bar{f_i^B}(x_2) + \bar{f_i^A}(x_1)f_i^B(x_2)] \quad (1.13)$$

where $f_i^A(x_j)$ and $f_i^B(x_j)$ is the parton distribution functions of the projectile A and of the target B, i.e. the probabilities of finding a quark with flavour in A or in B, carrying a longitudinal momentum fraction x_j of the total hadron momentum. The factor 1/3 forces to consider only parton-antiparton annihilation between partons of the same flavour. The f_i is parton distribution functions(PDFs).

Perturbative QCD adds to these elementary parton cross-section the contributions from other sub-process. The correction to the Equation 1.13 with the leading order approximations can be written as:

$$\frac{d\sigma^2}{dx_1 dx_2} = \frac{1}{3}\frac{4\pi\alpha^2}{3M^2}\Sigma_i e_i^2[f_i^A(x_i,Q^2)\bar{f_i^B}(x_2,Q^2)+\bar{f_i^A}(x_1,Q^2)f_i^B(x_2,Q^2)] \quad (1.14)$$

where Q^2 is named "scale" and $Q^2 = -q^2 = M^2$ is the transferred four-momentum. These redefined PDFs are extracted from deep inelastic scattering data. The leading order approximation cross-section underestimates the experimentally measured Drell-Yan cross-section by a factor of 2. This factor is usually known as "Drell-Yan K-factor"(K^{DY}). It is found to be independent from the invariant mass of the Drell-Yan pair above 1.5GeV and with no energy dependence at the currently accessed energies. The K^{DY} can depend, to certain extent, on the particular set of PDFs used in the calculation.

The production of charmonium states in proton interactions with nuclei has been studied extensively at Fermilab as well as at CERN. Since these experiments observe the $\mu^+\mu^-$ decay mode of the J/ψ and ψ', they also

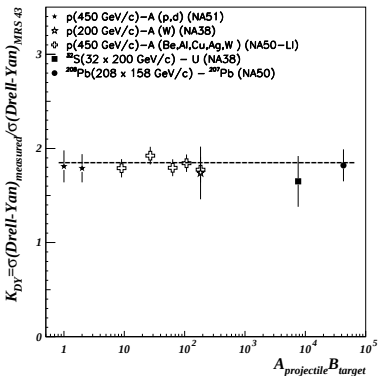

Figure 1.24 Drell-Yan K-factor as a function of $A_{projectile} \times B_{target}$

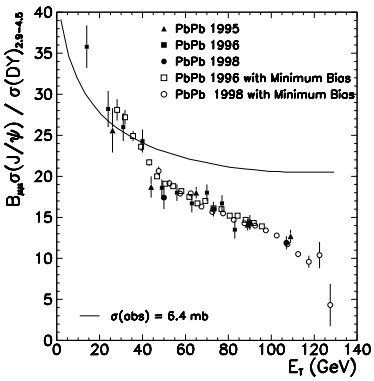

Figure 1.25 $J/\psi/DY$ as a function of E_T; the absorption curve is a fit to the NA38 p-A and S-U data

provide information on the nuclear target dependence of the $\mu^+\mu^-$ continuum spectrum produced by light quark-antiquark annihilation (Drell-Yan process, DY). Whereas the Drell-Yan cross section is observed to grow almost exactly in proportion to the nuclear mass number A, the J/ψ and ψ' production cross sections grow less rapidly. The target dependence is often parametrized as a power law, $\sigma = \sigma_0 A^\alpha$. A value $\alpha < 1$ indicates "suppression" of charmonium production, compared with the naive expectation $\sigma/A = \text{const.}$ obtained when one neglects final state interactions. The argument is that the strictly linear A-dependence of the DY cross section rules out initial state interactions as the origin of the reduced production of charmonium states.[1]

The A-dependence of the nuclear J/ψ and ψ' cross sections is remarkably similar. Both can be fit by the same exponent $\alpha \approx 0.92$, as shown in Fig. 1.26. Since the mean radius of the ψ' is much larger than that of

[1] This argument is not strictly correct, because heavy quarks are predominantly formed by gluon fusion or gluon scattering. Gluons might be more susceptible to initial state interactions than quarks and antiquarks. There is, indeed, evidence for enhanced initial state scattering of gluons from the p_T-spectra of heavy quark states produced in $p + \bar{p}$ reactions, giving rise to a broader "intrinsic" transverse momentum spread of gluons [28].

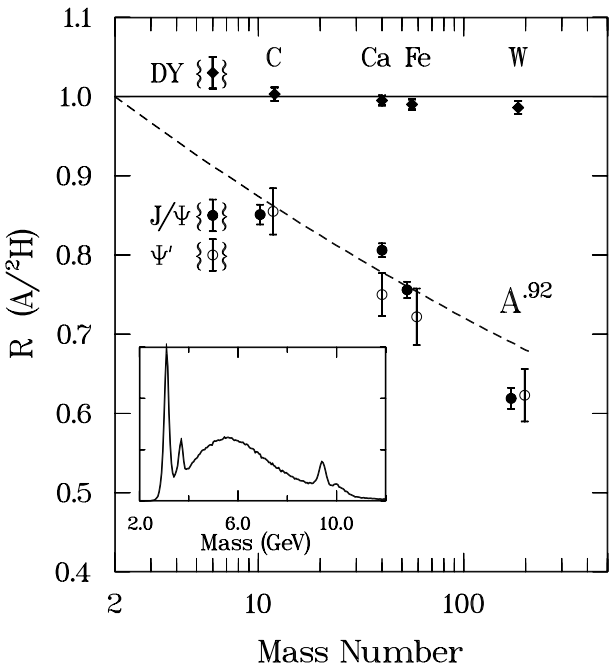

Figure 1.26 Ratio of nuclear cross section compared to deuterium for Drell-Yan pairs (DY), J/ψ and ψ' production. Note that the nuclear suppression for J/ψ and ψ' is the same. Data from experiment E772 at Fermilab [29].

the J/ψ, the equally strong suppression indicates that the final state interactions occur with a state that is not an eigenstate of the $(c\bar{c})$ system but rather with a common precursor of the J/ψ and ψ'. This does not come as a surprise, because the center of mass of the produced $(c\bar{c})$ pair moves rapidly with respect to the target nucleus. As viewed from the rest frame of the $(c\bar{c})$ pair, the nucleus is highly Lorentz contracted and thus the $(c\bar{c})$ pair leaves the target nucleus before the components corresponding to different quantum mechanical eigenstates of the charmonium system have had time to decohere.

The NA38/NA51/NA50 experiments have verified that, as expected theoretically, the Drell-Yan cross-section σ(DY) is proportional to the number of elementary nucleon-nucleon collisions, from proton-proton up to lead-lead interactions included (see Fig. 1.24). The ratio of the cross-sections for J/ψ and Drell-Yan production is therefore proportional to the J/ψ production cross-section per nucleon-nucleon collision. Moreover, the ratio $B_{\mu\mu}\sigma(J/\psi)/\sigma(DY)$ is directly measured and it is insensitive to reconstruction or trigger inefficiencies (identical muon pair topology for J/ψ and Drell-Yan events) or to absolute normalization uncertainties which obviously cancel out. Fig. 1.25 shows the ratio $B_{\mu\mu}\sigma(J/\psi)/\sigma(DY)$ as a function of E_T, for the previously collected Pb-Pb data samples – 1995, 1996 and 1998. The continuous line is the J/ψ normal absorption in nuclear matter and fits the NA51 p-p and p-d and NA38 p-A and S-U results. A clear departure of the $B_{\mu\mu}\sigma(J/\psi)/\sigma(DY)$ ratios from this normal absorption curve is observed at mid-centrality, suggesting the onset of an anomalous J/ψ suppression mechanism. Furthermore, no saturation of the ratio at high E_T is observed, as opposed to the absorption curve trend.

1.3 The Color Glass Condensate

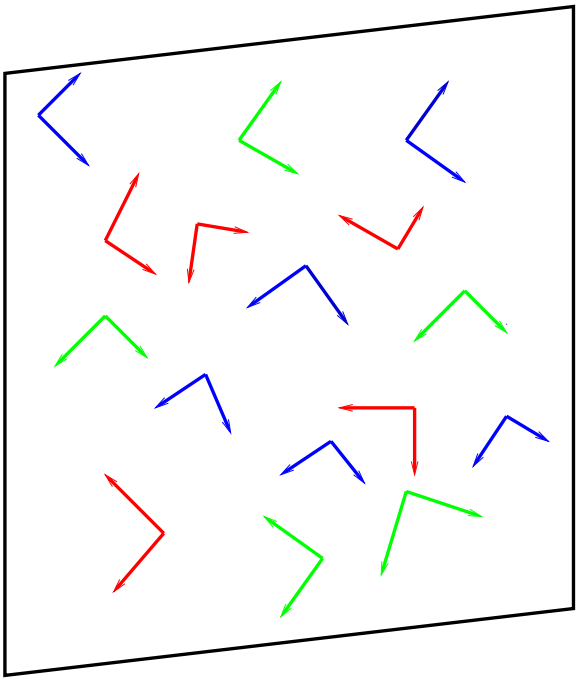

Figure 1.27 The Color Glass Condensate.

To understand this new form of matter, it is convenient to imagine a hadron in a reference frame where it has very large longitudinal momentum. We will be interested in the constituents of the hadron wavefunction which have small longitudinal momentum in this frame of reference. These low momentum constituents are produced by the high momentum ones. Because the high momentum constituents appear to have time scales which are Lorentz time dilated compared to their natural scales, and since they induce the low momentum fields associated with the low momentum particles, the low momentum fields evolve very slowly compared to their natural time scale. Hence the term, Color Glass, since the fields are composed of color gluons, and glass because the time scale for evolution of these low mo-

mentum fields is much longer than their natural time scale. These fields live on a two dimensional sheet because of the Lorentz contraction of the high energy hadron. We shall argue in the following paragraphs that the phase space-density of these fields becomes large and forms a condensate. [31]

The fields on the two dimensional sheet turn out to be similar to the Lienard-Wiechart potentials of electrodynamics. They correspond to plane waves as in the Weizsacker-Williams approximation of electrodynamics, except that they have color. They have their color electric field perpendicular to their color magnetic field and both perpendicular to their direction of motion, $\vec{E}^a \perp \vec{B}^a \perp \vec{z}$. They have a random color. This is shown in Fig. 1.27

The gluon structure function $xG(x,Q^2)$ is experimentally measured to increase at small x. In the reference frame where the hadron is very fast, x is the ratio of a constituent energy to the projectile energy. The gluon distribution is shown in Fig. 1.28a. Note the rapid increase in $xG(x,Q^2)$ as a function of x for small x. This is the origin of the "small x problem". This means that the piece of the hadron wavefunction relevant for small x processes has an increasing density of gluons. In Fig. 1.28, we look at a hadron headed along the beam direction. As x decreases, the density of gluons increases.

The phase space density of gluons is

$$\rho = \frac{1}{\pi R^2}\frac{dN}{dyd^2p_T} \tag{1.15}$$

where R is the hadron size, p_T is the transverse momentum of a constituent, and $y \sim ln(1/x)$. The high density of gluons is generated dynamically and is caused by an instability, which is proportional to the density. The instability is stabilized when the density of partons becomes large enough so that interactions of order $\alpha_{QCD}\eta^2$ become of the order of the linear instability. Here $\eta = \int d^2p_T\rho$. This requires that

$$\eta \sim Q^2_{sat}/\alpha_{QCD} \tag{1.16}$$

The factor of Q^2 arises because we consider densities per unit area, and Q^2_{sat} carries this dimension. This Q_{sat} is called the saturation momentum. The factor of α_{QCD} is the strong coupling strength of QCD. When $Q_{sat} >>$

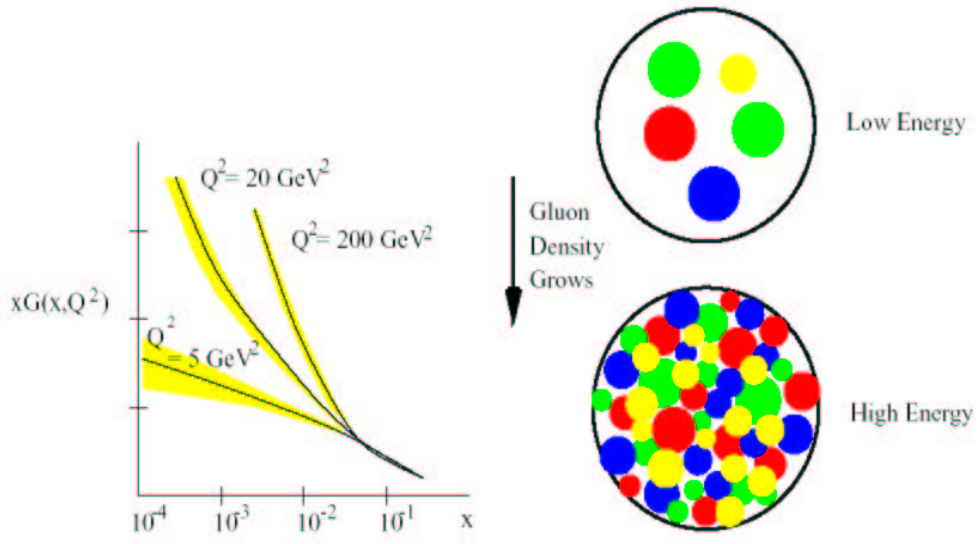

Figure 1.28 The gluon structure function as a function of x for various Q^2. The increase in density of gluons as x decreases.

Λ_{QCD}, we expect that $\alpha_{QCD} << 1$, so that the system becomes a high density Bose Condensate.

The name Color Glass Condensate arises therefore because

- **Color**

  The gluons are colored.

- **Glass** The natural time scale for the evolution of the gluon field is Lorentz time dilated. This is like a glass which is a liquid on long times scales but a solid on short ones.

- **Condensate**

  The phase space density is as large as it can be.

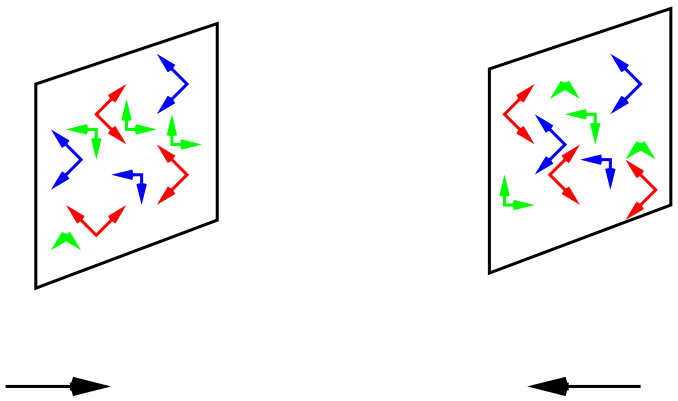

Figure 1.29 High energy nucleus-nucleus collisions.

Space Time Evolution of Heavy Ion Collisions

A collision of two sheets of Colored Glass is shown in Fig. 1.29. This is the picture of nucleus-nucleus collision which arises from the Color Glass Condensate [56]. The time evolution of the matter produced in these collisions is divided into several stages:

- **Initial Conditions**

  For $t < 0$, the two sheets approach one another. The Color Glass is frozen in each nucleus.

- **Melting the Color Glass**

  During the time $0 < t < t_{form}$, the Color Glass melts into quarks and gluons. It is estimated that $t_{form} \sim 1/Q_{sat} \sim .1 - .3\ fm/c$ at RHIC energy. The energy density of the matter at formation is somewhere around $\epsilon_{form} \sim Q_{sat}^4/\alpha_s \sim 20 - 100\ GeV/fm^3$.

- **Thermalization**

  During the time $t_{form} < t < t_{therm}$, the matter expands and thermalizes. Typical thermalization time is estimated to be $t_{therm} \sim .5 - 1\ fm/c$.

- **Hydrodynamic Expansion**

  The system expands as a thermal system until a time of decoupling which is typically about $t_{decoupling} \sim 10\ Fm/c$ at RHIC energy. Here the matter presumably starts as a Quark Gluon Plasma, evolves through a mixed phase of hadrons and Quark Gluon Plasma and eventually becomes a gas of pions. In this stage, most of the physics interesting for studies of the phase transition or cross over between Quark Gluon Plasma and ordinary hadronic matter takes place.

As the Color Glass melts, it produces particles as is shown in Fig. 1.30. The fastest particles have their natural time scale time dilated the most, so

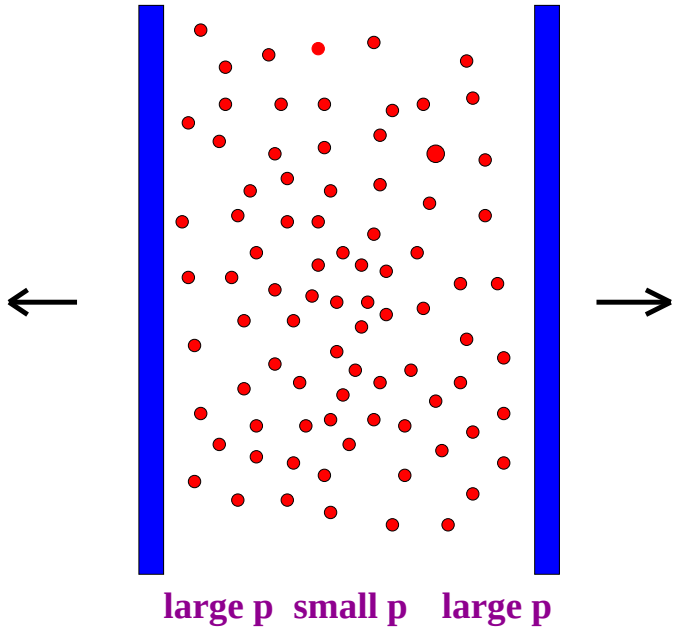

Figure 1.30 Particle production in nucleus-nucleus collision in the center of mass frame.

in the center of mass frame, the fastest particles are produced last. These particles have traveled the longest distance from the collision point, since their formation time is dilated the most. Therefore the matter is formed

with a correlation between momentum and position. This is like Hubble flow in cosmology where if you look at stars, the stars which are farthest away move away the fastest. For heavy ions as in cosmology, this description is frame independent. Unlike in cosmology, the Hubble expansion for heavy ion collisions is 1 dimensional. [8]

The density of particles falls as $N/V \sim 1/t$. If the particles expand without interaction, then the energy per particle is constant. If the particles thermalize, then $E/N \sim T$, and since $N/V \sim T^3$ for a massless gas, the temperature falls as $T \sim t^{-1/3}$. For a gas which is not quite massless, the temperature falls somewhere in the range $T_o > T > T_o(t_o/t)^{1/3}$, that is the temperature is bracketed by the value corresponding to no interaction and to that of a massless relativistic gas. This 1 dimensional expansion continues until the system begins to feel the effects of finite size in the transverse direction, and then rapidly cools through three dimensional expansion. Very close to when three dimensional expansion begins, the system decouples and particle free stream without further interaction to detectors.

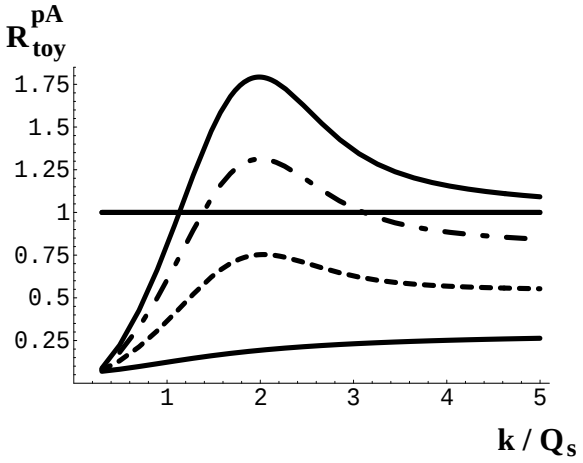

Figure 1.31 toy model CGC

The recent results on suppression of hadron spectra in deuteron gold (dA) collisions in the forward rapidity region(see Fig 1.32 [30]) of the Relativistic Heavy Ion Collider (RHIC) at the Brookhaven National Lab (BNL)

has generated a lot of interest in the applications of semi-classical QCD and the Color Glass Condensate [31] to RHIC. Even though the Color Glass Condensate is the prediction of QCD for the wave function of a hadron or nucleus at high energies [32–34], it is not a priori clear at what energy this happens. There is some experimental evidence [35] that RHIC may be at just high enough energy to see glimpses of the Color Glass Condensate.

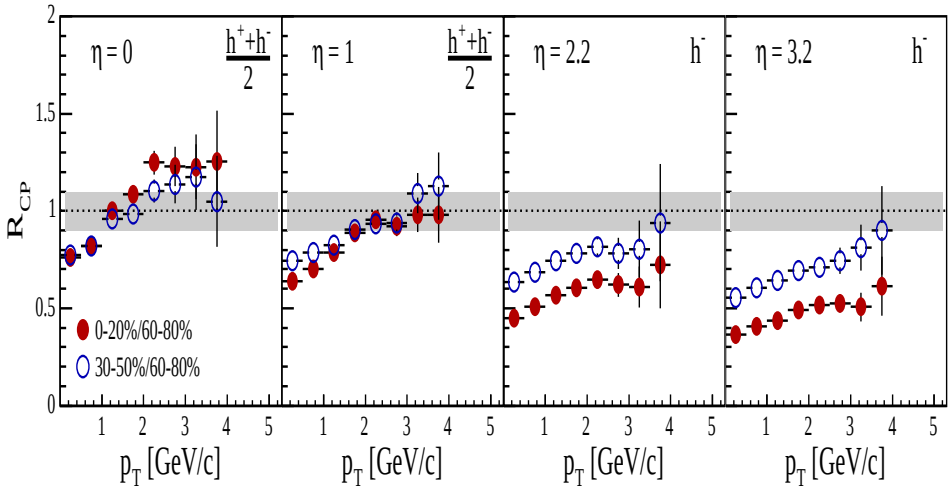

Figure 1.32 BRAHMS experimental results on charged hadron production in deuteron-gold reactions for different pseudo-rapidities as a function of transverse momentum. The ratio of yields in central to peripheral reactions scaled by the nuclear thickness ratio is shown.

The applications of the Color Glass Condensate formalism to the heavy ion collisions at RHIC have been most successful at low p_t [35] which probe the kinematic region where $x_{bj} \sim 0.01$ at mid rapidity. However, the mid rapidity region in heavy ion collisions is not the best place to look for the Color Glass Condensate because of the dominance of the final state effects, such as the energy loss of energetic partons [36] from the possibly formed Quark Gluon Plasma.

$$x \approx \frac{M}{\sqrt{s}} \times e^{-y} \tag{1.17}$$

The forward rapidity region in dA collisions (the deuteron fragmentation region) is the best place in a hadronic/nuclear collision to probe the Color Glass Condensate [37]. First, there is presumably no Quark Gluon Plasma formed in a deuteron gold collision so that the dominant final state effects such the jet energy loss from the plasma are absent. Second, the forward rapidity region probes the small x_{bj} part of the nuclear wave function and the large x_{bj} part of the deuteron wave function. This is the ideal situation for the Color Glass Condensate probes since the high gluon density effects in the nucleus which give rise to the Color Glass Condensate are the strongest in this kinematics.

RHIC is a unique experiment in the sense that it has almost a continuous rapidity coverage, $0 < y < 4$, among its various detectors where it can detect various particles. The STAR detector can measure hadrons and photons in mid rapidity as well as at $y = 4$. The PHENIX collaboration can measure hadrons at mid rapidity as well as dimuons in the rapidity region between $1.2 - 2.2$ while BRAHMS has measured hadrons at mid rapidity as well as rapidities of $1, 2.2$ and 3.2. Therefore, one has the chance to map out the rapidity (x_{bj}) dependence of particle production and confront it with the predictions of the Color Glass Condensate formalism. Already, the qualitative agreement between the predictions of the Color Glass Condensate formalism [38–40] and the data from BRAHMS, both the suppression of R_{dA} and its centrality dependence, are quite remarkable specially since all the available models in the market missed this suppression despite their many free parameters [41].

While there is some evidence in favor of Color Glass Condensate from HERA on electron-proton Deep Inelastic Scattering [50, 53], the BRAHMS collaboration at RHIC may have the best signature of the Color Glass Condensate in a nuclear environment so far in their measurement of the negatively charged hadrons in the forward rapidity region. To verify that this indeed the case, it is important to investigate the predictions of the Color Glass Condensate formalism for other processes.

1.4 Organization of Thesis

The PHENIX experiment was able to measure J/ψs through their dilepton decay in four spectrometers: two central arms covering the mid-rapidity region of $|\eta| < 0.35$ and twice $\pi/2$ in azimuth and two forward muon arms covering the full azimuth and $1.2 < |\eta| < 2.4$ in pseudorapidity. Electrons are identified in the central arms by their Čerenkov rings and by matching the momentum of charged particles reconstructed in drift chambers with the energy deposited in an electromagnetic calorimeter. Muons are selected by an absorber and identified by the depth they reach in a succession of proportional counters staggered with steel walls. The vertex and the event centrality are measured by beam-beam counters lying at $3 < |\eta| < 3.9$.

RHIC has started a physics run from year 2000. In the 2002-2003 run period (Run-3), both d+Au collision and p+p collision data have been accumulated, where J/ψ particles have been successfully detected via both the e^+e^- and $\mu^+\mu^-$ decay channels.

For the p+p collisions, total and differential cross sections for inclusive J/ψ production and for the d+Au collisions, the nuclear modification factor as a function of transverse momentum, rapidity and centrality at $\sqrt{s} =$ 200 GeV will be discussed here. In section 2 and 3, details of the experimental setup and analysis procedure are described respectively, focusing on the $\mu^+\mu^-$ channel measurement. In section 4, results are discussed together with theoretical predictions as well as results of other experiments, followed by the conclusion and the outlook.

Chapter 2

Experimental setup and data acquisition

2.1 The RHIC accelerator complex

The Relativistic Heavy-Ion Collider (RHIC), located in Brookhaven National Laboratory, Upton, New York, is capable of accelerating a wide variety of nuclei and ions from protons to Au (gold) nuclei up to 250-GeV energy for protons (or 100-GeV per nucleon for Au) using two independent rings and colliding them at six interaction points. The design luminosities are 2×10^{26} cm^{-2} sec^{-1} for Au beams and 2×10^{31} cm^{-2} sec^{-1} for proton beams (2×10^{31} cm^{-2} sec^{-1} in an enhanced mode) at the top energy.

Figure 2.1 shows an aerial view of the RHIC accelerator complex. The route for the proton acceleration to RHIC is shown in Fig. 2.2. Starting from the polarized ion source, (polarized) protons are accelerated through Linac, Booster and AGS then injected into both rings of RHIC, whose circumference is 3.834 km. The Blue ring runs clockwise and the Yellow ring runs counter-clockwise. There are currently 120 bunch buckets in each ring whose interval is 106 nsec (or 9.4 MHz frequency). In Run-2, only about a half of them (54 bunch buckets) have been filled. Typical bunch length was 2 nsec (60 cm) in rms during the p+p run.

Experiments are located at the interaction points in RHIC where two bunches in each ring collide at an angle of 0°. There are six interaction

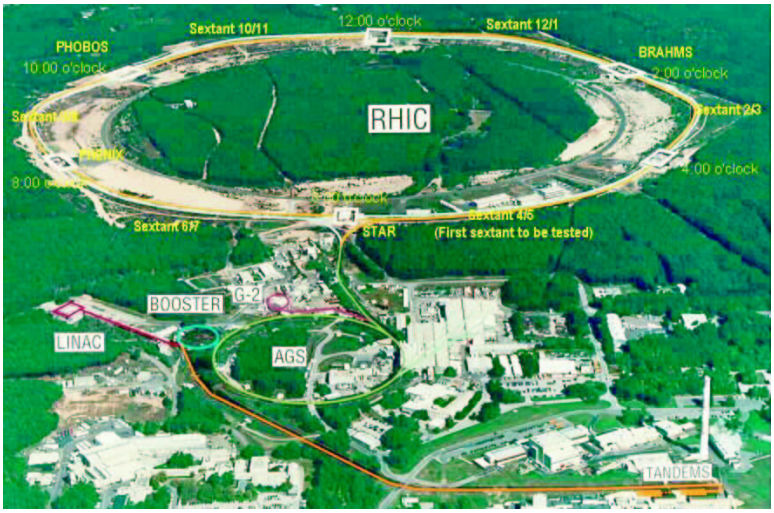

Figure 2.1 The RHIC accelerator complex

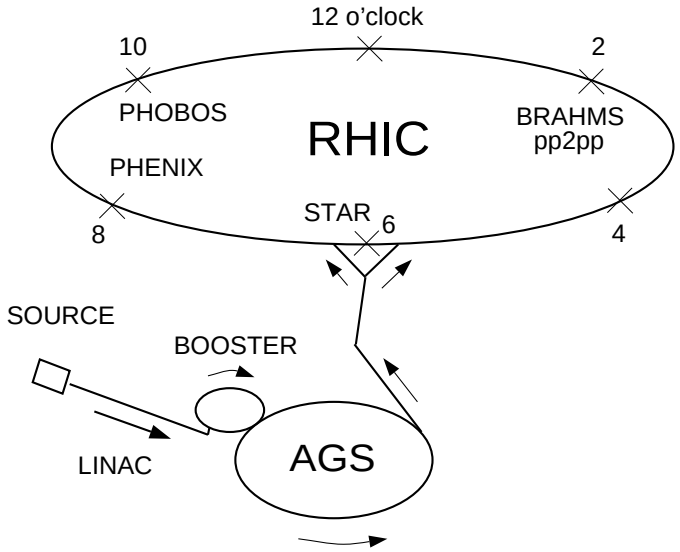

Figure 2.2 The proton acceleration to RHIC

points called 12, 2, 4, 6, 8, and 10 o'clock respectively starting from the north and going clockwise. Table 2.1 shows the experiments at each interaction point. Each experiment demonstrates its unique feature. STAR and PHENIX are the largest experiments at RHIC each with more than 400 collaborators. STAR (Solenoid Tracker At RHIC) tracks and identifies charged particles with a time projection chamber covering a large solid angle. PHENIX (Pioneering High Energy Nuclear and Ion eXperiment) was designed to measure hadrons, leptons and photons in both high multiplicity and high rate environments. BRAHMS measures hadrons over wide ranges of rapidity and momentum using two magnetic spectrometers. PHOBOS consists of a large number of silicon detectors surrounding the interaction region to measure charged particle multiplicities even in the most central Au+Au collisions. The acceptance coverage of each experiment is shown in Fig. 2.3. The pp2pp experiment is aiming at measuring p+p total and elastic cross sections.

Interaction Point (o'clock)	Experiment
12	-
2	pp2pp, BRAHMS
4	-
6	STAR
8	PHENIX
10	PHOBOS

Table 2.1 Experiments at RHIC

2.2 Coordinates and formulae

In this subsection, coordinate system and formulae used to describe the experimental setup and results are introduced.

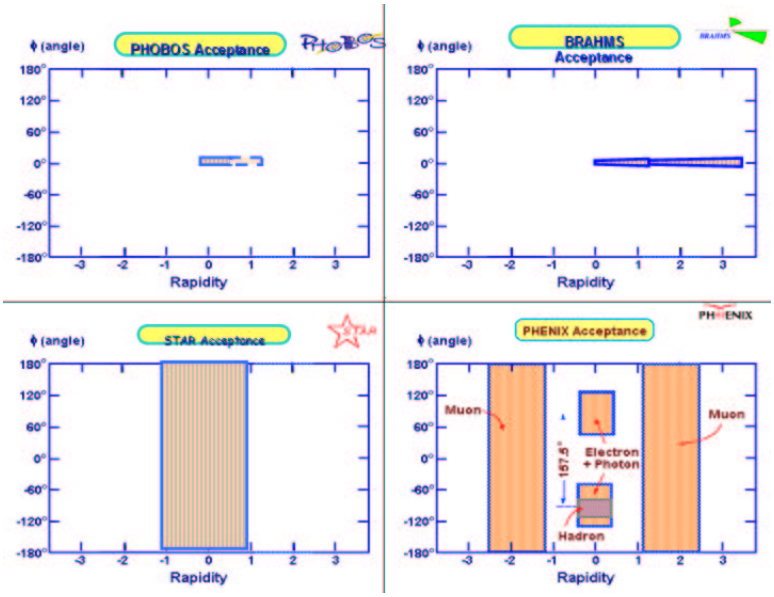

Figure 2.3 The rapidity coverage of Experiments in RHIC

Year	Ions	$\sqrt{s_{NN}}$	Luminosity	Detectors	J/Ψ
2000	Au+Au	130GeV	1 μb^{-1}	Central (electrons)	0
2001	Au+Au	200GeV	24 μb^{-1}	Central	13 + 0
2002	p+p	200GeV	0.15 pb^{-1}	+ 1 muon arm	46 + 66
2003	d+Au	200GeV	2.74 nb^{-1}	Central	300+800+600
2003	p+p	200GeV	0.35 pb^{-1}	+ 2 muon arms	100+300+120
2004	Au+Au	200GeV	240 mb^{-1}	Central +2muon arms	400+2x1600

Table 2.2 The history of RHIC. The table shows the PHENIX detector portions which are used for J/ψ analysis and also shows the number of reconstructed J/ψs in each period of runs.

2.2.1 Coordinate system at PHENIX

The z axis stands for the beam line which runs straight in the experimental area, where positive z points to the north. The polar angle θ and azimuthal angle ϕ are defined with respect to the z axis. The north (south) direction is usually defined as $\theta = 0$ (180) degrees and the west (east) direction is defined as $\phi = 0$ (180) degrees.

2.2.2 Formulae

Rapidity

Rapidity y of a particle is defined as

$$y \equiv \frac{1}{2} \ln \frac{E + p_z}{E - p_z}$$

where E is the energy and p_z is the z-component of momentum of the particle.

Pseudo rapidity

Pseudo rapidity η of a particle is defined as

$$\eta \equiv \frac{1}{2} \ln \frac{p_{tot} + p_z}{p_{tot} - p_z} = -\ln \tan \frac{\theta}{2}$$

where p_{tot} is the scalar value of momentum and θ is the polar angle of the particle direction. In the massless limit, y reaches η.

In the definition above, $y(\eta)$ of a particle going to the south is negative. However, absolute (positive) values of $y(\eta)$ will be often used for those particles in this paper, since results with the spectrometer on the south side of PHENIX will be mainly described and physics should be symmetric with respect to $y(\eta) = 0$.

Kinematics

Common to all models is a required description of the partonic content of both hadronic projectiles and hadronic targets. At high energies, the va-

lence quarks carry a small fraction of the total momentum;they primarily act as sources for gluons and other partonic degrees of freedom. The Parton Distribution Function(PDF) quantifies the probability of finding a parton carrying a fraction(x) of the total hadron momentum. The Feynmann x ($x_F = p_z/p_{zmax}$) of a particle is an experimental observable given by the ratio of the longitudinal momentum to the maximum possible longitudinal momentum. By measuring the X_F of the produced particles directly resulting from the initial hadron-hadron collisions, one can determine the parton distribution functions using the following relationship where x_1 and x_2 are the partonic fractional momentum of the target and projectile. The kinematic distribution for PHENIX central and muon arm is shown in the Fig. 2.4.

2.3 The PHENIX experiment overview

PHENIX is one of the largest experiments at RHIC, located at the 8-o'clock interaction region. Figure 2.5 shows a schematic view of the PHENIX experiment. PHENIX was designed to measure leptons, photons and hadrons in both high-multiplicity heavy-ion collisions and high event-rate p+p collisions.

There are two independent spectrometers in PHENIX which cover different pseudo-rapidity regions. Two Central Arms, East and West Arms, cover the pseudo-rapidity range of $|\eta| < 0.35$ with a quarter azimuth for each Arm and measure electrons, photons and hadrons. Two Muon Arms, North and South Arms, cover $1.2 < \eta < 2.4$ and $-2.2 < \eta < -1.2$ respectively with a full azimuth and measures muons.

There are three magnets in PHENIX. The Central Magnet provides an axial magnetic field for the Central Arms while two Muon Magnets produce a radial field for each Muon Arm. Figure 2.6 shows magnetic field lines inside the magnets. A part of the Central Magnet steel and a copper spacer mounted on each side of it (called a copper nosecone) work as a hadron absorber of about five interaction-length for the Muon Arms. The positions of the nosecones, $z = \pm$ 40 cm, determine a useful vertex region for physics events ($|z| <$ 30 to 40 cm depending on analysis).

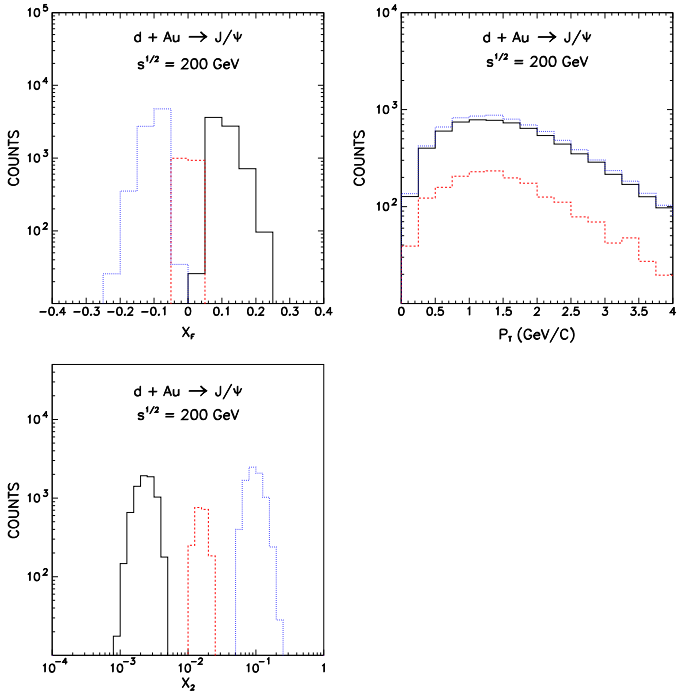

Figure 2.4 Expected event distributions for the J/ψ in a d+Au run at $\sqrt{s}$=200GeV. The Solid, dashed abd dotted histograms correspond to the North muon arm, central arm and South muon arm respectively

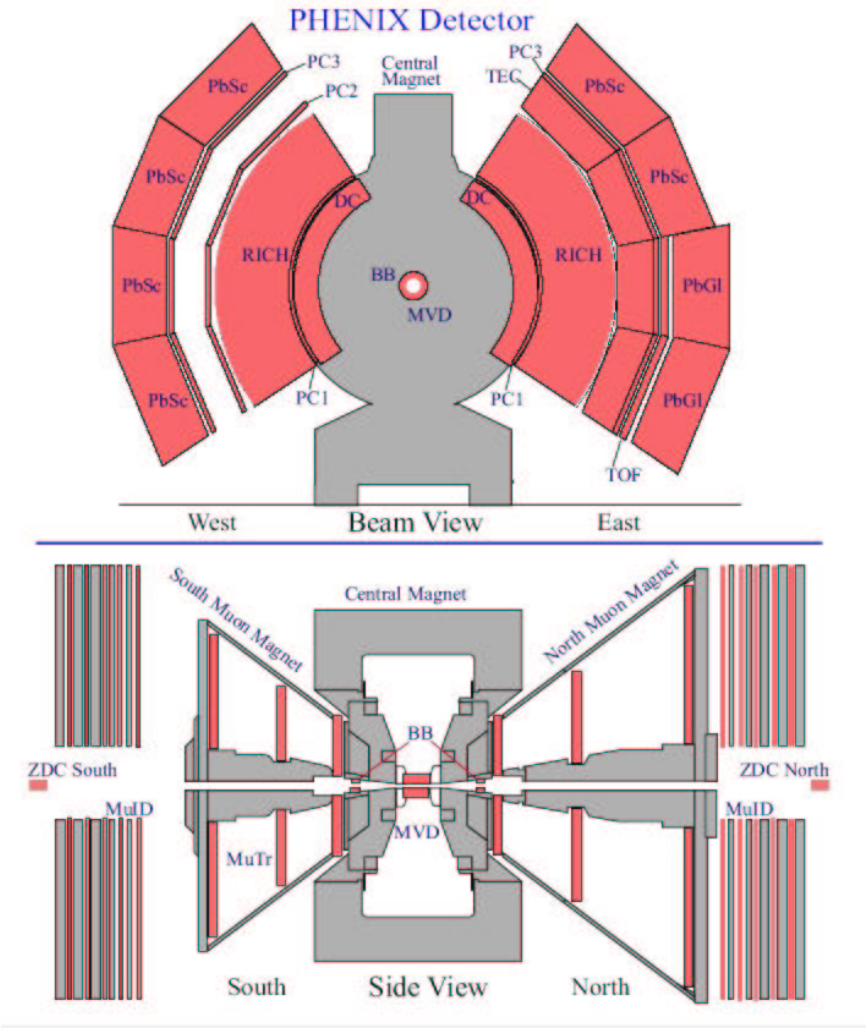

Figure 2.5 The PHENIX experiment overview : run3 configuration

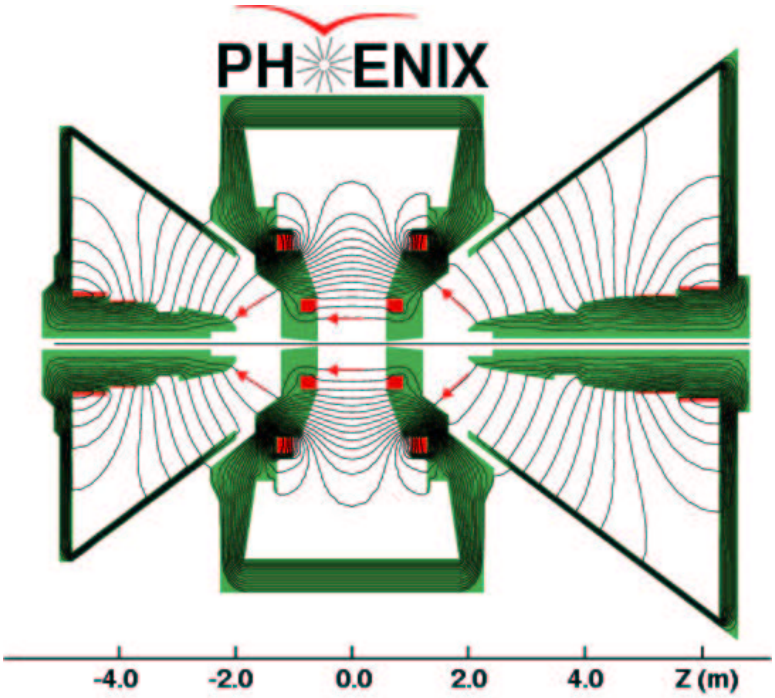

Figure 2.6 Magnetic field lines inside the Central and Muon Magnets

The Central Arms consist of three kinds of tracking chambers (Drift Chambers, Pad Chambers and Time-Expansion Chambers), Ring-Imaging Čerenkov Counters for the electron identification, Time-Of-Flight detectors for the particle-identification for hadrons, and Electro-Magnetic Calorimeters for measuring energies of electrons and photons. These detectors are positioned radially with respect to the z-axis extending from 2 m to 5 m. Details of operation and performance of the Central Arm detectors can be found in [126–128]. Descriptions of the analysis of the $J/\psi \to e^+e^-$ channel using the Central Arms are found in [129].

In addition to these four Arms, there are three kinds of counters to trigger p+p interactions which will be described in the next subsection followed by the subsection dedicated to description of the Muon Arms.

2.4 Interaction trigger counters

Three kinds of interaction-trigger counters (ITC) have been used to trigger p+p inelastic events and find vertices during the Run-2 p+p period. They are Beam-Beam Counters (BBC), Normalization Trigger Counters (NTC) and Zero-Degree Calorimeters (ZDC). Table 2.3 summarizes acceptance and performance of each ITC. Since trigger efficiency of the ZDC for p+p inelastic events is small (0.01), it was not used for the J/ψ analysis, hence will not be described here. Detailed information on the ZDC is found in [130]

Counters	Acceptance	Sensitive particle type	Typical efficiency	Typical vertex resolution (cm)
BBC	$3.0< \|\eta\| <3.9$ $\beta > 0.7$	charged particles	0.5	2
NTC	$1.1< \|\eta\| <2.8$	charged particles	0.6	10
ZDC	$\|\eta\| >6.2$	neutral particles	0.01	10

Table 2.3 Acceptances and performances of the interaction-trigger counters. Efficiencies and resolutions are for p+p inelastic events.

The Beam-Beam Counters

Two Beam-Beam Counters (BBC) have been used for the primary trigger and vertex counter for the p+p interactions. They are positioned 1.4 meters away from the interaction point along the beam axis on each side and cover from 2.4 to 5.7 degrees ($3.0 < |\eta| < 3.9$) with a full azimuth. They determine the vertex position of an event from the time difference between two counters. Figure 2.7 shows a photograph of a BBC. Each BBC consists of 64 hexagonal Čerenkov radiators each of which is mounted on a 1" photomultiplier tube (PMT). They are sensitive to charged particles whose $\beta \equiv v/c$ is greater than 0.7.

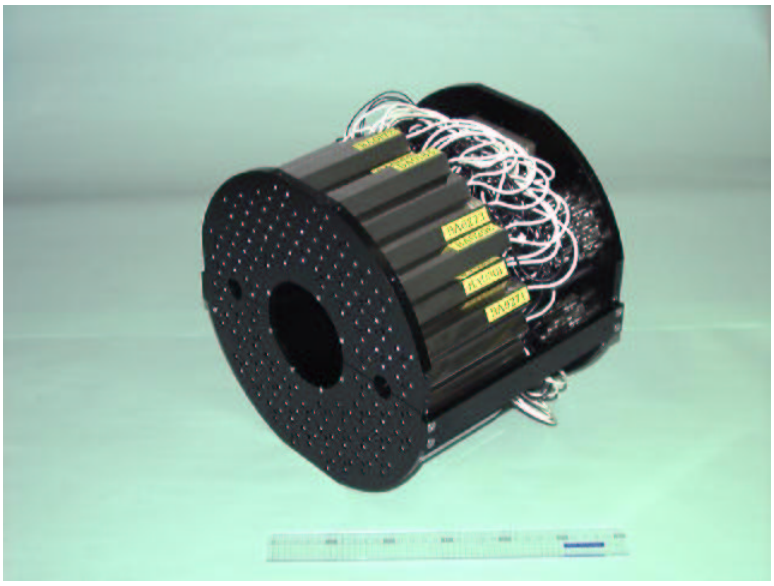

Figure 2.7 A photograph of a Beam-Beam Counter (BBC). Dimensions are 29 cm in outer-diameter and 25 cm in length.

With a beam test, intrinsic timing resolution of 50 psec was obtained for one module [131]. In Au+Au collisions, better vertex resolution is expected because hit multiplicity is higher. Actually 0.5-cm vertex resolution has been obtained in Run-2 Au+Au collisions. In p+p collisions, about 2-

cm vertex resolution is expected which is still good enough not to worsen invariant mass resolution for J/ψ particles measured in the Muon Arm. Trigger efficiency for p+p inelastic events is expected to be about 0.5, which will be discussed in section 3.

Beam-Beam Local-Level-1

Hit time information of all PMTs is sent to the Beam-Beam Local-Level-1 (BBLL1) board where a trigger decision is made. Online vertex position is obtained from hit time information without pulse-height corrections (threwing corrections). During the p+p run, a trigger is fired when there is at least one hit on both sides of the BBC counters and online z-vertex position $|z_{vtx}| < 75$ cm which is sufficiently large compared to offline vertex cuts (30 to 40 cm). Online vertices (without slewing corrections) and offline vertices (with slewing corrections) agree within the accuracy of the vertex determination (2 cm).

The Normalization Trigger Counters

Normalization Trigger Counters (NTC) have been introduced to increase trigger efficiency for p+p inelastic (including diffractive) events which is about 0.5 with the BBC only.

Each NTC is located on top of each side of the nosecone which is 40-cm away from the interaction point. Pseudo-rapidity coverage is $1.1 < |\eta| < 2.8$. It consists of four fan-shaped scintillators (called quadrants) each of which is mounted on a PMT to collect scintillation light emitted when a charged particle traverses. Single-particle detection efficiency obtained with a beam test is about 90% [132].

A simple NIM-logic makes NTC triggers using hit time information of all quadrants, which are sent to the Global-Level-1 board (see section 2.7). A trigger is fired when at least one quadrant on both sides has a hit. Trigger efficiency for p+p inelastic events is estimated with a simulation to be 60% by the NTC itself and go up to 74% when combined with the BBC where statistical errors of the simulation is 1%. Although NTC-triggered events without a BBC-trigger have not been used to increase the number of J/ψ's

because of its poor vertex-resolution (10 cm), they are used to confirm trigger efficiency of the BBC which will be discussed in section 3.

2.5 The Muon Arms

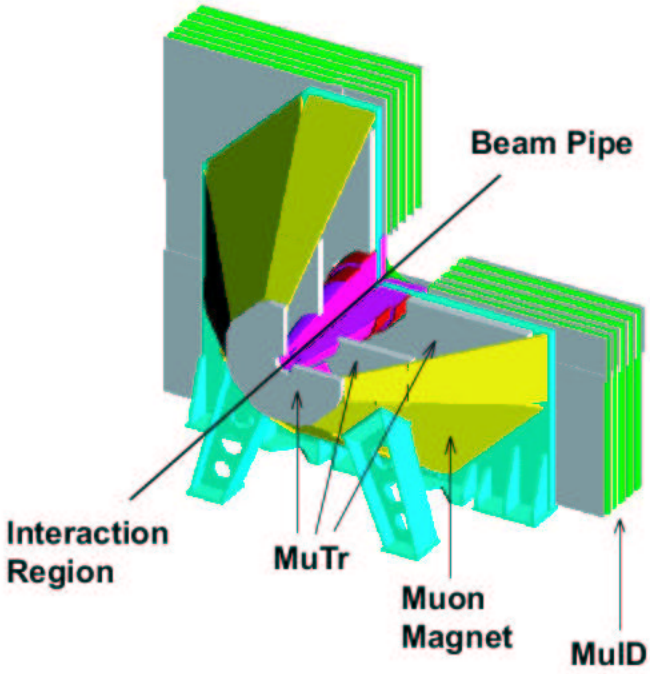

Figure 2.8 A schematic view of a Muon Arm. It consists of a conical magnet (Muon Magnet) with tracking chambers inside at three stations (Muon Tracker, or MuTr) and an array of chamber planes interleaved with absorbers (Muon Identifier, or MuID).

The PHENIX Muon Arms were designed to detect muon pairs from decays of vector mesons and Z^0 bosons produced in the forward rapidity region ($-2.2 < y < -1.2$ for the South Muon Arm and $1.2 < y < 2.4$ for the North Muon Arm) as well as single muons from (semi-)leptonic decays

of open heavy flavors and W bosons. Figure 2.8 shows a schematic view of a Muon Arm. Since only the South Arm was operational in Run-2, following descriptions specifically focus on it.

In this forward region, hadron background is relatively larger than that in the central region, since hadrons can be produced in soft processes with wider rapidity distribution than hard processes, while signal muons such as from heavy flavors are produced in hard processes. Good hadron rejection while keeping good momentum resolution is achieved with the following components of the Muon Arms and PHENIX.

1. Pre-rejection of hadrons with a five-interaction-length absorber of the nosecone and Central Magnet. Interaction length was determined not to degrade momentum resolution for low momentum (2 to 5 GeV/c) muons and to keep good mass resolution for J/ψ's. Hadron rejection factor of about 100 is achieved here.

2. Measurement of particle momentum with a magnetic spectrometer (Muon Tracking Chamber inside the Muon Magnet)

3. Further rejection of hadrons with an array of coarse-segmented tracking chambers and absorbers (Muon Identifier). Another factor of about 30 is achieved for the hadron rejection.

Figure 2.9 shows integrated nuclear interaction-length (λ_{int}) in the South Muon Arm as a function of the distance from the interaction point in the z direction. At the last MuID gap (gap 5), λ_{int} becomes 9.65. The minimum p_z (z-component of momentum) for a muon to reach gap 5 is 2.5 GeV/c.

2.5.1 The Muon Tracker

The PHENIX Muon Tracker (MuTr) comprises three stations of tracking chambers inside the Muon Magnet as shown in Fig. 2.5. Its design was driven by requirements from both heavy-ion physics and spin physics. The separation of each charmonium or bottomonium state from the others, J/ψ from ψ' for example, is essential to find QGP signal, since the degrees of suppression for each state are expected to vary because of different binding

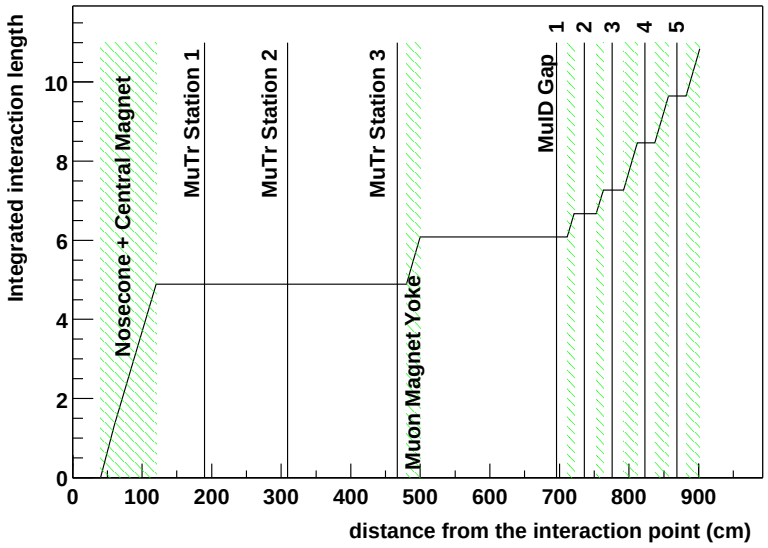

Figure 2.9 Integrated nuclear interaction-length of the absorbers in the South Muon Arm as a function of the distance from the interaction point in the z direction. Vertical lines indicate rough positions of the chambers. Hatched areas represent absorber materials.

radii. For spin physics, charges of high-p_T ($p_T > 20$ GeV/c) muons from W and Z boson decays are needed to be identified [85]. To satisfy the requirements above, 100-μm resolution is needed for chamber resolution. In addition, multiple cathode-strip orientations and read-out planes are required for each station to reconstruct tracks efficiently even in the most central Au+Au events. A MuTr electronics design was also driven by the requirement of 100-μm resolution measurements.

With 100-μm position resolution, momentum resolution $\Delta p/p = 3$ to 5% is achieved for 2 to 10 GeV/c muons as shown in Fig. 2.10. For low momentum (2 to 5 GeV/c) muons, multiple scattering is the dominant factor to smear muon momenta, whereas position resolution of chambers becomes dominant for high momentum (above 10 GeV/c) muons. Polar angle dependence of momentum resolution for high momentum muons is due to the difference in magnitudes of the magnetic field inside the South Muon Magnet as shown in Table 2.4.

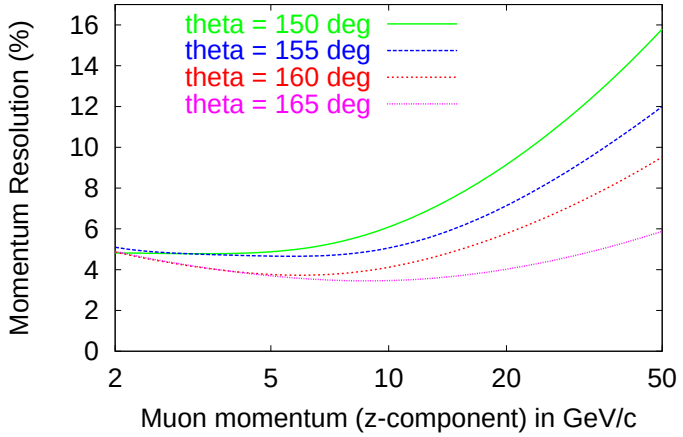

Figure 2.10 Momentum resolution for muons with different polar angles in the South Arm acceptance as a function of p_z obtained with a simulation. Typical statistical errors of the simulation is 5%.

Polar angle in degrees	165	160	155	150
Integrated magnetic field in T·m	0.774	0.494	0.344	0.255

Table 2.4 Integrated magnetic field inside the South Muon Magnets.

Mechanical design

All chamber planes inside the Muon Magnet are perpendicular to the z-axis. Their z-positions for each station are shown in Fig. 2.9. The magnetic field is in the radial direction so that charged particles from the interaction vertex bend primarily in the azimuthal direction, which is perpendicular to the direction of cathode strips to determine the track positions. Typical bend from the straight line at station 2 is 1 cm for medium-momentum (5 to 10 GeV/c) muons.

In one MuTr station there are three (or two) gaps each of which consists of two cathode-strip planes and one anode-wire plane in between with a 3.2-mm anode-cathode spacing. Figure 2.11 shows a cross section of a MuTr station. Station 3 has only two gaps because it can exploit additional two-dimensional position information of MuID roads. All gaps are divided into octants electrically as shown in Fig. 2.12 together with octant numbers. For station 2 and 3, octants are also the unit of mechanical assemblies while quadrants are for station 1. Figure 2.13 shows a photograph of a station-2 octant. An octant is further divided into two half-octants in the middle, in each of which directions of anode wires and cathode strips are fixed.

A cathode plane consists of 5-mm width strips with alternate readout to avoid cross-talks between them. An anode plane is an alternating structure of 20-μm gold-plated tungsten sense wires and 75-μm gold-plated Cu-Be field wires with a sense wire spacing of 10 mm(see a typical cathode strip chamber schematic view in Fig.2.14). Anode wires run in the azimuthal directions while cathode strips run in the radial directions. The direction of cathode strips in one plane of each gap is perpendicular to that of the anode-wires (called a non-stereo angle plane), with a goal of 100 μm position resolution. The direction of cathode strips in the other plane of the gap (a stereo angle plane) is tilted by 3.25 to 11.25 degrees depending on gap and

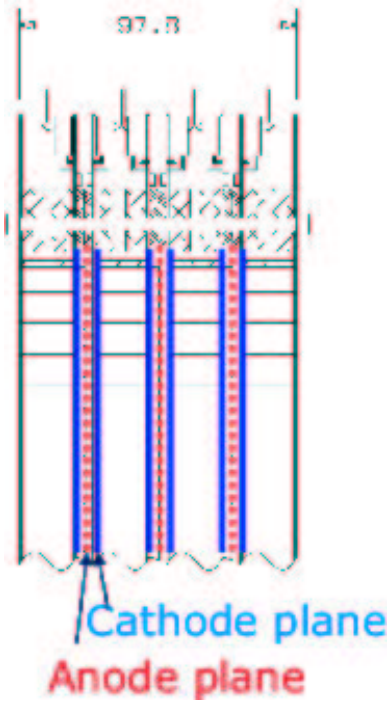

Figure 2.11 Cross section of a MuTr station. One MuTr station consists of two or three gaps, each of which has one anode-wire and two cathode-strip planes.

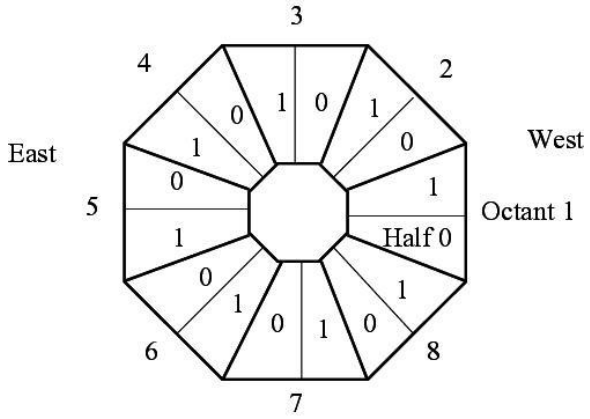

Figure 2.12 Octant and half-octant structures of a MuTr gap. The beam line passes at the center of this figure. The bold lines show the boundaries for octants and this lines for half-octants. Octant and half-octant numbers are also shown. For the South Arm, the left-hand side in the figure (octant-5 side) corresponds to the east direction.

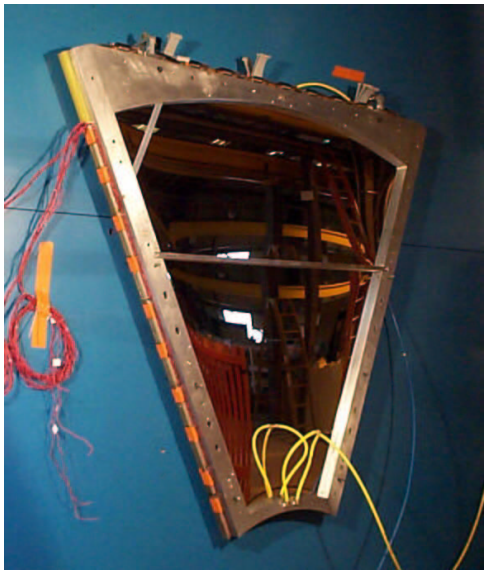

Figure 2.13 A photograph of a MuTr station-2 octant. A cathode plane is made of etched 25-μm copper coated mylar foils.

station, which are summarized in Table 2.5 and illustrated in Fig. 2.15 for station-1 planes.

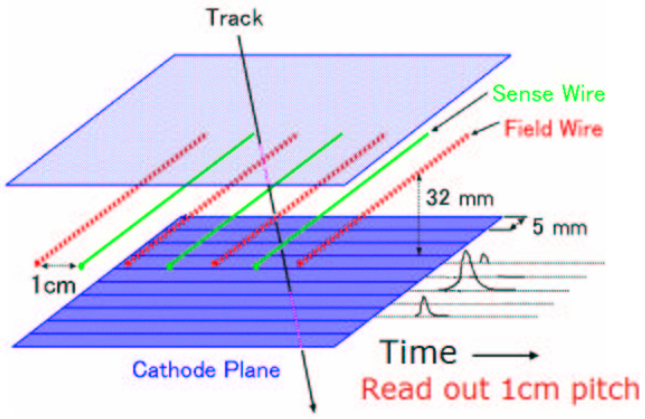

Figure 2.14 Typical cathode strip chamber operation.

Resolutions of stereo-angle planes are worse (300 μm) but they are needed to determine 3-D positions of hits and reject ghost tracks.

Specific technologies were used for each station to produce a cathode pattern to an accuracy of better than 25 μm; photo-lithography for station 1, electro-mechanical etching for station 2 and mechanical routing for station 3. A unique wire laying apparatus was designed and implemented for each station.

In order to reduce the multiple scattering in the spectrometer which degrades momentum resolution, thickness at the station 2 detector was required to be less than 10^{-3} of a radiation length. To meet this requirement, the station-2 octant cathodes were made of etched 25-μm copper coated mylar foils. The thickness of the copper coat is 600 Å. As a result, the total thickness of 8.5×10^{-4} radiation lengths is achieved which satisfies the requirement.

The chamber gas mixture was 50% Ar + 30% CO_2 + 20% CF_4 with a gas recirculation system included in normal operation. The nominal high-voltage potential applied to anode wires was 1850 V with a gain of approx-

Station	Gap	angle (degree)
1	1	-11.25
	2	$+6$
	3	$+11.25$
2	1	$+7.5$
	2	$+3.75$
	3	$+11.25$
3	1	-11.25
	2	-11.25

Table 2.5 Relative angles of the cathode strips in stereo-angle planes with respect to the non-stereo angle (radial direction). Positive signs represent the positive ϕ direction (counter-clockwise) for all half-octants in station 1 and half-octant 0 in station 2 and 3, while the negative ϕ direction for the others.

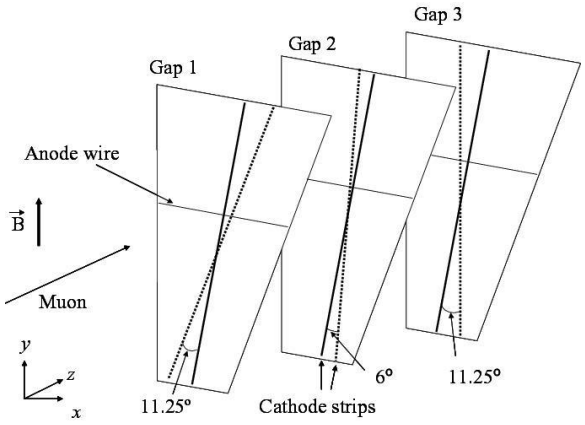

Figure 2.15 Directions of cathode strips and anode wires in station-1, octant-2, half-octant-0 planes. Bold lines show cathode strips in non-stereo-angle planes. Dotted lines show cathode strips in stereo-angle planes with angles shown in Table 2.5. Angles in the figure are not exact.

imately 2×10^4.

To maintain good momentum resolution, an optical alignment system has been installed to calibrate initial placement of the chambers, and to monitor displacement of the chambers during their operation to ± 25 μm. There are seven optical beams surrounding each octant chamber, consisting of an optical-fiber light source at station 1, a convex lens at station 2 and a CCD camera at station 3 which are shown in Fig. 2.16.

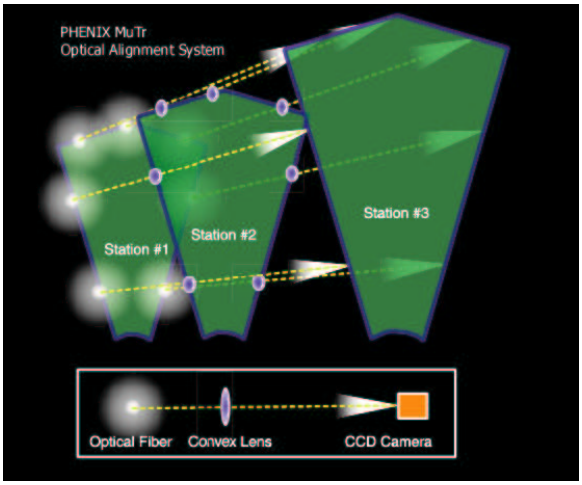

Figure 2.16 The optical alignment system in which light from an optical fiber is projected from station 1 through station 2 to a CCD mounted on station 3. The relative chamber positions are monitored to ± 25 μm.

Electronics design

Figure 2.17 shows a schematic diagram for the MuTr Front End Electronics (FEE). Raw chamber signals are continuously amplified by CPAs (Charge Pre-Amps) and stored in AMUs (Analog Memory Units) with 64-event buffers with the 10-MHz beam clock. Upon receipt of a level-1 trigger bit from a Granule Timing Module (GTM), stored samples of all channels are digitized by 11-bit ADCs (Analog to Digital Converters) and the results

are sent to a Data Collection Module (DCM) through a Front End Module (FEM). GTMs and DCMs are described in section 2.6.

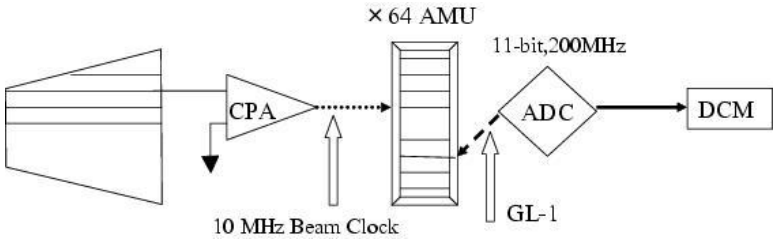

Figure 2.17 A schematic diagram for the MuTr Front-End Electronics (FEE). Raw chamber signals are continuously amplified with CPAs (Charge Pre-Amps) and stored in AMUs (Analog Memory Units). Upon receipt of a level-1 trigger bit from a GTM (Granule Timing Module), stored samples from all channels are digitized by ADCs (Analog to Digital Converters) and the results are sent to a DCM (Data Collection Module).

Four ADC samples are used to determine the amount of the charge deposited on a strip to reject noise hits as much as possible. Each sample is measured for the duration of 100 nsec. The second sampling starts 400 nsec after the first sampling ends. Second to fourth samplings are consecutive. Timing has been set so that the third sample comes to the peak of the pulse as shown in Fig. 2.18. Relative charges (or ADC counts) of these samples have been monitored online to guarantee peak positions not to move around from the third sampling. The amount of the peak charge of a strip is obtained offline as the average of the second to fourth samples with a pedestal subtracted. These four samples are converted within 40 μsec per event.

Strip by strip calibration is crucial for good position resolution, since a position of a muon track is determined by fitting charges on typically 2 or 3 consecutive strips induced by the track, which will be described in section 3.2.2. A calibration system has been implemented to inject pulses into all of the chambers. Four wires in each chamber gap, which span the entire width of the cathode planes, are sent a square pulse from a digital to analog converter (DAC), thus inducing a charge on all cathode strips in a

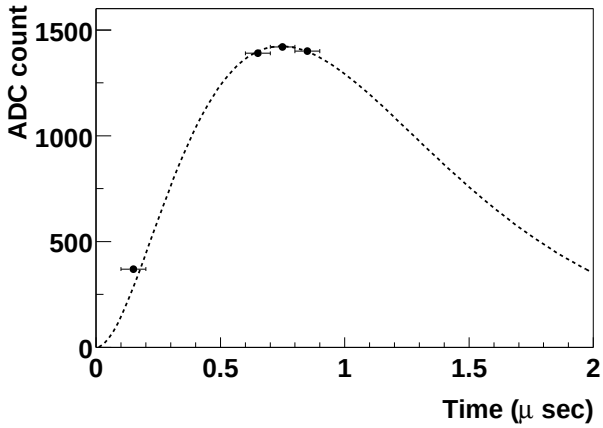

Figure 2.18 Typical ADC counts for each sampling together with a typical signal pulse (dotted line). The horizontal axis is for the relative sampling time. One ADC count corresponds to about 0.5 fC (10^{-15} Coulomb).

given gap simultaneously. Several different pulse amplitudes are sent to the chambers and many events are collected at each amplitude so that relative gains of the cathode strips can be determined over the entire range of the electronics. Pedestals are monitored by collecting calibration data with the DAC amplitude set to zero.

To meet the design requirement of 100-μm resolution, rms noise at the input to the preamps is required to be 0.5 fC for a typical pulse of 80 fC, which is achieved in a test bench measurement described next.

Integrated performance

Integrated performance of chambers and electronics has been studied in a cosmic-ray test in a test stand with one station-2 chamber and its full complement of electronics, and in readout of the entire South MuTr system prior to Run-2. The cosmic-ray test data showed that the system was capable of meeting the noise specifications and that 100-μm resolution could be achieved. The noise specifications have been met on the full South MuTr

system and the system has been shown to be robust over several months of data taking.

The cosmic-ray test was performed with one station-2 chamber, 960 channels of production front-end electronics, the same high-voltage and low-voltage distribution system that is used in the final system, and with a copy of the PHENIX data acquisition system. The noise specifications of 0.5 fC (1 ADC count) were met, as can be seen in Fig. 2.19, where the rms values of the pedestals on all readout channels are shown. Noise environment in situ has turned out to be similar to this test except for chambers in station 2, which has caused degradation of the mass resolution for J/ψ in Run-2.

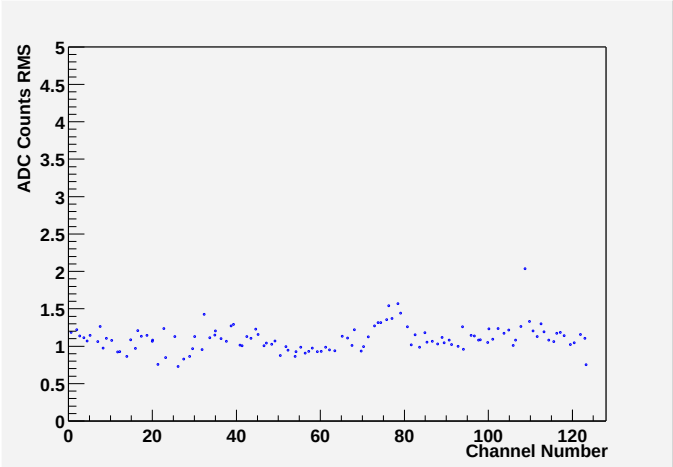

Figure 2.19 Measurement of rms noises for 128 typical channels in units of ADC counts (1 ADC count is roughly 0.5 fC) obtained in the cosmic-ray tests for a station-2 octant.

Two scintillators, one on either side of the station-2 chamber, were used to provide a trigger for cosmic rays going through the chamber. The data collected from this trigger were searched for clusters in each cathode readout plane, the clusters were fit to extract the centroid strip positions, and 5 out of 6 readout planes were fit to a straight line and projected to the sixth, central non-stereo readout plane. A cut was placed on the straight line fit to only the select tracks which were approximately perpendicular to the face of

the chamber and the difference between the projected straight-line fit and the measured position on the sixth plane was plotted. The result is shown in Fig. 2.20, where a resolution of approximately 100 μm was achieved when the projection error, position resolution for a track obtained with the other five planes, is removed from the residual.

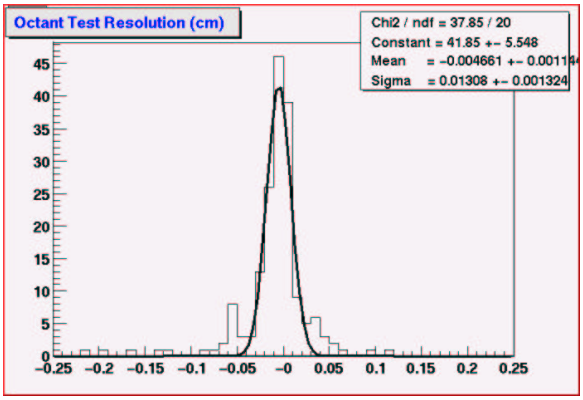

Figure 2.20 Measurement of position resolution obtained in cosmic-ray tests of a station-2 octant. The composite chamber plus projection error (position resolution for a track obtained with the other five planes) was about 131 μm, consistent with the 100 μm specification for the chambers and readout alone.

Each individual channel's gain, pedestal and variation (or noise) in the pedestal were measured. The dynamic range in the charge measurement of the system was verified and long runs demonstrated the stability of the optical links from FEMs to a DCM. Figure 2.21 shows the residuals from a gain measurement during the commissioning period. The residuals are shown to be consistent with a linear gain to a few ADC counts over the operable ADC range.

2.5.2 The Muon Identifier

The Muon IDentifier (MuID) consists of five layers of chambers interleaved with steel absorbers. Each chamber plane is called gap 1 through gap 5

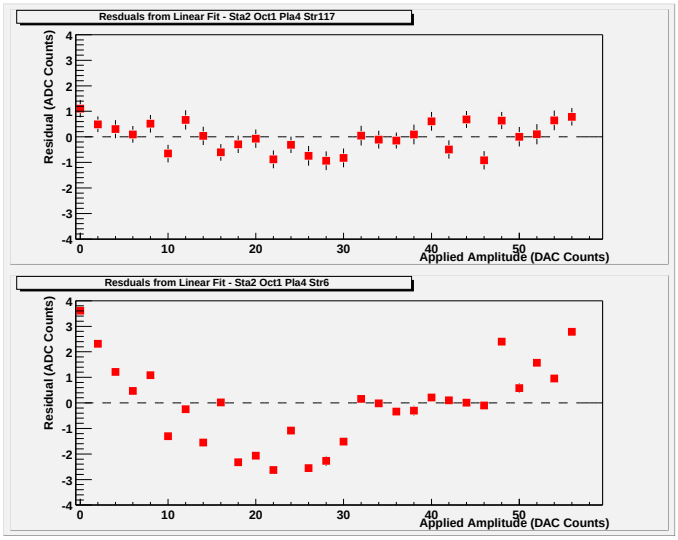

Figure 2.21 Residuals (in ADC counts) from a straight-line fit to the charge measured on a given strip of the ADC vs the DAC pulse amplitude applied to the calibration wires. Two different strips from a given cathode plane are shown. Approximately one half of the ADC range (of 2047 channels) is shown and is linear to a few ADC counts and constant over time.

starting from the nearest gap to the interaction point. The MuID is used for separating muons from charged hadrons and other background as well as providing triggers for single muons and dimuons (muon pairs). It gives another hadron rejection factor of about 30 in addition to the Central Magnet and nosecone (about 100), thus reducing the mis-identification rate for the punch-through hadrons to 3×10^{-4}. This is much smaller compared to the irreducible hadron weak-decay background ($\pi \to \mu\nu$ and $K \to \mu\nu$) in flight before the nosecone for near-threshold momentum (3 GeV/c) muons (3×10^{-3}). Minimum p_z for a muon produced at the interaction vertex to reach the MuID is 1.8 GeV/c and 2.5 GeV/c to penetrate through it.

Segmentation of the absorber into multiple layers improves the measurement of the trajectory in the MuID gaps (chamber layers) for low momentum muons, which is desirable to increase the acceptance for the ϕ meson detection. The segmentation chosen is 20 cm, 10 cm, 10 cm, 20 cm and 20 cm starting from the South Magnet backplate as shown in Fig. 2.9. In each gap between these absorbers, chamber panels are installed.

Mechanical Design

One MuID plane, or a gap, consists of six panel structures (called MuID panels) as shown in Fig. 2.22, into which chambers are assembled in both horizontal and vertical orientations. The upper figure of Fig. 2.23 shows the cross section of a MuID panel.

Iarocci-type plastic tubes have been chosen as MuID chambers for longevity, robustness and low cost to cover a large area (13×10 m^2 for each Arm). One tube has eight cells with a 9×9-mm^2 cross section each of which has a gold-coated CuBe anode-wire with a 100-μm diameter at its center. The lower figure of Fig. 2.23 shows the cross section of an Iarocci tube (in this figure, two tubes, or a two-pack is shown which will be explained later). The cathode wall is made of polyvinyl chloride (PVC) coated with carbon. Length of a tube varies from 2.5 m to 5.6 m depending on its position to be installed.

Tubes are operated in the proportional mode with 4300 to 4500 V potentials and isobutane-CO_2 mixed gas, where a gain of approximately 2×10^4 is achieved. As test-bench results, 92 ± 1 % efficiency, which was also mea-

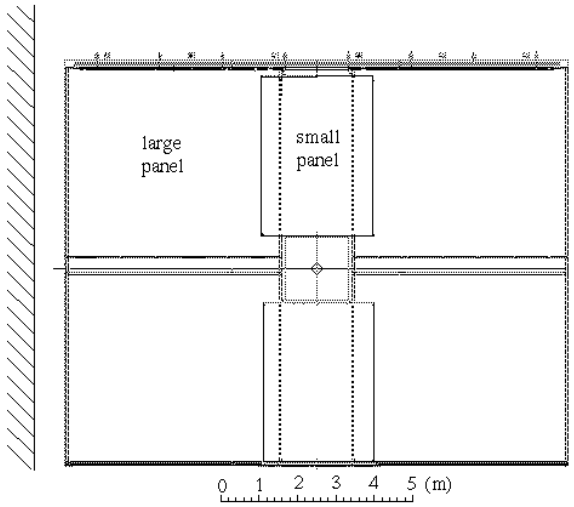

Figure 2.22 Configuration of MuID panels in one gap. The beam axis runs in the middle perpendicularly to the paper.

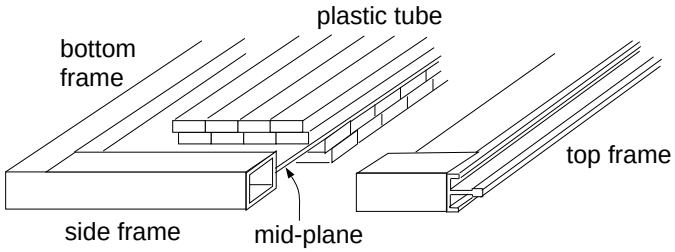

Cross section of the MuID panel

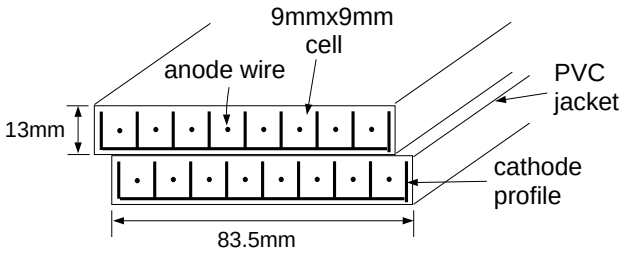

Cross section of the plastic tube(2-pack)

Figure 2.23 Cross section of a MuID panel (upper) and an Iarocci tube (lower). In one panel-orientation, there are two layers with independent gas and high-voltage chains. Two adjacent tubes in those layers make one signal channel to be read out.

sured in the beam test to be described later, and 80 nsec (nano-seconds) drift time width were obtained. To achieve a better efficiency and faster drift time, two tubes with a half cell (5-mm) shift consist one channel (called a 2-pack) as shown in Fig. 2.23. For a 2-pack, 97 $\pm$ 1 % efficiency and 60 nsec (nano-seconds) drift time have been obtained [134]. Drift time is faster enough than the bunch-crossing interval (106 nsec), so that a level-1 trigger can uniquely determine the bunch crossing in which an event has occurred. Gas mixture ratio is adjustable between 0 to 25% for isobutane. In Run-2 it has been set to 7% to meet the non-flammable requirement of PHENIX.

Iarocci tubes are assembled in a panel structure called a MuID panel which consists of Al frames, cover plates and a mid-plate (shown in the upper figure of Fig. 2.23). Iarocci tubes are glued to both sides of a 3-mm width Al mid-plate with double-sided tapes at 8.4-cm intervals for both horizontal and vertical orientations. Each orientation has two chamber layers shifted by a half cell (5 mm) to make 2-packs. Those layers have independent chains for gas and high-voltage supplies to minimize the number of dead channels.

There are two kinds of the panel size which are $5.6 \times 5.2\ \mathrm{m}^2$ (large panel) and 4.4 (or 4.2) $\times$ 2.9 m^2 (small panel). In one gap, four large panels and two small panels are installed as shown in Fig. 2.22. Adjacent panels overlap with each other so that there is no inactive area between them.

Electronics Design

A passive OR of signals of 16 wires in a 2-pack is read out and amplified by a factor of 150 with an in-panel amplifier on a high-voltage distribution board which also provides high voltage to each tube. Signals are then sent to the MuID Front-End Electronics (FEE) where they are again amplified by a factor of 3, discriminated and stored in the data buffer. Discriminator threshold values have been set to 90 mV to minimize the number of noise hits while keeping good efficiency (typical pulse height of signals is 500 mV to 1 V). Upon receipt of a level-1 trigger, all digitized bits are sent to a DCM. There is additional output of the MuID FEE called "pseudo-trigger output" which is grand logical OR of a certain fraction of channels. They are used for the NIM-logic level-1 trigger which is described in section 2.5.2.

Integrated performance

To confirm hadron-rejection performance and muon detection efficiency of the entire MuID system experimentally, a beam test was performed at KEK-PS [1] using the same type of Iarocci tubes and steel absorbers in the same configuration as in PHENIX.

Figure 2.24 shows the experimental setup for the beam test. Pion and muon beams were produced by bombing an inner target with 12-GeV proton beams, then 1-4 GeV/c momentum was selected with the magnet system and delivered to the experimental area. Four scintillation counters (ST1 to ST4) defined the beam. Three gaseous Čerenkov counters (GC1 to GC3) identified pions and muons. GC1 and GC2 were pressured to distinguish between pions and muons and GC3 to distinguish between muons and electrons. Beam qualities obtained were better than 99% for muons and better than 99.9 % for pions excluding their weak decays ($\pi^{\pm} \rightarrow \mu^{\pm}\nu$) after GC2. Five iron slabs were used with a width of 10 cm, 10 cm, 10 cm, 20 cm and 20-cm respectively staring from the upper stream. An additional 10-cm (20-cm) plate was added in front of the first layer to simulate the backplate of the South (North) Muon Magnet. The numbers of Iarocci tubes used were 3, 3, 5, 7 and 9 starting from the first gap for each orientation. They were optimized to 3σ dispersion of 2-GeV/c momentum muons due to multiple scattering.

As a result, muon detection efficiency of 86 $\pm$ 2 % has been obtained for 1.8-2.5 GeV/c muons with a small momentum dependence. This is slightly lower than the test bench result described before (92 $\pm$ 1 %), which is explained by additional inactive volumes between tubes. Figure 2.25 shows the results of pion mis-identification rate as a function of pion momentum, which is consistent with a GEANT [135] simulation including weak decays into muons. For the South Arm, mis-identification rate for 4-GeV/c momentum pions (about 5 GeV/c at the interaction region) has been determined to be 0.04 excluding decays. Multiplying the rejection factor of the nosecone and Central Magnet ($e^{-5} \sim 7 \times 10^{-3}$), the net mis-identification rate of 3 $\times 10^{-4}$ is obtained, which satisfies the design value.

[1] Proton Synchrotron at High Energy Accelerator Research Organization, Japan

Figure 2.24 Setup for the MuID beam test carried out at KEK-PS. Four scintillation counters (ST1 to ST4) define the beam. Three gaseous Čerenkov counters (GC1 to GC3) identify pions and muons.

The MuID NIM-logic trigger for LVL-1

A coarse-segmented trigger system called the MuID NIM-logic trigger[2] was used to trigger muons in the Muon Arm during the Run-2 and Run-3 period. Figure 2.5.2 shows a schematic view of the system.

As shown in the figure, all the MuID planes are divided into four regions (called quadrants) by horizontal and vertical lines through the middle. A trigger decision for a quadrant, that is, whether a muon has passed or not, is made by taking the coincidence of fired planes of the quadrant. Since the number of input channels of the trigger circuit is limited, only four gaps out of five were used. Deeper gaps (gap 3,4 and 5) were included since they are more important for muon identification than shallower gaps. Gap 1 was also included since (1) better tracking performance due to longer tracking length and (2) better rejection of cosmic rays and very low angle ($\theta < 9$ degrees) particles. The chance for a muon to cross more than one quadrant is small. Each quadrant is further divided into two sectors for both horizontal and vertical tube orientations. Figure 2.27 shows the segmentation for each gap. An output of each sector, grand OR of all channels inside, corresponds to a

[2]So named because the trigger circuit is constructed using NIM- and CAMAC-standard electronics.

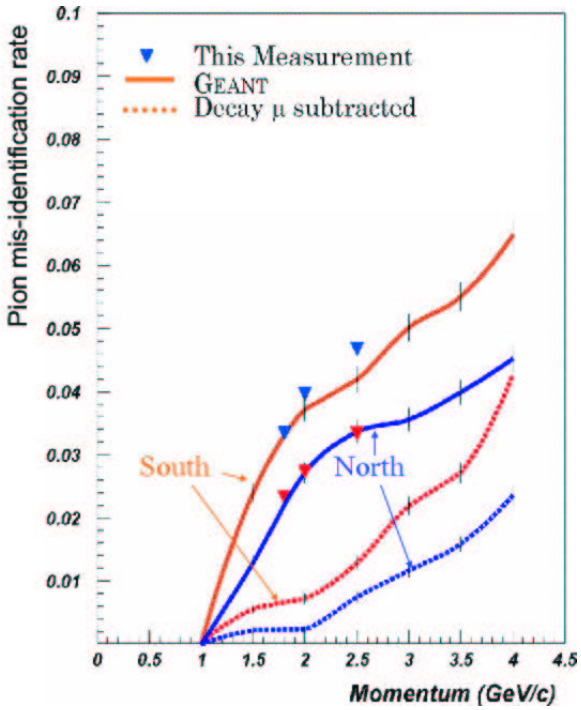

Figure 2.25 Pion mis-identification rate as a function of pion momentum for both the South and North Muon Arms obtained with the beam test at KEK. The solid (dotted) lines show simulation results including (excluding) $\pi^{\pm} \rightarrow \mu^{\pm}\nu$ decays.

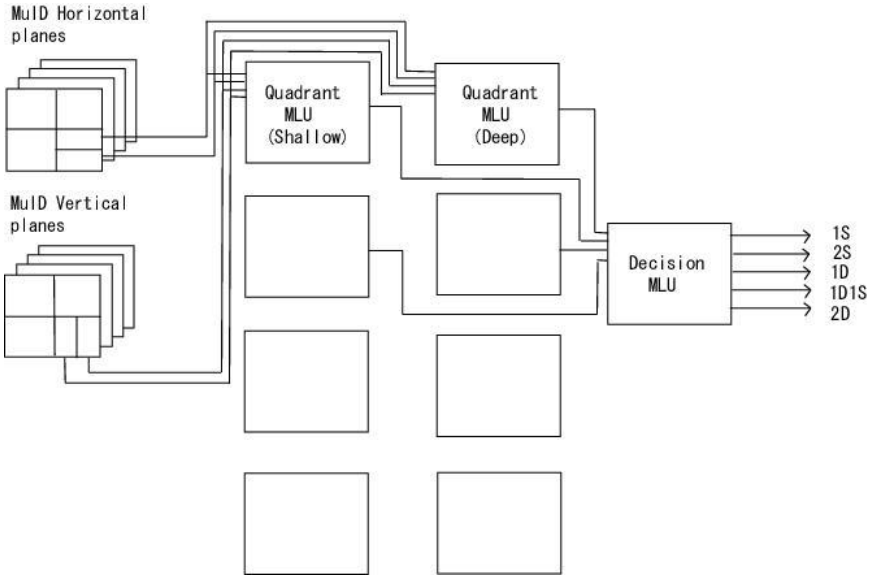

Figure 2.26 Schematic diagram of the MuID NIM-logic trigger. Each "Quadrant" MLU takes 16 (4 for each gap) output signals from the MuID FEE (Front-End Electronics). The "Decision" MLU takes output signals of all the "shallow" and "deep" quadrant MLUs and generates final trigger bits, which are 1S (single shallow), 2S (double shallow), 1D (single deep), 1D1S (deep-shallow) and 2D (double deep), as PHENIX Global-Level-1 input.

pseudo-trigger output of a ROC. in total, 16 pseudo-trigger output signals are sent to the trigger algorithm.

D	B	B	D
C	A	A	C
C	A	A	C
D	B	B	D

Figure 2.27 Segmentation of a MuID plane for the NIM-logic trigger. Bold lines divide quadrants and thin lines divide segments in each quadrant. Capital letters represent positions of each segment and used in the text.

Trigger decisions are made by LeCroy 2372 Memory Lookup Units (MLUs) for each quadrant. Two MLUs are prepared for each quadrant for both "deep" and "shallow" triggers. A deep trigger requires hits in all four gaps used and a shallow trigger requires hits up to gap 3. Hit patterns are required to point to the event vertex. Hit patterns such as A-A-B-B and A-C-D-D are accepted but B-B-A-A and D-A-A-C are not, for example, where four letters represent hit segments in a quadrant shown in Fig. 2.27 for each gap starting from the first gap. An example of an accepted-pattern is shown in Fig. 2.28. To minimize the loss of trigger efficiency due to finite chamber efficiencies, the algorithm allows some gaps to miss hits. For a deep trigger, 6 out of 8 gaps (including both orientations) are required to have a hit and 3 out of 4 gaps for a shallow trigger. Extra hits are allowed, thus no efficiency loss is expected due to background hits.

Total 8 quadrant trigger signals are sent to another MLU, called the "Decision MLU", which counts the number of triggered quadrants and issues five trigger signals:

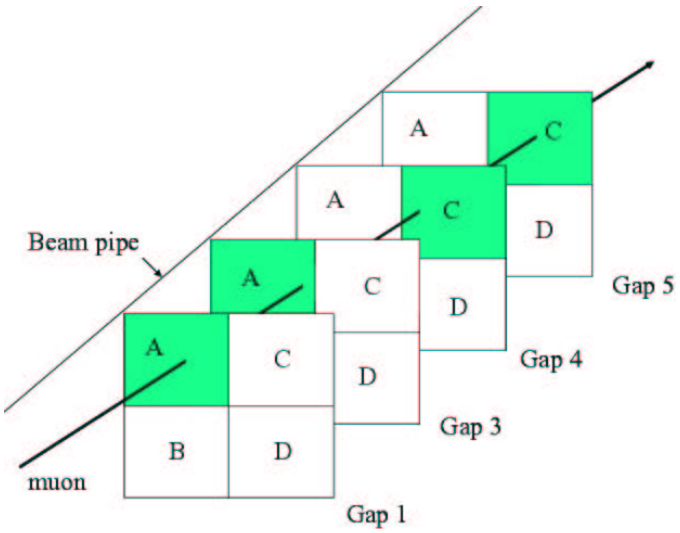

Figure 2.28 An accepted-pattern example of the MuID NIM-logic trigger. Capital letters represent positions of each segment. Gap 2 was not used because of the limitation of input channels of the trigger logic.

(1) single shallow (1S) – one shallow quadrant is fired,
(2) double shallow (2S) – two or more shallow quadrants,
(3) single deep (1D) – one deep quadrant,
(4) deep-shallow (1D1S) – one deep quadrant and one or more shallow quadrants, and
(5) double deep (2D) – two or more deep quadrants,

which are sent to the Global Level-1. A shallow quadrant-trigger is fired always when the deep quadrant-trigger is fired for that quadrant. Therefore, the following relations hold true: 2D $\subseteq$ 1D1S $\subseteq$ 1D $\subseteq$ 1S where A $\subseteq$ B denotes that the trigger B is always fired when the trigger A is fired. The reasons to have both shallow and deep triggers for each quadrant are (i) to achieve higher $J/\psi \to \mu^+\mu^-$ efficiency obtained with the 1D1S trigger than the 2D trigger by 30% and (ii) to study hadron punch-through background with the 1S and 2S triggers (not described in this paper).

2.6 The PHENIX DAQ system

Figure 2.29 shows a schematic view of the PHENIX Data Acquisition (DAQ) System. All the subsystems are equipped with the timing modules called Granule Timing Modules (GTMs). The Master Timing Module (MTM) delivers the 9.4-MHz RHIC clock to GTMs. When a trigger is issued by the Global Level-1, the clock and trigger bit are transported over optical fibers to the electronics of each detector, the Front End Module (FEM). The detector records the data in raw digitized format and transports the data packets over optical fibers to the Data Collection Module (DCM). The data are recorded in a buffer disk in the PHENIX control room where data quality is monitored online. At the maximum 60 mega-bytes per second has been achieved as a rate of recording data in the disk which corresponds to about 1200 events per second for p+p data whose size is about 50 kilo-bytes per event. The data are then transferred and stored in a huge storage tape with 1.2×10^{15} bytes capacity (sharing with other RHIC experiments) for offline computing such as calibration and track reconstruction.

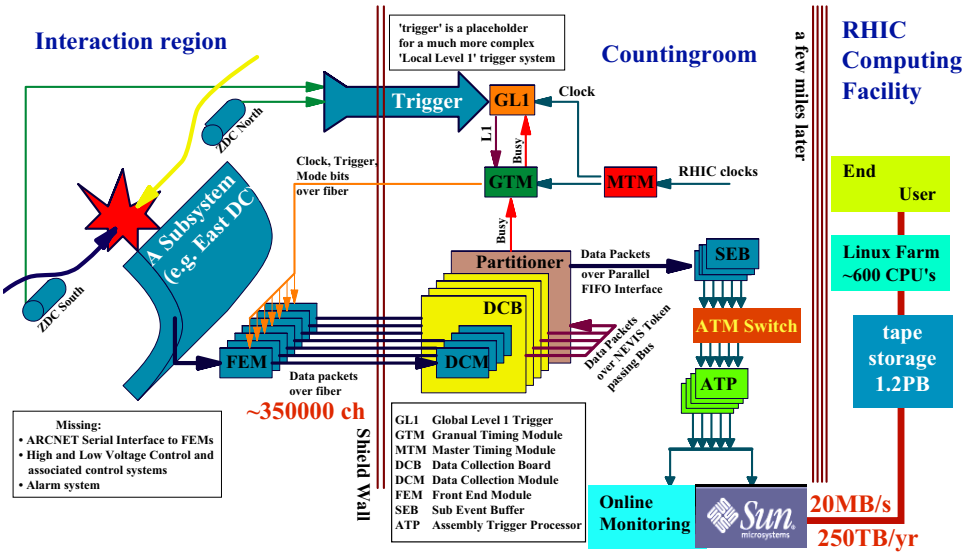

Figure 2.29 The PHENIX data acquisition system, triggered by an event in the Zero-Degree Calorimeters (Left in diagram)

2.7 Global Level-1 triggers

The level-1 triggers of PHENIX are issued by the Gglobal Llevel-1 (GL1) module, for which local level-1 and NIM-logic triggers from various subsystems are input. The maximum DAQ rate (about 1 kHz) and the number of triggers (10 or more) limit the rates for each GL1 trigger to about 100 Hz or less. Level-2 triggers were not used during the p+p and d+Au Run.

2.7.1 Minimum bias trigger

Logical OR of the BBC (BBLL1) and NTC triggers, called the "Minimum Bias (MB)" trigger was used to trigger p+p inelastic events with about 70% efficiency. MB-triggered events are useful for studying detector efficiency and background as well as extracting physics. At the highest luminosity of RHIC achieved in Run-2 (10^{30} cm^{-2} sec^{-1}), MB trigger rate was typically 10^{30} cm^{-2} sec^{-1} $\times$ 42 mb $\times$ 0.7 = 30 kHz. We have applied a prescale factor to this trigger depending on its rate to keep the DAQ rate below an affordable level. Here a prescaled factor F is an integer number and defined as

$$F = \frac{\text{Number of triggers when the DAQ is alive}}{\text{Number of events recorded}} - 1.$$

During the run, F = 19 to 79 were applied to the MB trigger.

2.7.2 Muon triggers

Two kinds of muon-related triggers were prepared for physics triggers:

(A) MB $\otimes$ 1D for the single muon trigger and

(B) MB $\otimes$ 1D1S for the dimuon trigger,

where $\otimes$ stands for logical AND, "1D1S" and "1D" have been already explained in section 2.5.2.

The rate of the single muon trigger was usually less than 100 Hz and consistent with that of the irreducible hadron-decay background before the nosecone (1/1500 of the minimum bias rate) within a factor of two. However, we sometimes observed abnormally high ($\sim$1 kHz) rates. This was found

to be due to blown-up beams which hit the beam pipe and produced high-energy secondary particles (including muons) sailing through the MuID. (This background can be rejected with a vertex cut for offline analysis.) We used this trigger with $F = 4$ when the trigger rate was too high. Rates of the dimuon trigger were typically about 1/10 that of the single muon trigger and never beyond 100 Hz. Therefore no prescale factor was applied to the dimuon trigger that has been used for the J/ψ analysis described in the next section.

Figure 2.30 shows Trigger Circuit (TC) efficiencies (ε_{TC}) for 34 runs randomly selected from the runs used for the run-II J/ψ analysis. The efficiencies ε_{TC} reflect the inefficiency of the hardware trigger circuit. It is defined as

$$\varepsilon_{TC} = \frac{\text{number of events with both hardware and software triggers}}{\text{number of events with software triggers}}$$

using MB-triggered events, where a hardware trigger equals the NIM-logic trigger output (GL1 input) and a software trigger is a result of the software which emulates the trigger algorithm. On average, an efficiency of 96.8 % has been obtained for the single muon trigger and 98.7 % for the dimuon trigger with small statistical errors ($< 0.1\%$). The inefficiency for the dimuon trigger, 1.3%, is much smaller than other errors on the cross sections for J/ψ production, which will be described in the next section. Inefficiencies are ascribed to hardware dead time which depends on the trigger rate. A simple model calculation, in which all efficiency loss is assumed to be due to the dead time, reproduces ε_{TC} for the single muon trigger well, as shown in Fig. 2.31. This consistency ensures that both hardware and software triggers worked as expected.

2.8 Online Monitoring

Conditions of the detectors in PHENIX have been continuously monitored online throughout the run to keep the quality of data. Monitoring of high-voltage (HV) status and data qualities are described in the following. In

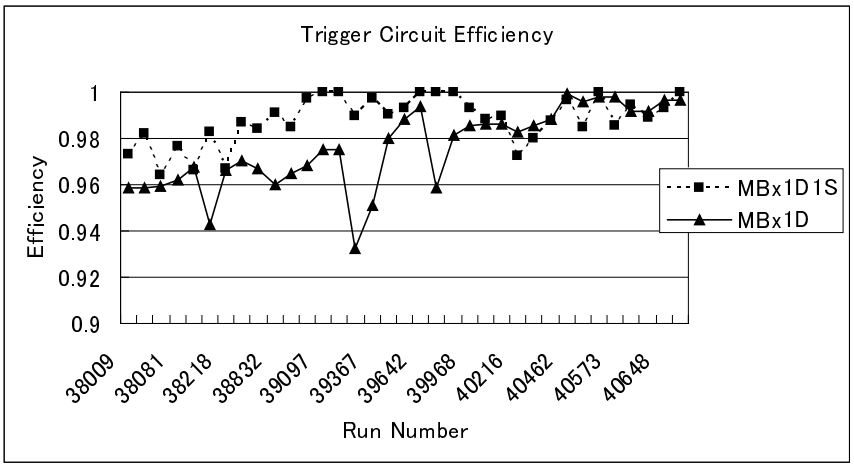

Figure 2.30 Trigger circuit efficiency (defined in the text) as a function of the run number for the single muon (MB $\otimes$ 1D) and dimuon (MB $\otimes$ 1D1S) triggers.

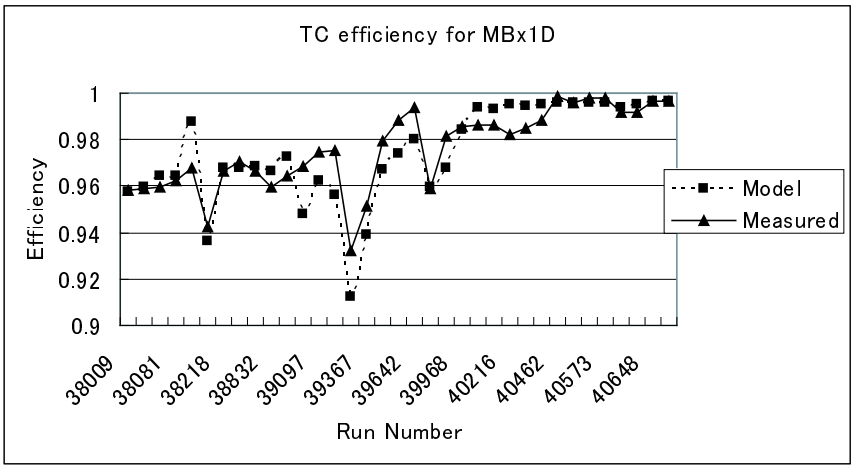

Figure 2.31 Trigger circuit efficiency (defined in the text) as a function of the run number for the single muon trigger, with that determined by a simple model calculation.

addition, status of such as low-voltage, electronics, and gas flows was monitored, which was rather stable.

High Voltage

Status of all HV chains was monitored attentively, which were the most delicate component of a detector. Both the MuTr and MuID suffered from trip HV chains. They were sometimes due to high current caused by unstable beam condition, but usually due to spark current caused by humidity or other reasons. Flowing gas (air or nitrogen) into the secondary volumes of the detectors (just outside of the ionization gas volume) significantly reduced the number of trip chains for both the detectors. Trip chains were automatically recovered by a script monitoring and recording the status of all chains in every 10 (MuTr) or 60 (MuID) seconds. Because of shorter recovery time (1 minute) compared to the typical run scale (1 hour) and small trip frequency ($\ll$ 1 trip per channel per run) for most of the channels, its effect on the variation of J/ψ detection efficiency is minimal, which is confirmed in the next section. Most of the above problems had been repaired after run-II data-taking. During the run-III data-taking period, it was very stable but the staus of course had been monitored extensively and the same procedure as used in run-II data analysis has been used for the run-III analysis.

Data quality

For both the MuTr and MuID, hit occupancies in each chamber plane were inspected for dead electronics, dead HV chains, and hot channels. For the MuTr, distributions of relative ADC counts of samples were monitored as shown in Fig. 2.32 and Fig. 2.34, to ensure the proper timing of the readout (peaks in the third sample). For the MuID, TC efficiency, described in section 2.7, was checked to make sure the NIM-logic trigger was working properly. Also BBC which was used as the normalization counter was extensively monitored. One of the BBC online monitoring in Fig. 2.33 shows a good timing and raw vertex position. No significant deviation of these quantities from criteria was observed throughout the p+p and d+Au run.

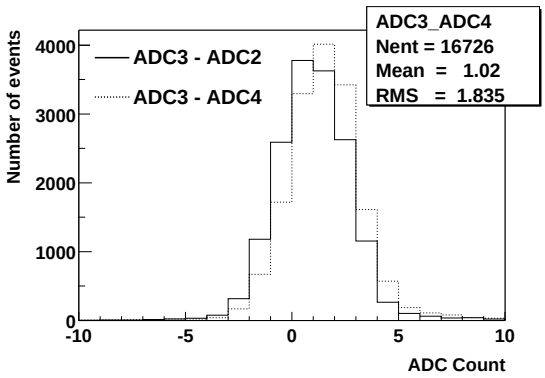

Figure 2.32 Distributions of relative ADC counts, (ADC3 − ADC2) and (ADC3 − ADC4), which were monitored online to confirm their average values were positive.

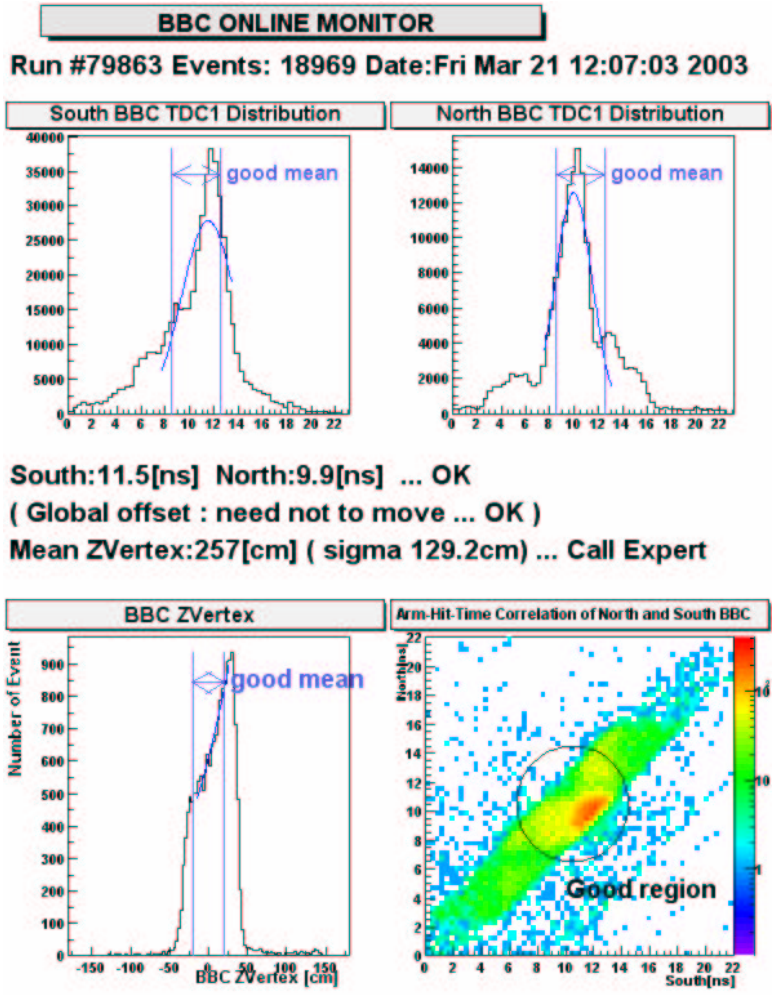

Figure 2.33 BBC online monitoring plot which shows the timing distribution(top) and reconstructed vertex distribution(bottom).

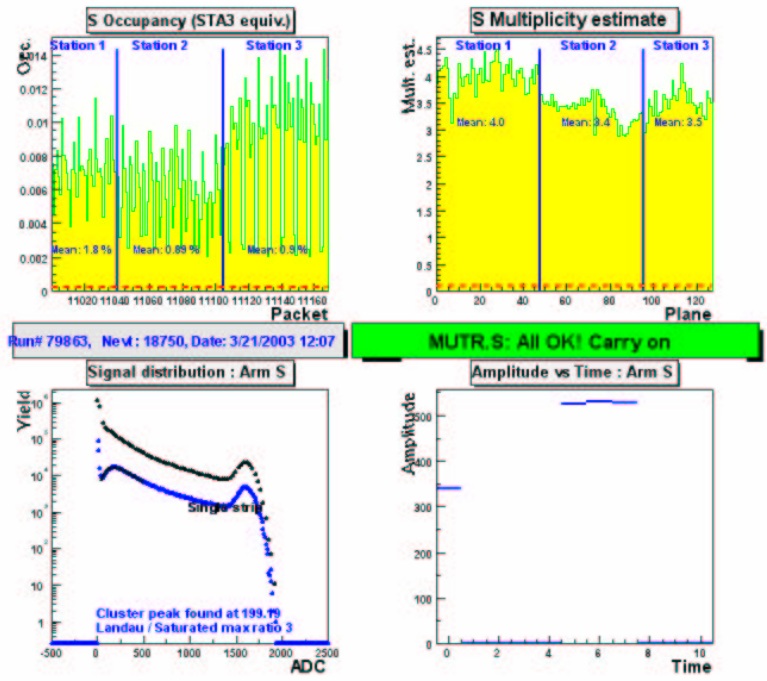

Figure 2.34 MuTr online monitoring plot which shows hit occupancy(top left), multiplicity(top right), signal distribution of the clusters(bottom left) and ADC counts for each sampling(bottom right)

Chapter 3

Data analysis

In this section, the branching fraction for the decay $J/\psi \to \mu^+\mu^-$ ($B_{\mu\mu}$) times rapidity-differential cross section for inclusive J/ψ production in the Muon Arm acceptance $B_{\mu\mu}d\sigma_{J/\psi}/dy|_{y^i}$ is obtained.

The cross-section for J/Ψ production is simple (in principle) to calculate:

$$\sigma(pp \to J/\Psi) = N_{J/\Psi}/\mathcal{L} \tag{3.1}$$

Of course, in practice, it is significantly more difficult to extract a correct cross-section than one might guess from this simple formula since $N_{J/\Psi}$ is not the number of J/Ψ that we observe, but rather the number that were actually created — and there are a number of significant correction factors that need to be applied to extract this quantity. The luminosity is also significantly more difficult to accurately compute than is suggested by that one symbol, $\mathcal{L}$.

The equation for $\sigma_{tot}(pp \to J/\Psi \to \mu^+\mu^-)$ (with the correction factors in the chosen factorization) is given by:

$$\sigma^{tot}_{J/\Psi} = \frac{N^{4\pi}_{J/\Psi}}{A\varepsilon^{4\pi}_{\mu}B_{\mu\mu}\varepsilon^{J/\Psi}_{MB}} \Big/ \frac{N_{MB}}{\sigma^{pp}_{tot}\varepsilon_{MB}} \tag{3.2}$$

where

- $N^{4\pi}_{J/\Psi}$ = the number of J/Ψs reconstructed in the muon arm that pass our given cuts.

- $A\varepsilon_{\mu}^{4\pi}$ = the product of the detector acceptance times reconstruction efficiency for J/Psis thrown over 4π. For this particular calculation each event was also required to pass the simulated di-muon trigger that was used for Run III.
- $B_{\mu\mu}$ = the branching ratio for J/Ψs decaying to two muons
- $\varepsilon_{MB}^{J/\Psi}$ = the BBC trigger efficiency for J/Ψ events produced within 38 cm of z=0
- N_{MB} = the number of minimum bias events used for this analysis, that have an event vertex within 38 cm of z=0
- σ_{tot}^{pp} = the p-p total cross section at $\sqrt{s} = 200$ GeV
- ε_{MB} = the BBC trigger efficiency for minimum bias events that have a vertex within 38 cm of z=0

The equation for this differential cross-section (with the correction factors in the chosen factorization) is given by:

$$\frac{d\sigma_{J/\Psi}}{dy}|_{y^i} = \frac{1}{\Delta y^i} \frac{N_{J/\Psi}^{y^i}}{A\varepsilon_{\mu}^{y^i} B_{\mu\mu} \varepsilon_{MB}^{J/\Psi}} / \frac{N_{MB}}{\sigma_{tot}^{pp} \varepsilon_{MB}} \tag{3.3}$$

where the efficiency is now calculated for the particular bin of interest as are the number of counts, $N_{J/\Psi}^{y^i}$.

We also present a normalized $p_\perp$ spectrum integrated over one-unit rapidity coverage of the each Muon arm acceptance because of the limited statistics:

$$\frac{1}{2\pi p_\perp} \frac{d\sigma_{J/\Psi}}{dy dp_\perp}|_{y^i, p_\perp^i} = \frac{1}{2\pi p_\perp \Delta p_\perp^i} \frac{N_{J/\Psi}^{y^i, p_\perp^i}}{A\varepsilon_{\mu}^{y^i, p_\perp^i} B_{\mu\mu} \varepsilon_{MB}^{J/\Psi}} / \frac{N_{MB}}{\sigma_{tot}^{pp} \varepsilon_{MB}} \tag{3.4}$$

J/ψ particles are identified in an invariant mass spectrum of $\mu^+\mu^-$ pairs, where the number of J/ψ's, $N_{J/\psi}$, is counted with a reasonable background subtraction. The detection efficiency for the $J/\psi \to \mu^+\mu^-$ events, $\varepsilon_{tot}^{J/\psi}$, is determined with a simulation, where detector response is well tuned to the

real data. An integrated luminosity, $\mathcal{L}$, is estimated also with a simulation, where consistency with the real data is confirmed. Details of analysis procedures to obtain $N_{J/\psi}$, $\varepsilon_{tot}^{J/\psi}$ and $\mathcal{L}$ are described in the following.

3.1 Data Set and Running Conditions

3.1.1 Run III Data Set

Online Event Selection — Events were selected by the coincidence of a valid minimum bias (BBCLL1) trigger and a valid MUID Blue Logic (dimuon) Trigger (BLT) which is described in section 3.1.5 Almost all events which passed the dimuon trigger for selected runs were filtered out of the full data set and written to separate PRDF files. More info is given in filtering section 3.2.7.

3.1.2 State of Muon Tracker

During Run III both the south and north muon tracker arms were installed and taking data. There were some high voltage channels in the tracking chambers which were disabled because of high current draw, a handful of data packets with intermittent problems, and a few packets which were found to have bad data (duplicated channels) in them. For the selected runs, all packets were in, and basically the same HV channels were off, i.e. we have a fairly stable situation throughout the analyzed data. We attempted to account for the problems in the Monte Carlo and real data analysis.

3.1.3 State of Muon Tracking Alignment

The alignment of the three tracking stations relative to each other was determined by looking at straight tracks from field-off data that were taken during Run III. Once the relative alignment was determined, correction constants were produced to be used for both the Monte Carlo detector response and the reconstruction of both Monte Carlo and real data.

The alignment procedure was basically the same as for the Run II analysis. The expected phi alignment accuracy is approximately 100 μm. The remaining misalignment errors contribute little to the J/ψ mass resolution.

3.1.4 State of Muon Identification

In general, the status of the MuID HV was good during Run-III. However, there were some bad chains where HV could not be applied at all or we could apply only lower voltage (less than 4300V) due to some problems. Also, there were issues with beam-related background, specially in the beginning of stores, which caused high current draws. Therefore, the MuID HV was left off until beam conditions were stable. (For Run IV, shielding is being installed to alleviate this problem). During the later part of the dAu run, there were some issues regarding the BLT crate (a bad LV module that was later replaced) that caused a drop in the so-called Trigger Circuit Efficiency (TCE) in the North arm. Furthermore, for the p-p running, the noise in the South MUID became worse, and forced running with higher thresholds (120 instead of 90, mV), leading to a reduced efficiency.

The general procedure of how the MuID efficiencies were estimated, as for Run III, using roads reconstructed for minimum bias events is summarized in section 3.3.2. In addition to this procedure, alternative methods were also used for independent estimates/cross-checks, including using reconstructed tracks from the MuTR in the new framework, with momentum and depth cuts, comparing projections and hits in the MuID. Since more severe cuts are applied than was used in the trigger, this method can be used on triggered data, which is very beneficial in terms of statistics. These corrections are large contributors to the overall efficiency corrections and systematic errors, and are described in detail in section 3.3.2.

3.1.5 Dimuon Trigger

The so-called MuID Blue-Logic Trigger was used for Run-III. The trigger scheme and its performance are summarized in section 2.7. For the selected runs in Run-III, the last gap was not used in the trigger, due to the large beam background mentioned earlier. Therefore, the so-called Deep trigger

was more of a shallow Deep trigger, sometimes referred to as Sheep and going to the fourth gap. The shallow trigger was going to the second gap. For the later third of the collected d-Au luminosity, we filtered on the 2-Deep trigger, while for the earlier parts of the d-Au run, and for the p-p run, the dimuon trigger was 1D1S.

The trigger circuit efficiency from the pp dimuon trigger for the runs we analyzed is shown in figures 3.1 and 3.2. The red line indicates 95% efficiency.

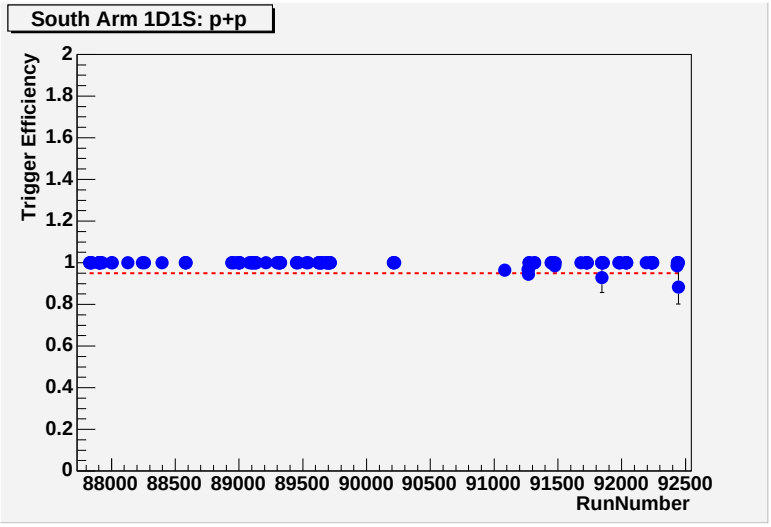

Figure 3.1 Trigger Circuit Efficiency for South dimuon trigger in p + p

3.1.6 Selection of Good Runs

In order to minimize the systematic error due to varying Muon Tracking HV, Muon Identification HV and Muon Tracking electronics problems, only those runs that passed the cuts shown in table 3.1 were selected for the analysis. A further elimination of runs was made based on examination of the hit distributions and occupancies from online monitoring and the PHENIX logbook.

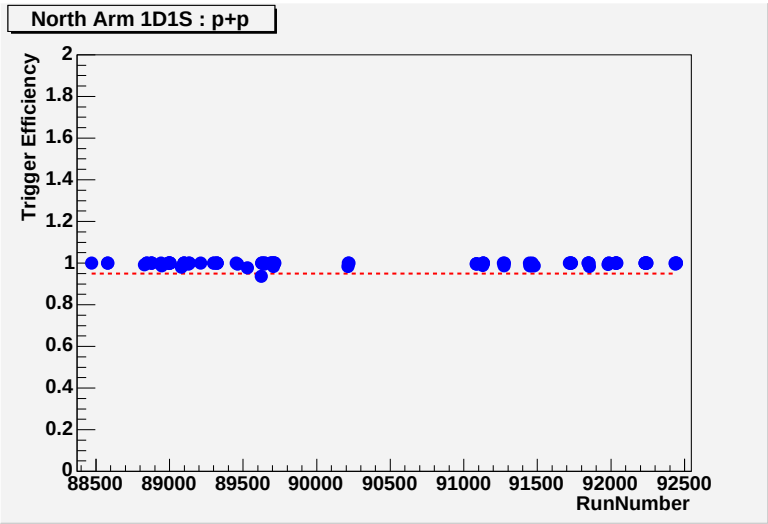

Figure 3.2 Trigger Circuit Efficiency for North dimuon trigger in p + p

In run 3, the Muon Tracking HV performed well and effects from the few bad HV channels are small. Also most runs that did have a problem are ones that already had problems with Muon Identification HV. Next runs which have a large number of bad Muon Identifier HV channels have been eliminated according to the cuts which are listed in table 3.1.

Because the efficiency loss from these bad Muon Identifier HV runs was found to be quite large, a calculation of the effect of the bad HV on the overall efficiency has been done for each run, and runs with more than 20% loss have been thrown out. Finally some runs had high occupancy and high multiplicity in some MuTR packets and were excluded from the analysis. This problem was caused by unstable low voltage distribution cards.

3.2 Muon Software

The Monte Carlo codes described below were needed to calculate $A \times \varepsilon^{4\pi}_{J/\psi}$ for J/ψ's falling in the rapidity and $p_\perp$ bins of interest to our calculations. The reconstruction code that was used was common to Monte Carlo and

Run	MuTR HV	Mutr Electronics	MuID HV
dAu(south)	9(3) out of 160	2 octants missing(0)	40(32) out of 300
dAu(north)	20(11) out of 160	2 octants missing(0)	35(25) out of 300
pp(south)	9(3) out of 160	2 octants missing(0)	35(33) out of 300
pp(north)	20(11) out of 160	2 octants missing(0)	31(25) out of 300

Table 3.1 Summary table of the maximum number of disabled MuTR and MuID HV chains allowed, and the maximum loss of the MuTR packets allowed. (X) is the nominal number of disabled chains (missing packets) for normal runs.

Beams	Arm	Nominal (nb^{-1})	Filtered (nb^{-1})	MuID HV (nb^{-1})	MuTr HV (nb^{-1})	TCE (nb^{-1})	MuTr FEE (nb^{-1})	Final (nb^{-1})
dAu	S	2.74	2.36	1.99	2.33		2.29	1.63
dAu	N	2.74	2.46	2.31	2.43		2.36	1.86
pp	S	352	259	234	245	240	228	208
pp	N	352	233	199	219	195	223	184

Table 3.2 Summary of integrated luminosity (nb^{-1}) for final good runs and breakdown of losses for different problems.

real data analysis. We attempt to describe the level of detail included in these codes and show how well we believe they represent our real detector performance.

We used PISA2000, the PHENIX detector simulation package, with the 3D magnetic field map, July 11 (2003) version, to track the muons through the active detector volume. In PYTHIA, events were thrown at $z_{vtx} = 0$. We used PISA to simulate a Gaussian z_{vtx} distribution with $\sigma = 39$ cm and only used events within 38 cm of z=0 to calculate efficiencies.

The flow chart of muon reconstruction and response software is shown at Fig.3.3

3.2.1 Muon Tracker Detector Response

The muon tracker detector response was simulated with the following:

- The real detector geometry was used including final alignment corrections.

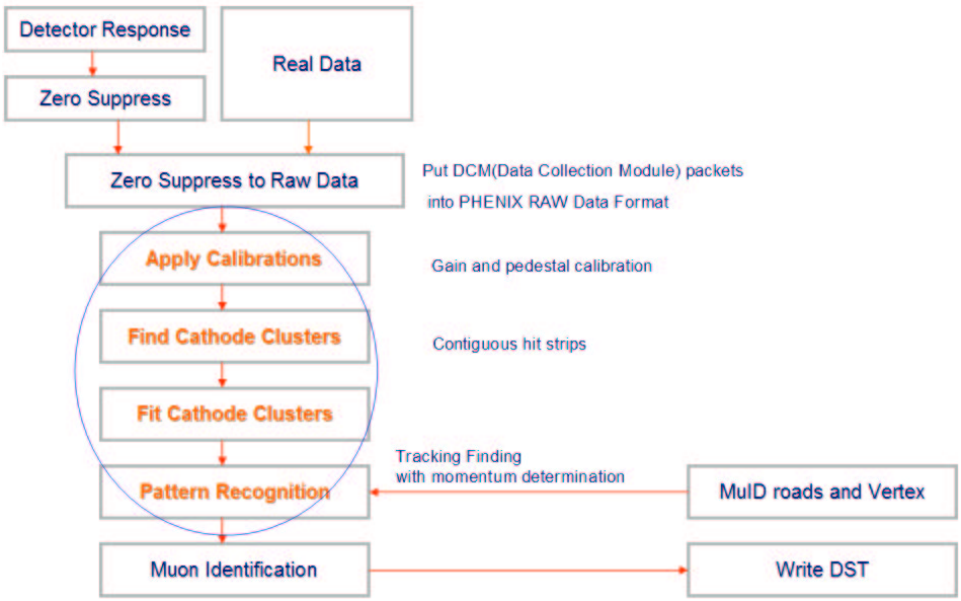

Figure 3.3 Muon arm reconstruction and response flow chart

- The configuration of tripped high voltage (HV) channels in the MuTr was simulated.
- DCM channels that were determined to contain bad/unreliable data were disabled in the simulated data as well as the real data analysis.
- Gains and pedestals determined from real data were used to set charge spectra and noise levels for each readout channel. If zero or minimal gain was measured from real data, the channel was effectively disabled for both MC simulations and real data analysis.
- Cathode strips in the station 2 North chambers which were determined to be scratched within the active volume were given reduced charge values, as was seen in real data.
- For the charge deposition in a tracker chamber, the Landau scale = 15.0 and the offset = 30.0 which makes the landau distributions from Monte Carlo approximately match the landau distributions from real data.
- The value for tracker chamber efficiency was 99%

Fig 3.5 and 3.4 show radiographs of the various muon tracker chamber gaps as produced by Monte Carlo and real data for one of pp runs. The radiographs were produced by finding all intersections of cathode strip hits within a given gap when there was one and only one hit on each plane within a gap. The latter cut was used to try to eliminate ghost hits caused by non-correlated cathode plane hits. As can be seen in the figures, on a gross level, the dead and live areas in the chambers are well matched between the two data sets.

3.2.2 Event Reconstruction

For run 3 data taking we found that a number of cathode strips in Station 2 North chambers were apparently scratched in the active volume of the chamber. This resulted in reduced charge collection on these strips. We attempted to determine all such strips using real data and tagged the affected

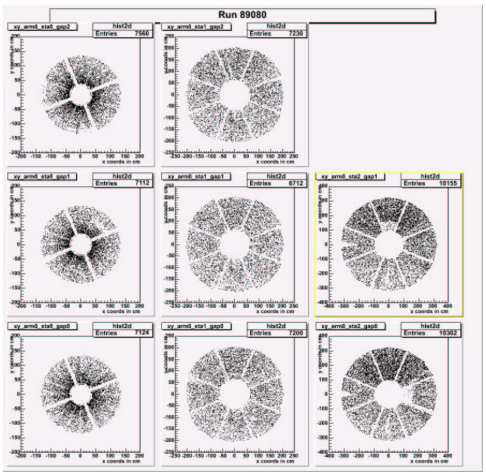

Figure 3.4 Real data-produced radiographs of each gap of the muon tracker for one of pp runs. The three gaps of station 1 are shown in the left three plots, the three gaps of station 2 are shown in the middle, and the two gaps of station 3 are shown in the right two plots.

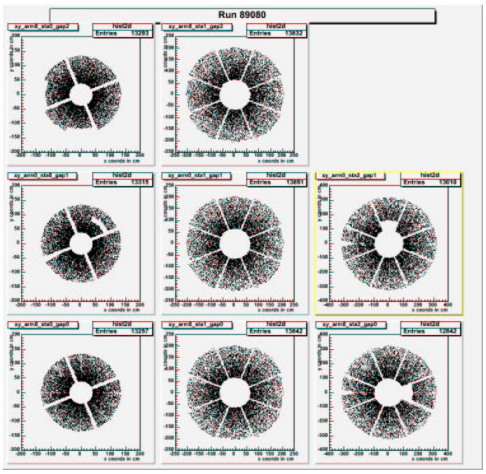

Figure 3.5 Monte Carlo-produced radiographs of each gap of the muon tracker. The chamber gaps are arranged in the same order as figure 3.4

strips in the database. Then in the reconstruction code all of these strips were given a large RMS value when fitting clusters and determining the resolution of fitted clusters. This should result in more accurate chi-square values and slightly improved cluster fitting results in some cases, but we don't expect too much improvement in the final mass resolution because of the lost charge information.

The old framework software reconstruction was run in the default mode which uses found muon identifier roads to seed the track finding in the track finder. By default only "golden" roads in the muon identifier are passed to the tracker to find associated tracks (see explanation of golden roads in section 3.2.5). After the tracker pattern recognition is completed, all found tracks are fit using a Kalman Filter fit package from GEANE. All muon tracker measurements as well as the measured vertex point and the muon identifier measurements are used in the fit. Following this fit a second-pass road finder module is executed which attempts to flag ghost tracks by setting the ghostflag to 1.

MuID road finding

First, one-dimensional roads are searched using either horizontal or vertical tubes. A road seed is constructed from a hit tube in the seed gap (or the first gap in the "search order") and event vertex position measured with the BBC or other interaction trigger counters. It is then extrapolated to the next gap in the search order, where additional hits are searched which are consistent with the road trajectory. The hit closest to the projection of the road to the gap within the search window is generally accepted and attached to the road. The road is fitted including the new hit and extrapolated to the next gap. The size of the search window is set to 15 cm (about two-tube widths) to allow a deviation from a straight-line trajectory due to multiple scattering in the steel absorbers. Two search orders, $2\rightarrow1\rightarrow3\rightarrow4\rightarrow5$ and $3\rightarrow2\rightarrow1\rightarrow4\rightarrow5$ where each number n stands for the n-th gap of the MuID, are used to enable roads to be reconstructed even the seed gap has inefficient tubes. Generally shallower gaps come earlier because of smaller multiple scattering, except for the first gap because of its higher hit occupancy from hadron and soft-electron background than the second or third gap. The

algorithm is allowed to skip gaps without hits, in order to keep higher efficiency despite low-efficiency tubes in one or two gaps. Finally both horizontal and vertical roads are combined and final two-dimensional roads are reconstructed. Typical road-multiplicity is small (< 0.01) for minimum-bias events.

Road finding efficiency is expected to be over 99% for muons with a momentum $p > 3$ GeV/c with good chamber efficiencies (97%) and low hit occupancies as in p+p collisions.

MuTr cluster finding / fitting

When a charged particle passes through a MuTr gap which is composed of two cathode planes and one anode-wire plane, charges are usually induced in two or three consecutive cathode-strips in each cathode plane. The hit position of the particle in each cathode plane is reconstructed with the following method.

The amount of the peak charge in each cathode strip is determined by four ADC samples as described in section 2.5.1. A sequence of consecutive hit strips, called a cluster, is searched and fitted with an empirical formula (Mathieson function [136]) to find the one-dimensional position at which a particle would have passed in each cathode plane. Figure 3.6 shows an example of peak charge distribution for a cluster. The cluster position is obtained as the peak position of the fit function.

If relative gain fluctuation and noise level are 1% of a typical signal pulse or less, position resolution of 100 μm is obtained, which is confirmed with the cosmic ray test described in section 2.5.1. With this resolution, about 110 MeV/c^2 is expected as the mass resolution for a J/ψ. However the actual noise level has turned out to be worse during the run at station 2, which was typically 3%. Degradation in J/ψ mass resolution due to higher noise level is expected to be about 30% (140 MeV/c^2), which is compared with the real data in later section.

Muon track finding / fitting

Starting from a road found in the MuID, a track grows by attaching clusters in the MuTr stations from backward to forward, that is, station 3 to

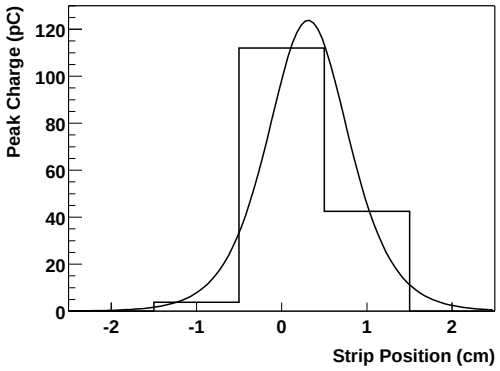

Figure 3.6 An example of peak charge values of sequential cathode-strips (a cluster) induced by a charged track, together with a fit of the Mathieson function. In this example, the cluster has three hit strips and its position is determined to be 3.1-mm off the position of the central strip.

station 1.

Each road is extended to each cathode plane in station 3, where clusters are found consistent with the road inside its search window. Table 3.3 shows widths of the search windows for both the θ and ϕ directions at each station in the South MuTr. The search window in station 3 is large enough compared to position resolution of roads (10 to 20 cm depending on quality cuts on them). It gets smaller from station 3 to station 1 because track information such as position and momentum is getting more accurate in the process of track finding. By fitting clusters, a local vector called a stub is found. A stub requires at least two cathode planes with a cluster in each station. A crudely estimated momentum is assigned to the track from the last penetration gap of the MuID road.

The track is then extrapolated to station 2, using an effective bend-plane and a momentum kick, which are determined by the approximate momentum and the magnetic field inside the Muon Magnet. Clusters are searched again in station 2 within the search window. If a stub is found in station 2, the stubs in station 2 and 3 are fitted altogether to assign more accurate momentum to the track. It is again extrapolated to station 1 using

station	θ direction (cm)	ϕ direction (cm)
1	20	10
2	30	25
3	50	40

Table 3.3 Widths of the search windows for the θ and ϕ directions at each MuTr station.

better momentum information, where clusters are searched and attached to the track once more. The minimum number of hit planes required for a track is 12 out of all 16 planes.

Finally all the cluster positions and the event vertex position are fitted with the Kalman-Filter algorithm [137], which is a recursive technique to obtain the solution to a least-squares fit, to determine the momentum vector of the track at the event vertex taking energy loss in the absorber (the Central Magnet and copper nosecone) into account.

Position resolution of the BBC, expected to be about 2 cm with a simulation, is confirmed with the real data. Figure 3.7 shows distribution of the differences between z-vertices found with the BBC and the Pad Chambers (PC) in the Central Arms [126]. The distribution is fitted with a double Gaussian function. The larger Gaussian has a 2.7 cm width, while the smaller one has a 9.8 cm width which is supposedly due to background contribution. Resolution of the PC is expected to be also about 2 cm with a simulation, which is consistent with the real data with background subtracted.

3.2.3 Single muons

In this section, some properties of reconstructed muons are shown to demonstrate their qualities and Muon Arm performance.

Event vertex distribution

Low-momentum ($p < 5$ GeV/c) single muons, the majority of the inclusive muon yield, are expected to be dominated by charged hadrons decay-

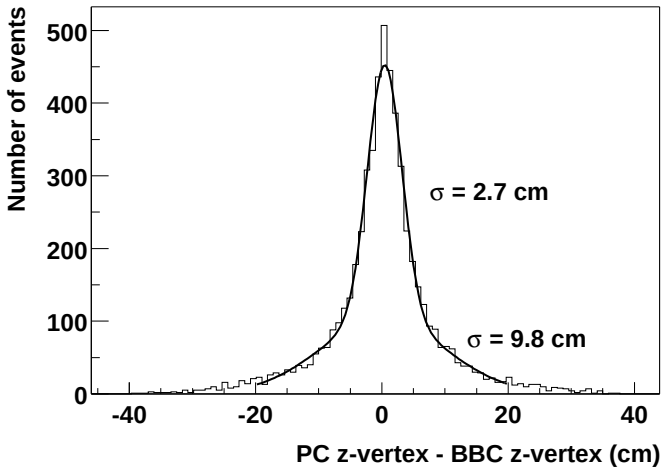

Figure 3.7 Distribution of the differences between z-vertices found with the BBC and the Pad Chambers (PC) in the Central Arms. The distribution is fitted with a double Gaussian function. The larger Gaussian has a 2.7 cm width, while the smaller one has a 9.8 cm width which is supposedly due to background contribution.

ing weakly into muons ($\pi^{\pm} \to \mu^{\pm}\nu$ and $K^{\pm} \to \mu^{\pm}\nu$) in flight before the nosecone. Contribution of punch-through hadrons is small, which has been confirmed by the beam test described in section 2.5.2. The decay probability for charged pions $P(\pi \to \mu)$ is given by

$$P(\pi \to \mu) = 1 - \exp(-LB_r/\gamma c\tau) \simeq LB_r/\gamma c\tau$$

where L is the distance between the vertex point and nosecone including one hadronic interaction length of the nosecone (15 cm), B_r is the branching fraction for the decay $\pi^{\pm} \to \mu^{\pm}\nu$, γ is the ratio of the particle energy to mass and $c\tau$ is the decay length of the particle. Typical value of $LB_r/\gamma c\tau$ is $3{\times}10^{-3}$ for $p \sim 3$ GeV/c muons. The same kind of formula holds also for charged kaons. The net contribution of charged kaons to single muon spectra is expected to be about the same as that of charged pions.

Figure 3.8 shows BBC z-vertex (z_{vtx}) distribution for single-muon events divided by that for minimum-bias events in the range $|z_{vtx}| < 38$ cm which is a cut used for the J/ψ analysis. Error bars indicate statistical errors of the particular run. The solid line shows a straight line fit to the data assuming flat distribution for non-decay components, which reproduces the data very well in the range $-20 < z_{vtx} < 38$ cm. The deviation from the fit in the range $-38 < z_{vtx} < -20$ cm is due to the increase in background induced by very low angle particles. From the fit, the fraction of non-decay components is determined to be about 20%, which supposedly includes background such as punch-through hadrons and ghost tracks as well as physics signals such as charm and bottom mesons decaying semi-leptonically.

The dominance of decay muons to the measured single-muon yield is consistent with an expectation, which confirms that the South Muon Arm has been worked as expected and there is no significant contribution of ghost tracks nor punch-through hadron background to reconstructed muons.

Track-road matching

Figure 3.9 shows distribution of the distance between intersections to a station-3 plane of a track and a corresponding road, $r_{track-road}$. The peak is around 10 cm which is consistent with the expectation from the position resolution of a road (8.4 cm) and multiple scattering in the absorbers, thus demonstrating that the two detectors match well as expected.

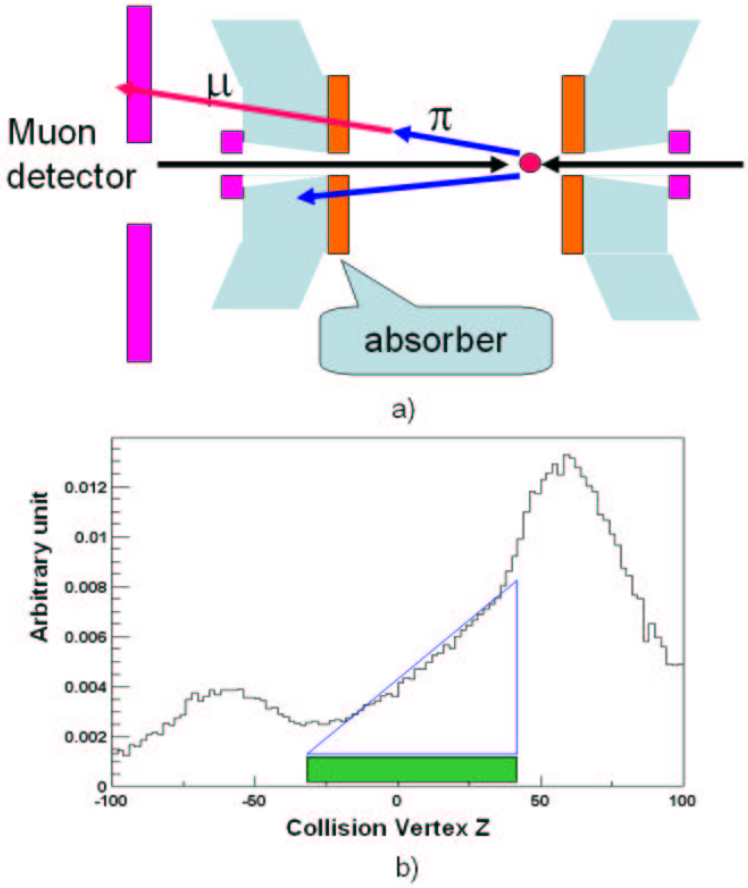

Figure 3.8 BBC z-vertex distribution for single-muon events divided by that for minimum bias events. The solid line shows a linear fit to the data points assuming constant distribution for non-decay components.

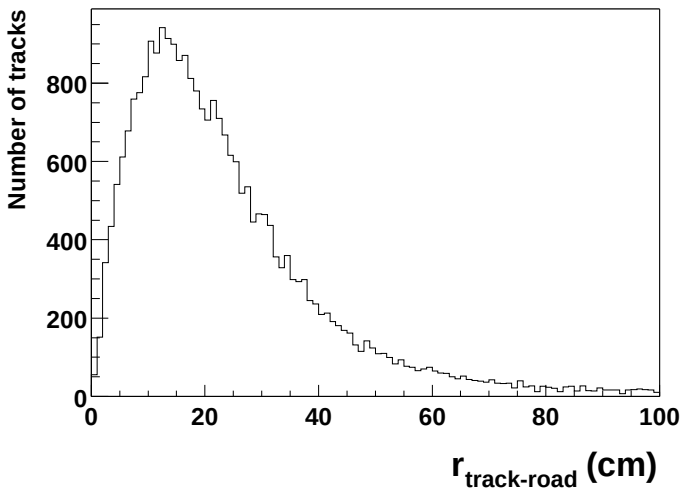

Figure 3.9 The distribution of the distance between a track and a road ($r_{track-road}$) at station 3. The peak position, around 12 cm, roughly represents the rms in the two-dimensional space.

3.2.4 Muon Tracking Software Performance

The state of the Muon Tracker during data taking was modeled in the Monte Carlo as outlined in section 3.2.1. To check that the Monte Carlo representation accurately reflected the true state of the detector, the hit distributions in all planes were compared between Monte Carlo and real data, and the track reconstruction efficiency, as determined by pointing MuID roads to the muon tracker was compared between real data and Monte Carlo.

3.2.5 Muon Identification Software Performance

Some MUID software specifics are discussed in section 3.3.2, while describing how the MUID tube and trigger efficiencies were estimated from real data, using MC data for cross-checks. The main part of MUID offline software of interest is the road-finding. The material in this section is included for completeness and to help the reader understand the later sections. The MUID readout is on a digital yes/no basis; if the signal on a tube is above a set threshold, the tube is said to have fired. This reduces the problem of hit- and cluster-finding to investigating which tubes have fired, and if they are neighbors. A tube is oriented in either the horizontal or vertical direction.

The offline roadfinder in use starts out by doing 1Dim-road reconstruction. This means looking at combinations between fired tubes in the MUID planes/gaps in one orientation at a time, and keeping combinations that roughly point back to the nominal vertex position. Different search orders are used to remove possible biases. The basic requirements are that there needs to be at least one hit in one of the first two planes (0 or 1), and that the road should make it at least to plane 2. There is also a requirement that there should be at least 3 hits per 1Dim road, which for the shallower road (depth = 2) means that all planes need to be hit. This is sometimes referred to as the original parameter setting. In a reconstruction pass, this hit requirement was changed to allow for one skipped/missed plane. This is referred to as the relaxed parameter setting.

After the 1Dim roadfinding is done, the results from the two orientations are combined, into 2Dim roads. The depth, and the number of hits, between

the 1Dim roads resulting in a 2Dim road need to match within ± 1. In the roadfinder, there is also grouping of nearby candidate roads, and selection of so-called golden roads, but this distinction is not relied on in the offline data analysis, so we will not go into these details here.

It is to be noted that in this procedure, the reconstructed tracks have to reach the third MUID gap, while the 1D1S trigger was requesting one track to the second, and one to the fourth. As it was first seen with the new framework reconstruction (MUTOO, MUIOO) then with a modified MUI road finding, there are some J/ψ's to be gained considering these shallower roads. However, because of a higher background and a lack of time to shrink it, we restrict ourselves for now to this third gap roads, the loss being taken cared of by the acceptance$\times$efficiency correction.

3.2.6 Muon Identification Trigger Simulation

To monitor the Blue-Logic Trigger online, a software Blue-logic Trigger emulator was written. It simulates the logic of hardware Blue-Logic trigger circuit and calculates trigger decisions according to Muon Identifier raw hit information we recorded online. During Run 3, we ran this emulator simultaneously with data taking and used it as a tool to diagnose Blue-Logic trigger hardware. To quantify how well the hardware works, we defined Trigger Circuit efficiency as the percentage of the times when hardware fires a trigger to the times when emulator fires a trigger. For most of the data we took, this efficiency is about 90% (again, for the p-p period, see figures 3.1 and 3.2). During offline analysis, we also use it as one of criteria for run selection.

The validity of the trigger emulator was intensively checked, already for Run-2 (see section 2.7) for many runs. The trigger emulator, using estimated MUID tube efficiencies, was an integral part of the simulation chain.

3.2.7 Filtering

For this analysis we use level-1 trigger filtered events for either two-deep (2D) road triggers or one-deep and one-shallow (1D1S) road triggers. For

the d-Au data runs 78402-80312 we use 2D triggers, while for the earlier d-Au runs, 72336-78307, we use 1D1S triggers. For p-p runs we use only 1D1S triggers. Triggers were filtered out on the RCF machines using HPSS to extract the prdf files and the standard OnCal filtering routines to select the triggered events via the live bits with TriggerHelper. These events were then written out to separate filtered PRDF files and stored in HPSS.

3.2.8 Data Production and Analysis

We built up standard dsts and MWG nanodsts from the prdfs, including the following subsystems : BBC, ZDC, FCAL, MUTR and MUID, and using the new 3D simulated field map (including the north field). Several processing passes were done to test various improvements of the reconstruction. The data we show here were processed at CCF using the pro.43 libraries. To cope for a few percents loss of segments at various stages of the analysis we correct our result by using the ratio of the event number in nanodst and run control number of triggered events(see table 3.4).

Sample	In RC	In MWG	MWG/RC	BBC live	$\|z_{vtx}\| < 38$	N_{MB}
S2D	2 412 354	2 217 582	91.93%	1 335 801 768	$\sim$ 96.4%	1.184×10^9
S1D1S	31 820 276	27 886 566	87.64%	1 875 636 515	$\sim$ 94.5%	1.566×10^9
N2D	1 061 717	1 022 462	96.30%	1 701 932 446	$\sim$ 95.2%	1.553×10^9
N1D1S	3 051 636	2 847 592	93.31%	1 971 994 519	$\sim$ 94.7%	1.711×10^9
SPP	1 164 526	1 164 244	99.98%	4 639 768 393	$\sim$ 97.7%	4.531×10^9
NPP	4 062 648	4 057 461	99.87%	4 108 647 407	$\sim$ 98.0%	4.021×10^9

Table 3.4 Number of processed triggers found in the run control and in the nanodst. The number of corresponding minimum bias events N_{MB} is equal to the number of lived BBC triggers $\times$ the MWG/RC ratio $\times$ the fraction of these events passing our $|z_{vtx}| < 38$ vertex cut estimated on scaled recorded BBC triggers. This numbers were computed on a run by run basis and sum up to the number in the last column.

3.2.9 Analysis cuts

Several analysis cuts are made on the final ntuples in order to reduce the number of ghost tracks and to improve the signal to noise for the J/ψ mass

peak by reducing the background levels:

- Muon pairs with tracks flagged as ghosts by the second pass roadfinder (ghostflag = 1) are removed.
- The vertex is required to be within 38 cm of z=0, $|z_{BBC}| < 38$ cm. To deal with the acceptance loss caused by this cut, we compute the fraction of scaled bbc triggers within our vertex range and include the drop in the luminosity normalization (see table 3.4).
- Pairs with one or two tracks with a poor Chi-square are removed, $\chi^2/DOF < 20$.
- Both tracks are required to have positive momentum (North arm, positive rapidity) or negative momentum (South arm, negative rapidity).
- J/ψ rapidity has to be within -2.2 to -1.2 for the south arm and $+1.2$ to $+2.4$ for the north arm.
- The difference between the dimuon reconstructed vertex and BBC vertex is required to be less than 25 cm ($|z_{BP} - z_{BBC}| < 25$ cm).
- The two roads have to come from different quadrants.

Except for the vertex cut which is taken cared of in the luminosity computation, all these cuts are applied to the montecarlo reconstruction when we compute the acceptance correction.

3.3 J/ψ detection efficiency

Total detection efficiency for $J/\psi \to \mu^+\mu^-$ events in the collisions, $\varepsilon_{tot}^{J/\psi}$, is decomposed into four factors:

$$\varepsilon_{tot}^{J/\psi} = \eta_{acc} \cdot \varepsilon_{MuID}^{J/\psi} \cdot \varepsilon_{MuTr}^{J/\psi} \cdot \varepsilon_{BBC}^{J/\psi} \tag{3.5}$$

where

η_{acc}: South Muon Arm acceptance times reconstruction efficiency for muon pairs from J/ψ's produced in $1.2 < y < 2.2$ with 100% chamber efficiencies,

$\varepsilon^{J/\psi}_{MuID}$: Efficiency correction due to real chamber efficiencies of the MuID,

$\varepsilon^{J/\psi}_{MuTr}$: Efficiency correction due to real chamber efficiencies of the MuTr, and

$\varepsilon^{J/\psi}_{BBC}$: Efficiency of BBC for p+p $\rightarrow J/\psi X$ ($1.2 < y^{J/\psi} < 2.2$) events.

Analysis procedures and results of each factor will be described in the following.

3.3.1 Detector acceptance

The geometrical acceptance of the South Muon Arm is represented as η_{acc} including reconstruction efficiency for muon pairs from J/ψ's produced in $1.2 < y < 2.2$ with 100% chamber efficiencies. In p+p events, multiplicity is sufficiently small to achieve high (~90%) reconstruction efficiency when hits are found in chambers. Therefore, η_{acc} is close to the geometrical acceptance itself. Using simulation, η_{acc} is calculated as

$$\eta_{acc} = \frac{\text{the number of reconstructed } J/\psi \text{ events with } 1.2 < y < 2.2}{\text{the number of simulated } J/\psi \text{ events with } 1.2 < y < 2.2}$$

where PYTHIA has been used to produce J/ψ events, based on the color-singlet model. Rapidity and p_T distributions (at lower p_T) of J/ψ do not depend on the production model unlike a total cross section, and are consistent with the real data as discussed in section 4. The same reconstruction software, parameters and cuts are used as the real data. The result of the average value of η_{acc} is 0.11 requiring a dimuon trigger. Rapidity and p_T dependence will be described in later section including finite chamber and BBC efficiencies ($\varepsilon^{J/\psi}_{tot}$).

Polarization of J/ψ or spin-alignment (denoted as λ), which is sensitive to its production mechanism, is unknown at $\sqrt{s} = 200$ GeV and not possible to be determined with the limited number of J/ψ's obtained in Run-2.

The South Muon Arm acceptance has significant λ dependence as shown in Fig. 3.10, giving a systematic uncertainty of η_{acc}. This dependence is primarily a result of the $p_z < 2\,\mathrm{GeV}/c$ lower-momentum cutoff which cuts off the backward-going daughter muons in the J/ψ rest-frame with respect to the momentum direction of the J/ψ in the laboratory frame. Results of both lower-energy experiments and Tevatron indicate that $|\lambda|$ is no larger than 0.3 especially for low-p_T ($\sim$ 1 GeV/c) and low-x_F ($\sim$ 0.1) J/ψ's [120, 124] which dominate our yield. On the assumption of $|\lambda| < 0.3$, we have assigned a 10% systematic error of η_{acc}.

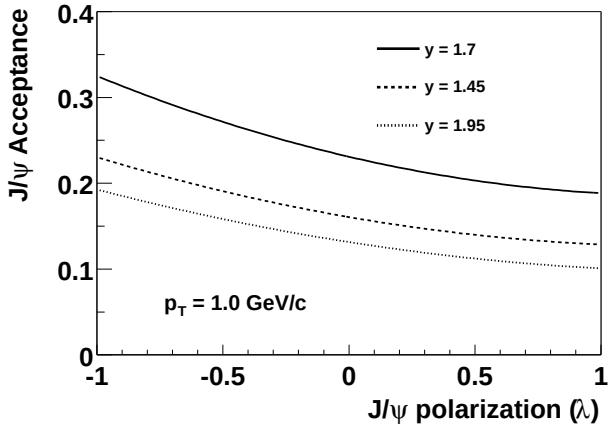

Figure 3.10 J/ψ polarization dependence of the J/ψ acceptance at $p_T = 1$ GeV/c and some y (rapidity) points.

3.3.2 MuID efficiencies

We describe here the technique used to determine the Muon Identifier (MUID) tube efficiencies and the resulting values from Run 3 proton-proton and deuteron-gold data sets which is different from the method which was used and found to underestimate the efficiency(see the details in [166]).

It has been observed that there were various problems with high voltage (HV) units in the MUID during Run 3. Therefore it is important to calculate

tube efficiencies in quantized groups corresponding to the HV chains. In order to have sufficient statistics for this level of granularity, we have used the dimuon triggered data sampled (1D1S and 2D), but correct out this trigger bias.

Efficiency of the specific MuID plane d for a muon, ε_d, is given by

$$\varepsilon_d = \frac{\text{the number of reconstructed roads with a hit in } d}{\text{the number of all reconstructed roads}}$$

for each orientation.

Below is an outline of our procedure.

1. A pass is made through all dimuon triggered data PRDF files in the "good runs" list. See earlier sections for these lists.

2. We use the MUTOO and MUIOO new framework resulting found tracks. In order to be used in the analysis, we require a track that is found in the muon tracker (MUTR) with a matched MUID road. Thus, the tracks must pass the default MUTOO track finding parameters, and more importantly the MUID road must pass the default MUIOO road finding parameters.

3. We remove any trigger and road finding algorithm bias by requiring that all hit requirements are satisfied without the plane of interest. We actually do this in code by setting that plane to have no hit and seeing that all requirements are met, and then setting that plane to have a hit and seeing that all requirements are met. Both checks are necessary because sometimes an extra hit can cause a road to be lost. For example, since the roadfinder requires agreement within +/- 1 for the number of hits in the 1Dim horizontal road and 1Dim vertical road.

We list the relevant checks to remove any bias below.

Trigger Bias Removal:

1. We assume that each track may have to have satisfied the Deep Road Blue Logic Trigger requirement (since in the 1D1S case we do not

know which is shallow and which is deep ahead of time). The BLT requires 7 of 8 hits in planes 0,1,2,3 in a given quadrant.

Thus, if the plane of interest is in planes 0-3, we require all of the other 7 planes to have hits associated with the road.

Road Finding Bias Removal:

1. We use two MUIOO search seed orders (-1,2,1,0,3,4) and (-1,1,2,0,3,4). The (-1) means that the roadfinder starts with the point (x,y,z = 0,0,0) and connects to hits in the next listed plane (either 2 or 1). The roadfinder uses both search orders and then removes completely redundant roads (all hits identical). Thus, we are implicitly requiring a hit in plane (1 or 2) in both horizontal and vertical.

2. We require all MUIOO roads to have $depth == 4$. This requires a hit in either plane 4 vertical or horizontal or both. So if the plane of interest is in plane 4, we require that the other view have a hit in plane 4.

3. We require a minimum depth of each 1D road ($min\_depth\_1d >= 2$). Thus, both horizontal and vertical require at least one hit in (plane 2 or plane 3 or plane 4).

4. We require a minimum number of hits of each 1D road ($min\_nhits\_1d > 2$). Thus there must be at least 3 hits in each 1D road.

5. We require that the depth of the 1D vertical road agree with the depth of the 1D horizontal road within ± 1.

6. We require that the number of hits in the 1D vertical road agree with the number of hits in the 1D horizontal road within ± 1.

Good Run List Weighting

We have calculated the high voltage chain by chain efficiencies for every run in the "good runs" list for north and south arms. We then weight

each run's efficiency by the number of sampled minimum bias events, by using the $BBCLL1 >= 1$ LIVE scaler value for that run. The more correct weighting would be $BBCLL1 >= 1$ LIVE scaler times $|zvtx| < 38/zall$ to get the correction for the number of events in the offline analysis cuts.

It is notable that this weighting, instead of just weighting by the number of tracks found avoids certain assumptions about uncorrelated panel status. If you had 50% of the run with panel 2 off in planes 0 and 1, you would never have a track for those runs and thus not count the lower efficiency. If these states are many and random, then it all averages out.

It was found that using the run weighting for proton-proton data that this lowered the average efficiency by 0.6%.

Random Hit Efficiency Bias

There can be cases where the particle does not leave a hit in a MUID tube due to an inefficiency, but a random other hit falls within the road finding window. This leads to an increase in the MUID efficiencies calculated. We need to remove this random hit bias because our final acceptance and efficiency calculations will be done by embedding Monte Carlo J/psi on top of real data events. The real data events have the random hit contribution already, and thus we would be double counting if we also include this contribution in the tube efficiencies.

One might also be concerned that since we analyze triggered events, they might have a bias towards larger occupancy from tunnel related background.

We have used a simple approximation to remove this random hit bias.

The MUIOO road finder associates new hits that are within ± 30 cm of the current road parameters. As the roadfinder builds up 1D roads, it re-fits points already associated with the road. It then decides whether to associate a new hit if it is within this window of the current parameters projected to that plane. This adds a subtle road search order dependence to the search parameters used in the window cut.

We output an additional ntuple that contains not only the track and MUID road information, but also the residual for each MUID plane. That means we have the distance from the MUID projected road to the nearest hit in a particular plane of the MUID.

From Monte Carlo studies of single muons, we find that real hits are within ±15 cm of the final determined road finder parameters projected to the plane of interest. Thus, we break things down in the following equation.

$$\begin{aligned} total_{1530} &= (1 - real_{eff}) * (1 - rand_{eff}) * rand_{eff} \\ total_{eff} &= real_{eff} + (1 - real_{eff}) * rand_{eff} + total_{1530} \end{aligned} \tag{3.6}$$

The total efficiency for finding a hit within the 30 cm window is equal to the real tube efficiency from the particle of interest (realeff). Then if the real particle does not leave a hit (1 - realeff), you may get a random hit within the 0-15 cm window (randeff). If there is no hit at all within ±15 cm, you may have a random hit within the window $|15-30|$ cm. We assume the probability of getting a random hit within 0-15 cm is the same as 15-30 cm. Remember that these are search windows for 1D roads. Thus, the third term in the expression above is the probability to have no hit within ±15 cm, but to have a hit within ±30 cm.

We can determine from data the ($total_{eff}$) and the last term (eff_{1530}.) We then have two equations and two unknowns and can solve for the real tube efficiency that we are after ($real_{eff}$).

Systematic Checks

We can compare the results from triggered events with those in minimum bias events to see if there is any residual problem. This comparison has been done with the partial production pass for deuteron-gold and find that the results on average agree within 0.2%.

After all the systematic checks, the Muon Identifier (MUID) tube efficiencies from Run 3 proton-proton and deuteron-gold data sets were extracted and used as a input in the simulation. Fig 3.12(see the Fig 3.11 in one dimension plot for all the HV channels) shows the efficiency at the different muid chamber geometry which was divided into quantized groups corresponding to the HV chains. Based on all those studies, the following systematic errors are assigned:

- ±0.2% : Trigger vs. Min.Bias comparison

- + 0.0% - 2% : Random Hit removal assumptions
- ±1% : Sharing between HV chains...

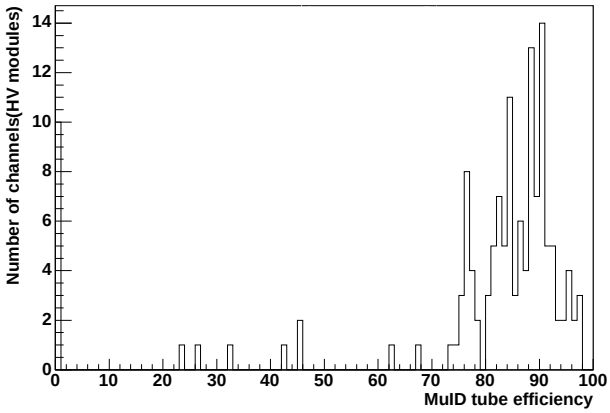

Figure 3.11 Muid tube efficiency in each muid HV modules for run-III p-p data.

Trigger and road-finding efficiencies have been estimated with simulation including the trigger emulator and the MuID chamber efficiencies obtained above for both single muon and dimuon (J/ψ) events. Definition of MuID efficiency for single muons ε^{μ}_{MuID} is given by

$$\varepsilon^{\mu}_{MuID} = \frac{N_{\mu} \text{ with the real MuID efficiencies}}{N_{\mu} \text{ with 100\% MuID efficiencies}}$$

where N_{μ} represents the number of reconstructed muon tracks through a full simulation. The similar definition is applicable for J/ψ's, which is equivalent to $\varepsilon^{J/\psi}_{MuID}$ requiring a dimuon trigger in both the numerator and denominator. For a single muon with $p_z = 5$ GeV/c, 80% efficiency is obtained and 62% for a J/ψ requiring a single or dimuon trigger respectively. These are consistent with a very crude prediction that $\varepsilon^{J/\psi}_{MuID} \sim (\varepsilon^{\mu}_{MuID})^2$ since the average momentum from J/ψ's ($p_z = 5$ GeV/c) is used for the single muon simulation.

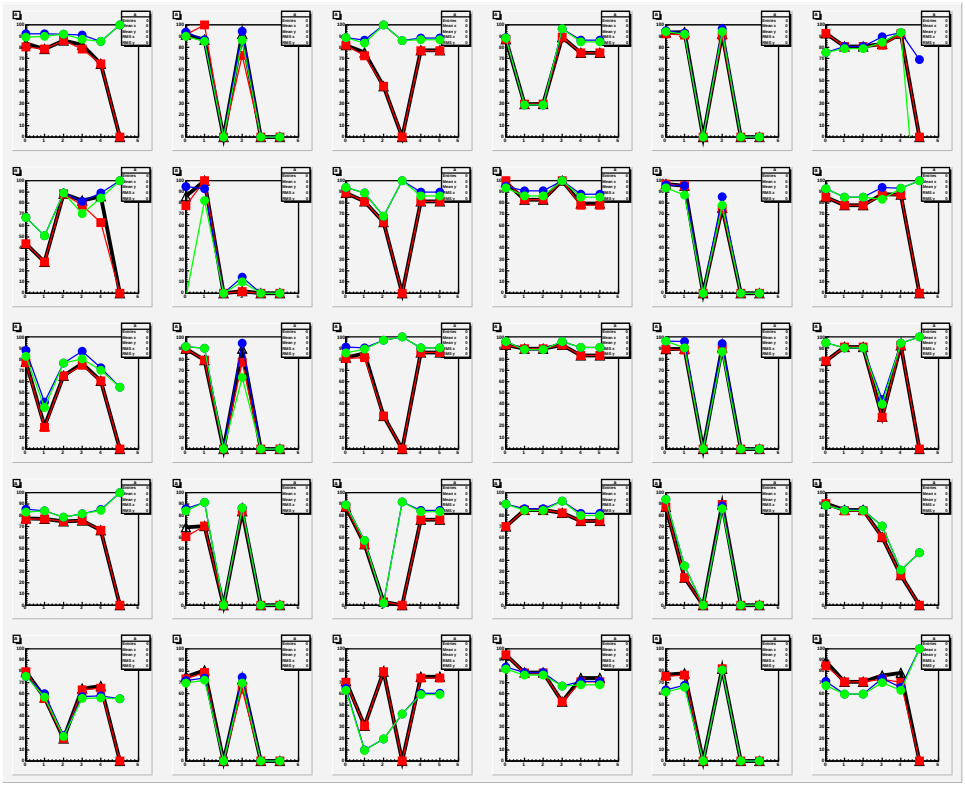

Figure 3.12 Muid tube efficiency in each muid HV modules for run-III p+p and d+Au data. The five gaps of MuID are shown from the top row, the six panels of MuID are shown from the left column. The different color correspond to the different data set(p+p or d+Au) and different correction methods(see details for methods in this section).

In high particle-multiplicity environment such as in Au+Au collisions, road finding efficiency may drop because of difficulty in hit-road associations. However in p+p collisions, much smaller hit occupancy ensures high road-finding efficiency. Figure 3.13 shows distribution of the number of MuID hit channels per event. Most of the minimum-bias triggered events have zero or small hit multiplicities. On the contrary, the hit multiplicity distribution for the single-muon triggered events has a peak around 9 or 10 which is the expected number of hits when a single muon penetrates through the entire MuID (5 gaps $\times$ 2 orientations). This indicates that most of MuID hits are induced by signal muons and not by background hits such as from soft electrons.

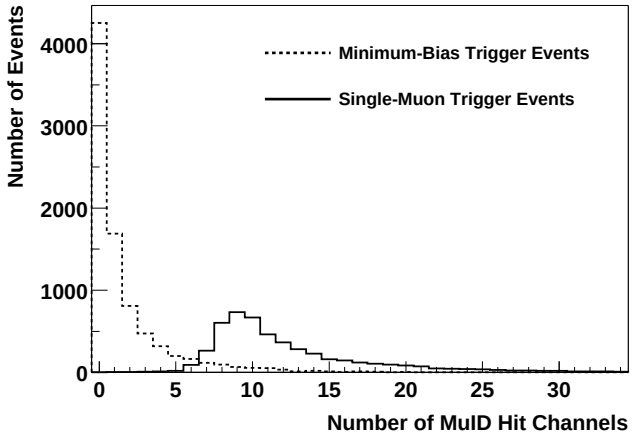

Figure 3.13 MuID hit multiplicity in minimum-bias triggered events (dotted line) and single-muon triggered events (solid line).

Figures 3.14 and 3.15 also show MuID hit multiplicities in single-road events and J/ψ candidate events (unlike-sign dimuons in the J/ψ mass region) respectively, both of which are compared with simulations. For both cases, hit multiplicities agree with simulations and again confirm hit occupancies in the real data are small as expected. Provided valid particle multiplicity of the event generator (PYTHIA) which is confirmed in the next section, this consistency assures response and performance of the detectors

are as expected; thus, no efficiency degradation is suspected.

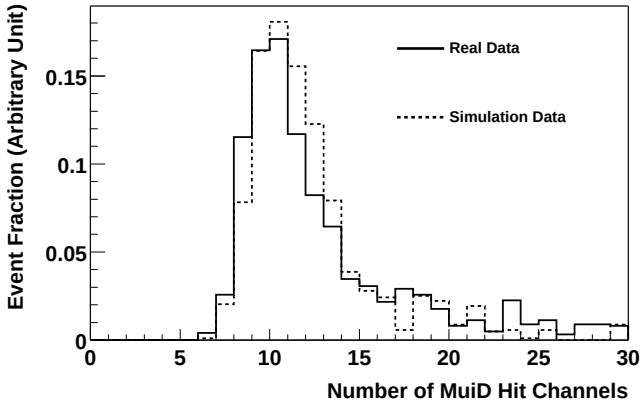

Figure 3.14 MuID hit multiplicity for single-road events. The solid line shows real data and the dotted line shows simulation data.

MuTr efficiencies

Efficiencies of each MuTr plane for a muon are known to be high (99%) inside active detector volumes according to a cosmic ray test. Inactive volumes between octants, which are their frames, are included in the detector acceptance (about 70% for a single track). Some dead Front-End Modules (FEMs) and high-voltage supply chains during the run caused inefficiencies primarily.

A sample run was selected to model MuTr dead FEMs, dead electronics channels and dead high-voltage chains. To examine consistency of the model with the real data, MuTr efficiencies for a single muon ε^{μ}_{MuTr} defined as

$$\varepsilon^{\mu}_{MuTr} = \frac{\text{the number of roads with a track}}{\text{the number of roads}}$$

are obtained using both the real data and simulation to be compared. Tighter cuts are applied to the sample roads to reject as many ghosts as

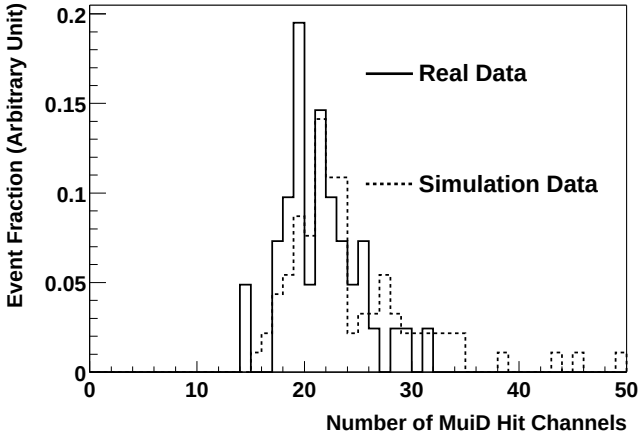

Figure 3.15 MuID hit multiplicity for J/ψ (candidate) events. The solid line shows real data and the dotted line shows simulation data.

possible. Figure 3.16 shows ε^{μ}_{MuTr} as a function of $r_{z=0}$, which is the distance between the origin and the intersection of a road to the $z = 0$ plane. The decrease in efficiency at large $r_{z=0}$ is due to contamination of background roads presumably from beam scraping that has caused high trigger rates as described in section 2.7.2. The cut $r_{z=0} < 50$ cm is applied to eliminate them. Other road quality parameters are checked in the same way and confirmed to be valid. About 80% of the road sample is dominated by hadron-decays as demonstrated by the BBC z-vertex distribution as already shown in Fig. 3.8. A fraction of ghost roads is further constrained by z-vertex dependence of ε^{μ}_{MuTr}, because efficiency is sensitive to the fraction of non-ghost roads with z-vertex dependence, which is dominated by decay muons. Actually, there is no significant dependence on BBC z-vertex as shown in Fig. 3.17. The fraction of the ghost roads to the road sample is constrained by fitting it assuming a flat z-vertex distribution for them and estimated to be less than 5%.

Figure 3.18 shows MuTr efficiencies for both the real and simulation data as a function of the azimuthal angle of the qualified roads. There is a reasonably good agreement of the real data and simulation with exception

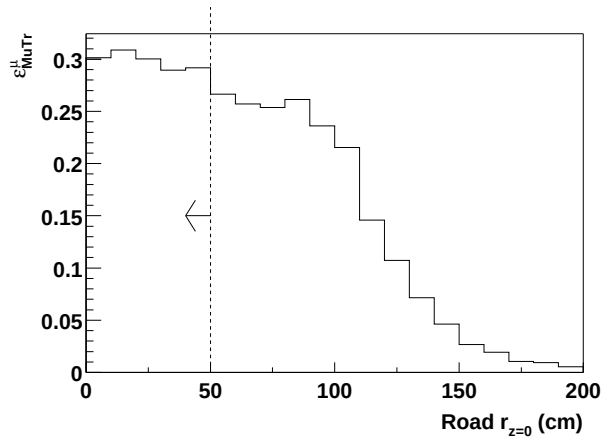

Figure 3.16 MuTr efficiency ε^{μ}_{MuTr} as a function of $r_{z=0}$ of roads. See the text for the definitions of ε^{μ}_{MuTr} and $r_{z=0}$. The dotted line and the arrow represent the quality cut to select good roads used for the MuTr efficiency calculation.

of the region(Station 2 North chambers) in which we found that a number of cathode strips chambers were apparently scratched in the active volume of the chamber. This resulted in reduced charge collection on these strips. We attempted to determine all such strips using real data and tagged the affected strips in the database. Then in the reconstruction code all of these strips were given a large RMS value when fitting clusters and determining the resolution of fitted clusters. This should result in more accurate chi-square values and slightly improved cluster fitting results in some cases, but we don't expect too much improvement in the final mass resolution because of the lost charge information. Therefore we assign a systematic error of 5% to $\varepsilon^{J/\psi}_{MuTr}$ of this particular run based on the disagreement between the simulation and real data. To minimize an uncertainty due to run dependence of MuTr efficiency, only runs with a high duty fraction are selected and used for the analysis. The run selection criteria is shown at table 3.1.

The muon overall tracker efficiency for J/ψ events is evaluated along with the muon identifier and the muon trigger using a full simulation of

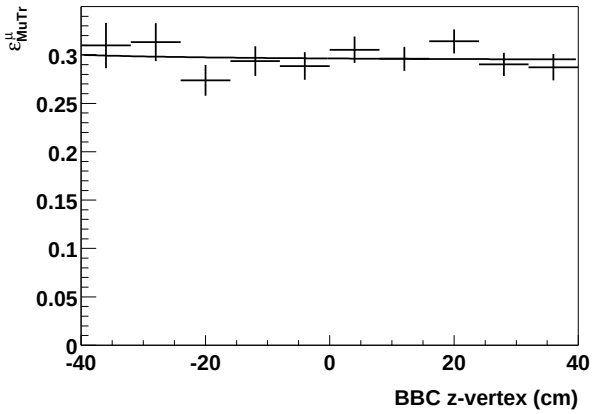

Figure 3.17 MuTr efficiency ε^{μ}_{MuTr} as a function of the BBC z-vertex. See the text for the definition of ε^{μ}_{MuTr}. The error bars are statistical errors for one particular run. The line shows a fit to the data with a function assuming a constant fraction of ghost roads, which is determined to be less than 5%.

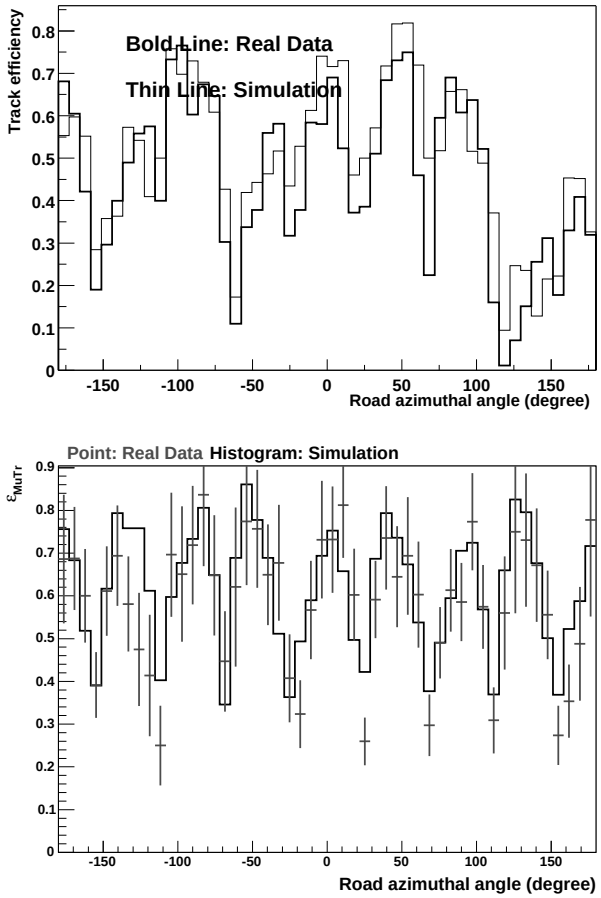

Figure 3.18 MuTr efficiency ε^{μ}_{MuTr} as a function of the azimuthal angle of roads. See the text for the definition of ε^{μ}_{MuTr}. The points with a statistical error are for the real data and the histogram is for the simulation data. Statistical errors of the simulation data are omitted, which are comparable with those of the real data (run-II(top), run-III(bottom)).

the detector for Pythia generated J/ψ events as outlined in section 3.2.1 to 3.2.6. One input to these simulations is the intrinsic efficiency of the muon tracker planes. As mentioned in 3.2.1 this was taken as 99%. A data driven method of evaluating this efficiency was accomplished by using good muon identifier roads to project back into the tracker and determine the efficiency for finding these tracks in the tracker. This method can be used for both simulated events and for real data events. But in the later case, one has to be very careful to select clean real roads that correspond to real tracks going all the way through the muon tracker stations. Comparisons between simulation and data at present show good agreement for the South muon tracker but only fair agreement for the North muon tracker. But further cuts on the quality of the roads seems to be converging towards good agreement for both arms. A systematic uncertainty allowing for the present state of this verification of the muon tracker plane efficiencies is included in the later section 3.6 about systematics.

Just as for the analysis, we used PYTHIA v5.720 with GRV-98 parton distribution functions to generate the J/ψ's used in determining our acceptant and efficiency. The J/ψ could be primary or from a χ_c decay. We forced the $J/\psi \to \mu^+\mu^-$ decay with no kinematic cuts over 4π.

3.3.3 Embedding studies

For realistic background and chamber occupancies, we embedded the simulated muon hits from J/ψs into real dAu MinBias events in several centrality bins. The dAu files chosen for embedding had to have the same HV state as the simulated data and a sufficient number of events. We used the runs 78838, 79863, 80312 for the HV state 79863. The difference in efficiency obtained between clean J/ψ events and J/ψ events embedded in real events was shown in table 3.5 which are statistics limited at the 3% level. Based on this we assign a systematic error from embedding of 3%. We used the same version of track reconstruction as we used for real data reconstruction for this study. The mass distribution produced by Monte Carlo when J/ψ are thrown over the entire acceptance of the arms, mixed with real dAu 0-20% central events are shown in the Figure 3.19.

Centrality	Arm	Thrown	Reconstructed (No embedding)	Reconstructed (embedding)	$A \times \varepsilon^{4\pi}_{J/\psi}$ (No embedding)	$A \times \varepsilon^{4\pi}_{J/\psi}$ (embedding)
0-20%	South	12451	659	653	5.29+-0.21%	5.24+-0.21%
20-40%	South	14642	796	797	5.43+-0.20%	5.44+-0.20%
40-60%	South	15801	855	863	5.41+-0.19%	5.46+-0.19%
60-88%	South	24845	1309	1337	5.26+-0.15%	5.38+-0.15%
0-20%	North	13901	1011	1023	7.27+-0.24%	7.35+-0.24%
20-40%	North	16453	1212	1226	7.36+-0.22%	7.45+-0.22%
40-60%	North	17684	1292	1307	7.30+-0.21%	7.39+-0.21%
60-88%	North	27885	2030	2088	7.27+-0.17%	7.48+-0.17%

Table 3.5 Summary of the embedding results : clean J/ψ events are embedded in real dAu events in each centrality bins. errors in the table are only statistical

3.3.4 BBC efficiency for p+p $\rightarrow J/\psi X$ events

Efficiency of the BBC for p+p $\rightarrow J/\psi X$ events ($\varepsilon^{J/\psi}_{BBC}$), where a J/ψ decays into a muon pair detected in the South Muon Arm, is estimated to be 0.74 ± 0.01 (stat.) from simulation studies using PYTHIA and GEANT. No significant p_T nor rapidity dependence has been found. This factor is closely related to $\varepsilon^{inela}_{BBC}$ which is BBC efficiency for p+p inelastic events and will be described in section 3.3.6. The systematic error of $\varepsilon^{J/\psi}_{BBC}$ will also be discussed there.

3.3.5 Total detection efficiency

Total detection efficiency $\varepsilon^{J/\psi}_{tot}$ is given by

$$\varepsilon^{J/\psi}_{tot} = \frac{\text{the number of reconstructed } J/\psi\text{'s in } 1.2 < y < 2.2}{\text{the number of simulated } J/\psi\text{'s in } 1.2 < y < 2.2}$$

with a simulation including the MuID, MuTr and BBC efficiencies obtained in the previous sections. Run-averaged values are used for the MuID part. For the MuTr part, dead FEMs, high-voltage chains and real ADC gains with the particular run are used. About 88 000 PYTHIA events with unpolarized J/ψ's are simulated and $\varepsilon^{J/\psi}_{tot}$ is obtained which is $(1.19 \pm 0.03)\%$. where the error stands for the statistical error of the simulation. PYTHIA's p_T and rapidity distributions are consistent with the real data as shown in the next section.

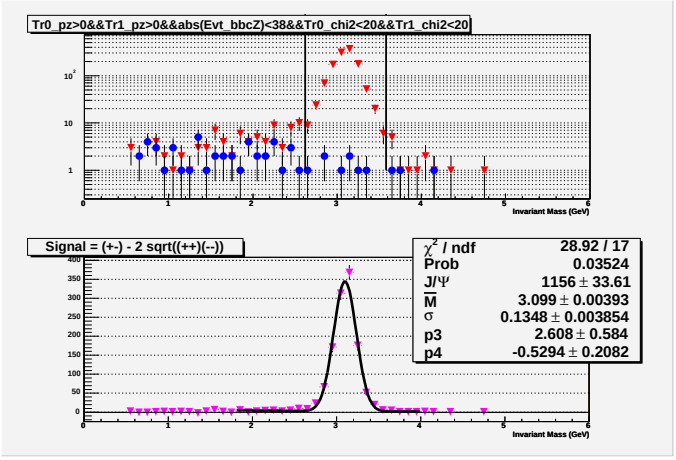

Figure 3.19 The mass distribution produced by Monte Carlo when J/ψ are thrown over the entire acceptance of the north arm, mixed with real dAu 0-20% central events

Transverse momentum (p_T) and rapidity (y) dependence are shown in Figs. 3.20 and 3.21 respectively. Error bars represent statistical errors of the simulation. Relatively small p_T dependence of $\varepsilon_{tot}^{J/\psi}$ is found in the range $0 < p_T < 5$ GeV/c which is the statistical limit of our measurement. For the calculation of differential cross sections for J/ψ production, averaged values are used in each rapidity or p_T bin shown in Tables 4.1 in chapter 4. A slight decrease in $\varepsilon_{tot}^{J/\psi}$ at higher p_T is due to the bias of the dimuon trigger which requires two different quadrants to be fired, thus losing some J/ψ's with a smaller opening angle between two muons. A systematic error of $\varepsilon_{tot}^{J/\psi}$ due to the uncertainty of J/ψ's p_T distribution is estimated to be small ($< 2\%$) by changing efficiency values in each p_T bin within their statistical uncertainties. Rapidity distribution is sensitive to gluon density in the proton. A systematic error of $\varepsilon_{tot}^{J/\psi}$ due to the uncertainty of the rapidity distribution is studied using PYTHIA with various parton distribution functions. As a result the variation of $\varepsilon_{tot}^{J/\psi}$ is found to be negligible ($< 2\%$).

The systematic errors of each factor of $\varepsilon_{tot}^{J/\psi}$ is summarized in Table 3.14 in section 3.6.

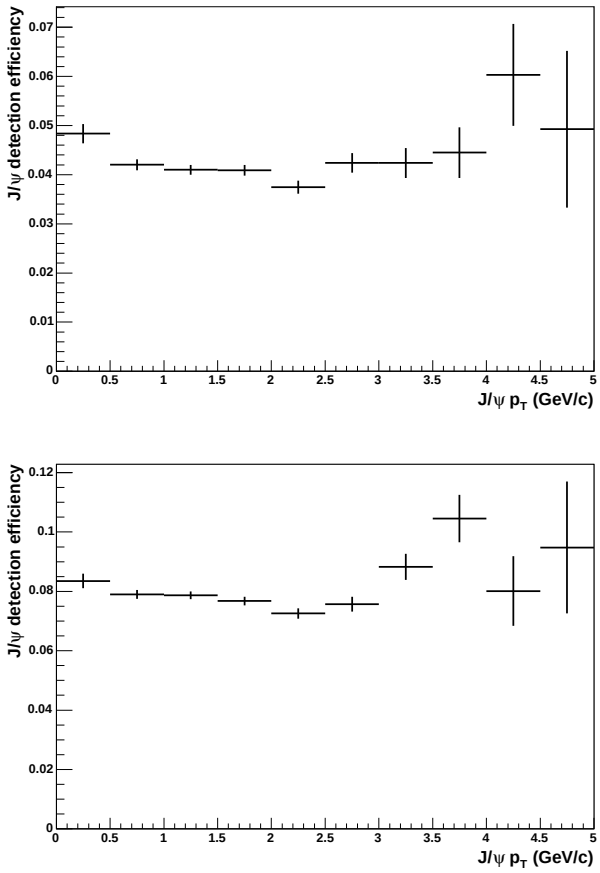

Figure 3.20 Transverse momentum (p_T) dependence of J/ψ detection efficiency ($\varepsilon_{tot}^{J/\psi}$). Error bars are for statistical errors of the simulation(top:south,bottom:north).

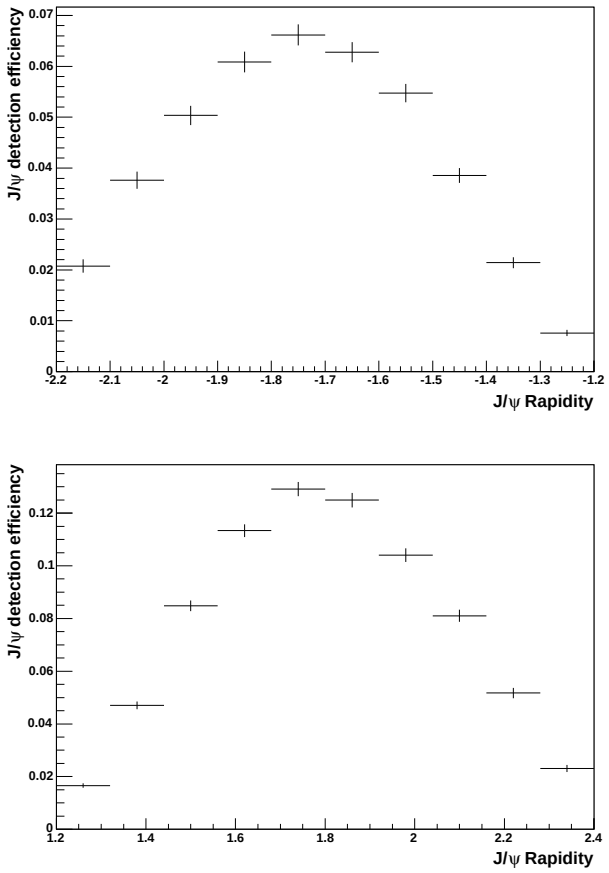

Figure 3.21 Rapidity dependence of J/ψ detection efficiency ($\varepsilon_{tot}^{J/\psi}$). Error bars are for statistical errors of the simulation(top:south,bottom:north).

3.3.6 Integrated luminosity

The integrated luminosity used for this analysis is given by

$$\mathcal{L} = \frac{N_{MB}^{|z_{vtx}|<38\,\mathrm{cm}}}{\varepsilon_{BBC}^{inela}\,\sigma_{inela}} \tag{3.7}$$

where

$N_{MB}^{\lvert z_{vtx}\rvert<38\,\mathrm{cm}}$:	the number of minimum bias triggers with an offline BBC z-vertex cut,
$\varepsilon_{BBC}^{inela}$:	efficiency of the BBC for p+p inelastic events with the same vertex cut, and
σ_{inela}:	p+p inelastic cross section.

Analysis procedures to obtain these factors will be described in the following.

Number of minimum bias triggers

The number of minimum-bias triggered events integrated over all the selected runs is represented as $N_{MB}^{|z_{vtx}|<38\,\mathrm{cm}}$, with an offline BBC z-vertex cut $|z_{vtx}| < 38$ cm. Since most of minimum bias triggers have been prescaled (see section 2.7.1), it is not possible to obtain un-prescaled values of $N_{MB}^{|z_{vtx}|<38\,\mathrm{cm}}$. Instead it is calculated as

$$N_{MB}^{run_i,|z_{vtx}|<38\,\mathrm{cm}} = N_{MB,\,\mathrm{live}}^{run_i} \times \frac{N_{MB,\,\mathrm{prescaled}}^{run_i,|z_{vtx}|<38\,\mathrm{cm}}}{N_{MB,\,\mathrm{prescaled}}^{run_i}} \tag{3.8}$$

for each run where un-prescaled (live) counts of all minimum-bias triggers $N_{MB,\mathrm{live}}^{run_i}$ are obtained from the run control log and the ratios of minimum bias events with a BBC z-vertex cut ($N_{MB,\,\mathrm{prescaled}}^{run_i,|z_{vtx}|<38\,\mathrm{cm}}$) to all minimum bias events ($N_{MB,\,\mathrm{prescaled}}^{run_i}$) for each run are obtained from the prescaled data. Intergated over all the runs used for the J/ψ analysis, 1.72×10^9 has been obtained with a very small statistical error.

The fraction of the number of triggers from beam-related background is found to be less than 0.1% with the beam test, where the rate of the

BBLL1 trigger was reduced from 10 kHz to 2∼3 Hz when beams were mis-steered. Crossing-by-crossing variation for minimum-bias triggered events, shown in Fig. 3.22, also give us an estimation of the magnitude of the background. Since beam-related background events happen randomly, its fraction is estimated by the ratio of the number of events in non-collision crossings (even numbers in the figure) to the number of events in collision crossings (odd numbers in the figure). If a BBC z-vertex ($|z_{vtx}| < 75$ cm) is required (the upper figure), the ratio is less than 0.1%. On the other hand, it goes up to 10% if no BBC z-vertex required (the lower figure), which means NTC-exclusive triggered events suffer from beam-related background by 10%.

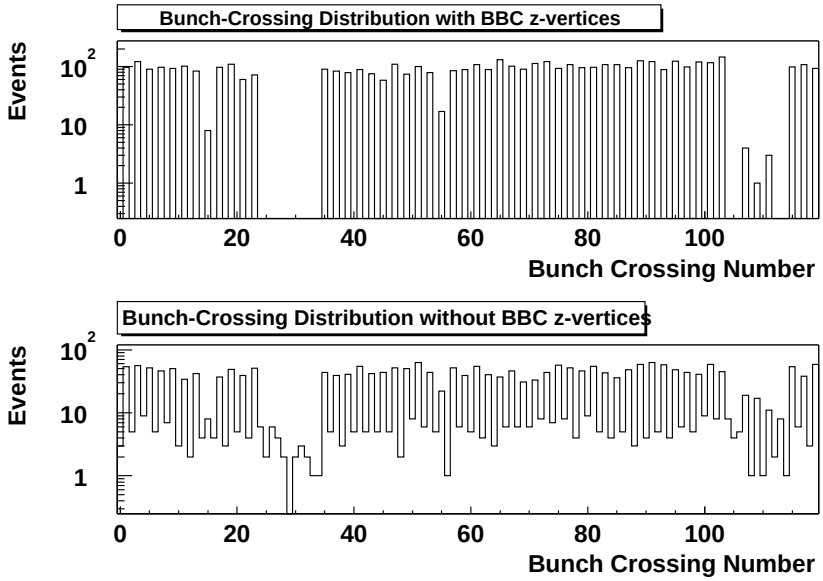

Figure 3.22 Crossing-by-crossing variation for minimum-bias triggered events with (upper) and without (lower) a BBC z-vertex cut ($|z_{vtx}| < 75$ cm). Even numbers are for non-collision crossings and odd numbers are for collision crossings. Events in non-collision crossings are supposedly induced by beam-related background.

p+p inelastic cross section

The total p+p cross section σ_{tot} at $\sqrt{s} = 200\,\mathrm{GeV}$ has not been measured yet. Following parametrization for σ_{tot} as a function of $\sqrt{s}$ is given in [139] as well as fit parameters, which reproduce experimental data well.

$$\sigma_{tot} = Z + B\log^2(s/s_0) + Y_1(s)^{-\eta_1} - Y_2(s)^{-\eta_2} \tag{3.9}$$

where Z, B, Y_i are in mb and s and s_0 are in GeV^2. The first and second terms, which represent the pomeron contribution, dominates at high $\sqrt{s}$. The exponents η_1 and η_2 represent lower-lying C-even and C-odd exchanges, respectively. From the fitted parameters given there, σ_{tot} is determined to be 51.5 ± 1.1 mb at $\sqrt{s} = 200$ GeV. Elastic cross section σ_{ela} is also obtained (10.2 ± 0.3 mb), yielding the inelastic cross section of $\sigma_{inela} = \sigma_{tot} - \sigma_{ela} = 41.3 \pm 1.2$ mb.

Pseudo-rapidity range of protons from elastic p+p scattering is $5 < |\eta| < 9$ which is out of BBC acceptance, thus being excluded from the luminosity calculation.

BBC efficiencies

Efficiencies of the BBC for inclusive p+p inelastic events, $\varepsilon_{BBC}^{inela}$, and for p+p $\rightarrow J/\psi X$ events, $\varepsilon_{BBC}^{J/\psi}$, are sensitive to charged particle multiplicity which has not been measured at $\sqrt{s} = 200$ GeV before. We have used the event generator PYTHIA to estimate them, whose consistency with the real data is fully examined.

PYTHIA and the PHENIX detector simulation using GEANT give $\varepsilon_{BBC}^{J/\psi} = 0.74 \pm 0.01$ and $\varepsilon_{BBC}^{inela} = 0.51 \pm 0.01$ respectively with a $|z_{vtx}| < 38$ cm cut, where errors are statistical errors of the simulation. Because of higher multiplicities in p+p $\rightarrow J/\psi X$ events than in inelastic events on average, $\varepsilon_{BBC}^{J/\psi}$ is larger than $\varepsilon_{BBC}^{inela}$. No significant p_T nor rapidity dependence has been found for $\varepsilon_{BBC}^{J/\psi}$.

To cross-check these results for their validities, relative efficiency $R = \varepsilon_{BBC}^{inela}/\varepsilon_{MB}^{inela}$ is compared with the real data, where ε_{MB}^{inela} is efficiency of the MB (minimum bias) trigger, logical OR of BBC and NTC triggers, for p+p inelastic events. From simulation, $R = 0.51/0.70 = 0.73$ is obtained with

a 1% statistical error. However, NTC trigger rate has suffered from beam-related background which is not included in the simulation. Its fraction is about 10% at maximum as described in section 3.3.6. Therefore R is expected to vary from 0.67 to 0.73. Figure 3.25 shows run statistics for the relative rate of the BBC trigger to the minimum-bias trigger which is identical to R. The distribution is consistent with the expectation from the simulation and background rate. The lower tail is due to runs with higher background (or NTC trigger) rate. Even at the highest rate, contamination of the beam scraping background to physics events is expected to be small ($< 10^{-3}$).

BBC efficiencies are sensitive to particle multiplicities especially in and near the BBC acceptance ($3.0 < |\eta| < 3.9$) given by the event generator. Figure 3.23 shows comparison of PYTHIA with the UA1 data [140] for the p_T spectrum for inclusive charged hadrons at central rapidity ($|\eta| < 2.5$) in p+$\bar{\text{p}}$ collisions at $\sqrt{s} = 200$ GeV. They are in good agreement to 20% precision. Since gluon-gluon scattering dominates the inclusive charged-particle yield for both p+p and p+$\bar{\text{p}}$ collisions, the consistency in p+$\bar{\text{p}}$ collisions indicate the consistency in p+p collisions. In Run-2 at RHIC, p_T differential cross sections for the neutral pion production have been actually measured in the PHENIX Central Arms ($|\eta| < 0.35$) in p+p collisions at $\sqrt{s} = 200$ GeV which agree with the UA1 results in the range $p_T < 4$ GeV/c to about 10% precision [141]. Figure 3.24 shows comparison of PYTHIA with the UA5 data [142] for the charged-particle pseudo-rapidity distributions in p+$\bar{\text{p}}$ collisions at $\sqrt{s} = 200$ GeV. PYTHIA distribution is again consistent with the real data to 20% precision. A systematic error of $\varepsilon_{BBC}^{inela}$ from uncertainty of particle distribution is estimated by changing charged particle multiplicity in PYTHIA by 20% tuning parameters on the fragmentation function [1] and changes of $\varepsilon_{BBC}^{inela}$ are found to be 15% or less. PDF (parton distribution function) dependence is also studied and is found to be smaller (3%). Therefore a 15% systematic error is assigned to $\varepsilon_{BBC}^{inela}$ from the uncertainty of the initial particle distribution. The relative trigger rate R is 0.80 when particle multiplicity is increased by 20% and 0.66 when

[1] for example, change PARJ(41) from 0.3 to 1.3 and PARJ(42) from 0.58 to 1.58, which represent the parameters a and b respectively in the Lund fragmentation function $f(x) \propto z^{-1}(1-z)^a \exp(-bm_\perp^2/z)$

decreased, both of which are deviated from the measurement and indicating the particle multiplicity with the original PYTHIA parameters reproduces the real data well.

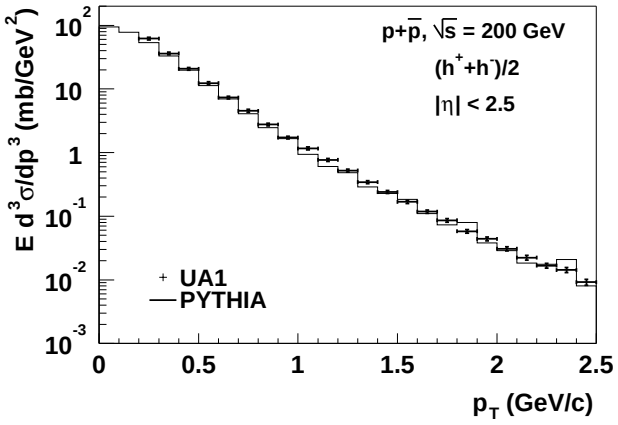

Figure 3.23 Inclusive cross section for single charged hadrons in p+$\bar{\text{p}}$ collisions at $\sqrt{s} = 200$ GeV as a function of p_T of hadrons. The points with error bars are for the UA1 data [140] and the histogram is for a PYTHIA prediction.

In the p+p run, event vertex distribution varied from 40 cm to 70 cm in rms. If $\varepsilon_{BBC}^{inela}$ had a significant dependence on the z-vertex position, it would be affected by the change in the vertex distribution. However, no z-vertex dependence within $|z_{vtx}| < 38$ cm is actually found over the statistical uncertainty of the simulation study ($< 3\%$); hence, no fluctuation in $\varepsilon_{BBC}^{inela}$ is expected during the run.

High-voltage potentials applied to each PMT (photomultiplier tube) of the BBC were stable during the run. However there is PMT by PMT fluctuation in discriminator-threshold values possibly by 10 to 20% which is not reflected in the simulation. It gives rise to an uncertainty of $\varepsilon_{BBC}^{inela}$. However it is found to be small ($< 5\%$) with a simulation by conservatively doubling and halving all the PMT threshold values.

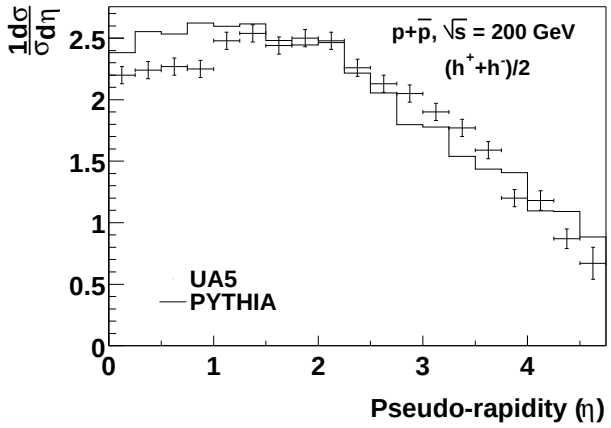

Figure 3.24 Charged particle pseudo-rapidity distribution in p+$\bar{\text{p}}$ collisions at $\sqrt{s} = 200$ GeV. The points with error bars are UA5 data [142] and the histogram is for PYTHIA.

As the ver der Meer scan [2] result, $\varepsilon_{BBC}^{inela} \times \sigma_{inela}$ has also been determined to be 18.5 $\pm$ 1.9 mb. This is consistent with $\varepsilon_{BBC}^{inela}$ obtained with the simulation times σ_{inela} obtained in the previous subsection within their errors.

The same magnitude of uncertainty is expected on $\varepsilon_{BBC}^{J/\psi}$. However, some systematic uncertainties of $\varepsilon_{BBC}^{inela}$ and $\varepsilon_{BBC}^{J/\psi}$ will be canceled out since the total cross section is proportional to their ratio. For example, if particle multiplicity is higher in inelastic events, it tends to have higher multiplicity also in $J/\psi \to \mu^+\mu^-$ events. Therefore a smaller systematic error of $\varepsilon_{BBC}^{J/\psi}$ is assigned which is 10%.

BBC efficiency for another hard scattering events in p+p collisions, π^0 production events, has been measured in the Central Arms ($|\eta| < 0.35$) in Run-2 [141]. It is relatively p_T independent and consistent with a PYTHIA simulation within a few percent of errors, as shown in Fig. 3.26. It confirms that PYTHIA reproduces particle multiplicities in p+p hard scat-

[2] a technique to measure the cross section of a beam by steering

tering events for which BBC efficiency is scale and (supposedly) process independent.

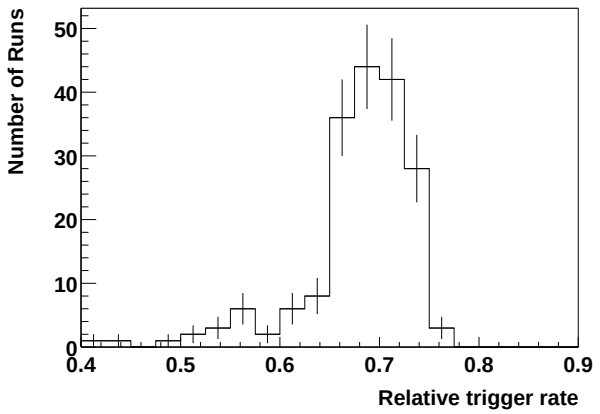

Figure 3.25 Run statistics for the relative trigger rate, BBC/MB, where MB (minimum bias) is the logical OR of the BBC and NTC triggers. The lower tail is due to the runs with higher NTC trigger rate from background.

3.3.7 Fitting dimuon spectra

Applying the cuts given in section 3.2.9, we find the $\mu^+\mu^-$ spectra given by the red triangle histograms on figures 3.27 to 3.32 for our various data samples. J/ψ peaks can clearly be seen.

Combinatorial background

Most of the background under the peaks is due to the combinatorics of uncorrelated muons. To subtract this background, we rely on the like sign events. The spectra of the $\mu^+\mu^+$ and $\mu^-\mu^-$ are shown in green stars and light blue triangles, the blue circles being the sum.

A rough estimate of the number of J/ψ is given by the subtraction of the unlike sign to the like sign pairs in a given mass window. This method was

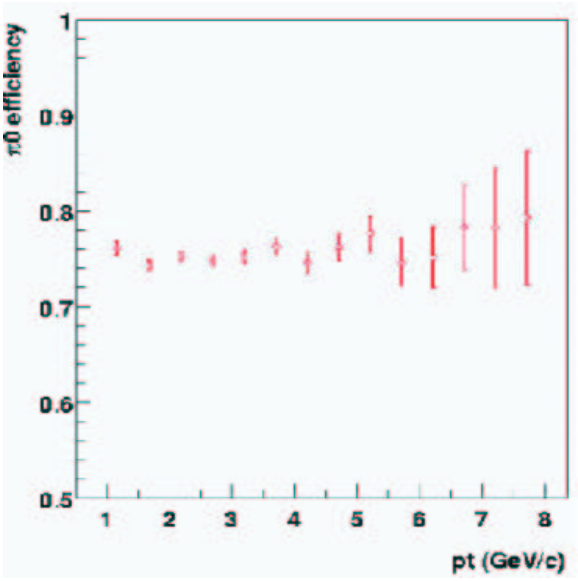

Figure 3.26 BBC efficiency for p+p $\rightarrow \pi^0 X$ events as a function of p_T of π^0 measured in the Central Arms ($|\eta| < 0.35$) [141].

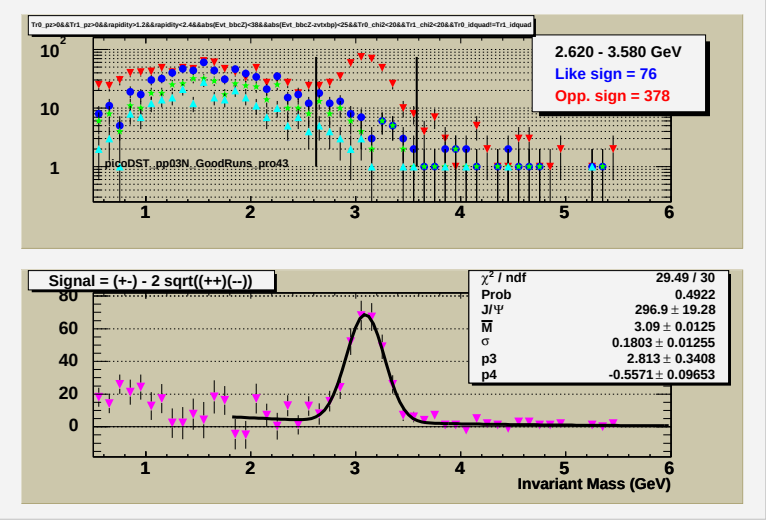

Figure 3.27 Invariant dimuon mass distributions for proton+proton data in the north arm. Top plot : $\mu^+\mu^-$ (red triangles), $\mu^+\mu^+$ (green stars), $\mu^-\mu^-$(light blue triangles) and $\mu^+\mu^+ + \mu^-\mu^-$ (blue circles). Bottom plot : background subtracted distribution fitted by an exponential plus a gaussian function.

applied for the run 2 result [185]. Given the higher statistics we have, we move to a more accurate method, to reflect that N_{++} (the number of $\mu^+\mu^+$ pairs) is not equal to N_{--} (the number of $\mu^-\mu^-$ pairs) as it can clearly be seen on the plots. The combinatorial background is thus determined by counting N_{++} and N_{--} that pass the same cuts as N_{+-}, and estimated with $N_{bkg} = 2\sqrt{N_{++} \times N_{--}}$.

The bottom purple triangle histogram on figures 3.27 to 3.32 is then : $N_{+-} - 2\sqrt{N_{++} \times N_{--}}$ (aka : $purple = red - 2\sqrt{green \times lightblue}$).

We're also working on two other subtraction methods :

1. One is to fit individually the $\mu^+\mu^+$ and $\mu^-\mu^-$ spectra above 2 GeV by exponentials and to build up $N_{bkg} = 2\sqrt{N_{++} \times N_{--}}$ based on the resulting functions. This shows the advantage to wash out statistical fluctuations, which are large in the high mass region.

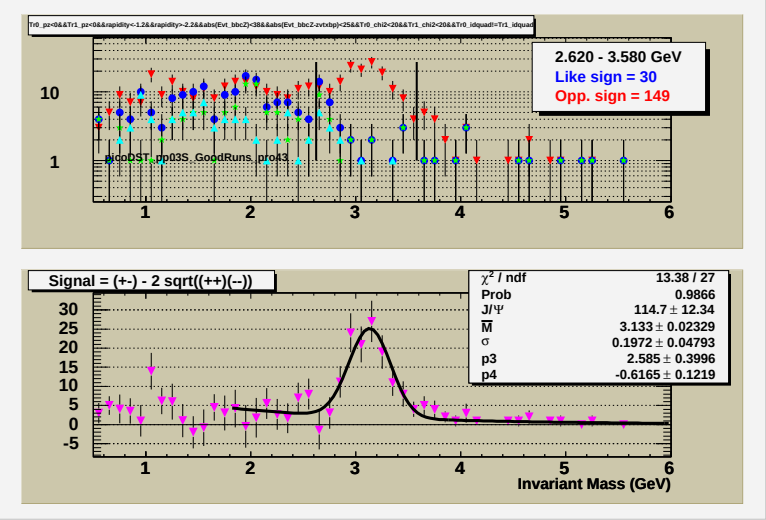

Figure 3.28 Invariant dimuon mass distributions for proton+proton data in the south arm.

2. However, the two methods above uses the assumption that there is no charge asymmetry introduced by the detector acceptance. An alternative approach is to build up combinatorial background by mixing single muons from different events. This method is under development but already shows good agreement with the $N_{bkg} = 2\sqrt{N_{++} \times N_{--}}$ method.

The differences between the fitting method 1 above and our subtraction method stays within 5% for our global samples. Higher differences are seen when we split the data in centrality, transverse momentum or rapidity bins. They all have been carefully investigated and are mostly due to changes in the physical background slope estimation, and thus are being covered by the systematic error quoted in the following section.

The method 2 gives correction factors that are also less than 5%. Thus we assign a 5% systematic error for the combinatorial background estimation and subtraction.

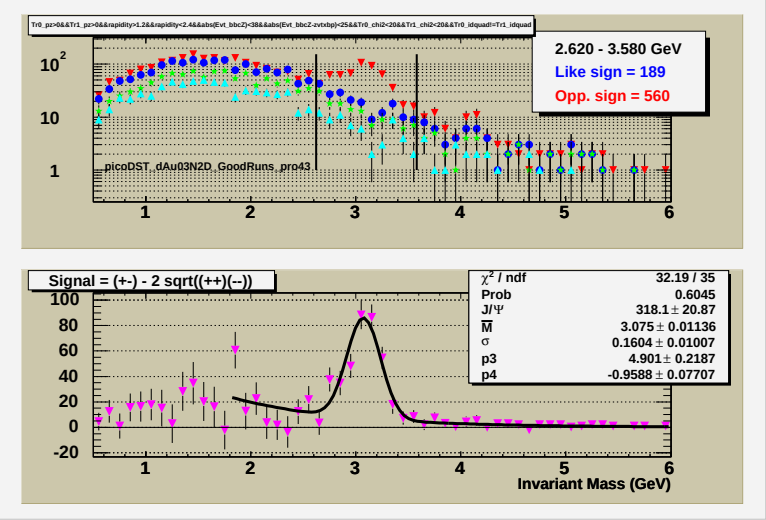

Figure 3.29 Invariant dimuon mass distributions for deuteron+gold data in the north arm (2D triggers).

Physical background

Once we have subtracted the combinatorial background, we are left with the purple triangles bottom curves, which should mostly be made of physically correlated muons. We see on this plots that we have some signals below and above the J/ψ mass region, and also a hint of the ψ'. Studies are being made to understand this background in terms of open charm (low mass) and Drell-Yann (high mass). For this preliminary result, we derive the number of J/ψ doing a simple gaussian + exponential fit such as the ones displayed on the figures. The fits lead to reasonable masses and resolutions. The exponential slopes are consistent between the four dAu samples, and separately on the two pp samples, giving us confidence that we're fairly describing the backgrounds.

However, we have tried to fit the signal shapes with many different functions and find that they all fairly describe the data :

1. Gaussian + exponential between 1.4 to 6.0 GeV (used to derive the final numbers).

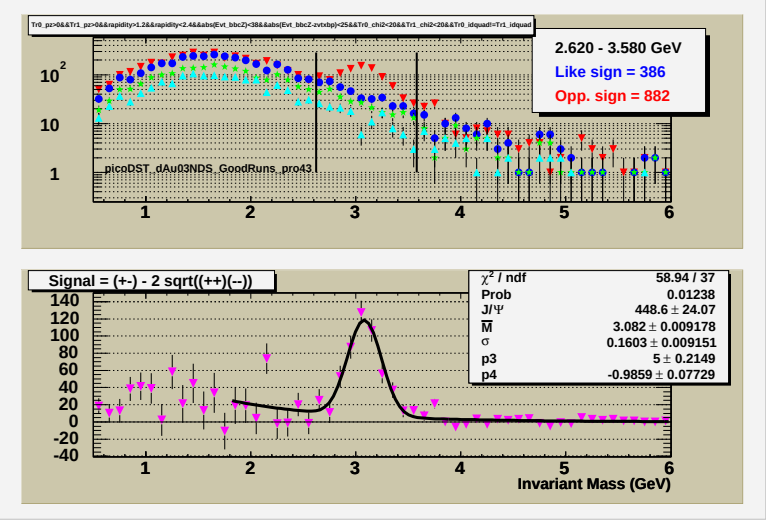

Figure 3.30 Invariant dimuon mass distributions for deuteron+gold data in the north arm (1D1S triggers).

2. Gaussian + exponential with a different fitting range (between 1.8 and 6.0 GeV for the plots presented here and in the table 3.6, but we have tried other values).

3. Gaussian + quadratic polynomial.

4. J/ψ gaussian + ψ' gaussian (Δm from PDG and same resolution) + exponential.

5. J/ψ gaussian + ψ' gaussian (Δm from PDG and same resolution) + 2 exponentials (low slope at high mass for Drell-Yann and high slope at low mass for open charm, both inspired from preliminary montecarlo simulation).

6. Simple Gaussian with no background, leading to results which are very close to the previous method.

7. Gaussian + an exponential constraint to fade out under the peak, basically leading to no background contribution in the J/ψ mass region.

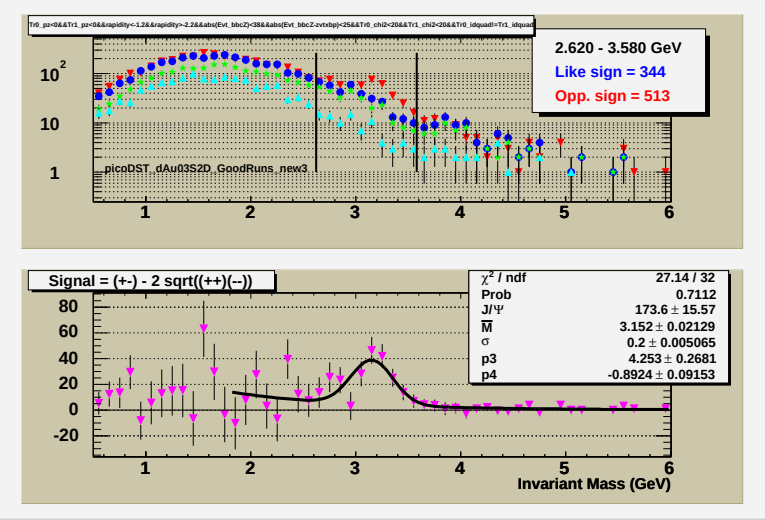

Figure 3.31 Invariant dimuon mass distributions for deuteron+gold data in the south arm (2D triggers).

The results of all these methods are given in table 3.6. The two last methods give reasonable χ^2 probabilities and cannot be totally ruled out without further understanding and simulation of our backgrounds. Thus we assign for now a systematic error on our fitting procedure equal to the difference of our fit to the no background hypothesis, divided $\sqrt{12}/2$.

The methods 1 to 5 give results that are much closer from one another, the differences being far below the systematic errors computed above.

For the dAu/pp ratio, we take the differences between the highest and the lowest estimation and divide it by $\sqrt{12}$.

Fitting subsamples

When we divide the data samples into rapidity, transverse momentum or centrality bins, we use the exponential + gaussian fit, applying some constraints based on the results obtained from the global sample fit. Typically, here are the constraints we have to apply to make all the fits to converge :

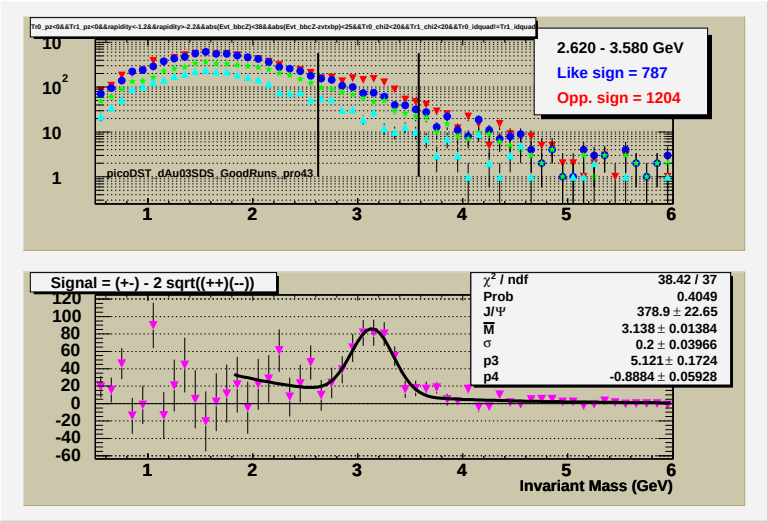

Figure 3.32 Invariant dimuon mass distributions for deuteron+gold data in the south arm (1D1S triggers).

- Fit being done between 1.4 and 6 GeV to ease the exponential slope estimation.
- 3.05 < gaussian centroid < 3.16 GeV.
- 150 < sigma < 200 MeV.
- 0 < Expon. Norm < 200.
- 0 < Expon. Slope < 3. $(-1/p4$ in the plots)

For each binning and each sample, we checked that the sum of the numbers of J/ψ's found on each bin is roughly equal to the number found on the global sample.

system	arm	1. e+g	2. e+g	3. q+g	4. e+2g	5. 2e+2g	6. gaus	7. e+g	error
dAu	N	784(32)	772(32)	742(31)	766(31)	828(32)	925(31)	928(31)	10.34%
dAu	S	578(27)	559(28)	522(27)	565(33)	553(27)	697(27)	710(27)	11.88%
pp	N	290(19)	270(19)	286(13)	292(19)	292(19)	326(18)	332(18)	7.12%
pp	S	118(12)	115(13)	109(13)	111(12)	111(12)	128(11)	132(12)	4.69%
dAu/pp	S	4.88	4.87	4.78	5.10	4.99	5.45	5.40	3.7%
dAu/pp	N	2.70	2.86	2.60	2.62	2.83	2.83	2.79	2.8%

Table 3.6 Systematic uncertainties associated with the shapes and background descriptions used for fitting the mass spectra and extracting the J/ψ yields. The last column is the systematic errors derive from this comparison.

3.4 Cross Section Input Variables

We give below all the input variable used for the final cross section calculations.

3.4.1 $N_{J/\psi}$

This quantity is simply the number of identified J/ψs derived by the real data analysis. The analysis cuts and the fitting procedure was described in previous sections (3.2.9 and 3.3.7).

3.4.2 $A \times \varepsilon^{4\pi}_{J/\psi}$

$A \times \varepsilon^{4\pi}_{J/\psi}$ is the product of the acceptance and efficiency for the muon arms (triggering and reconstruction) as given by realistic detector simulations. It is calculated for each bin by counting the number of J/ψ's which are reconstructed, pass a simulated dimuon trigger, and pass the same cuts as were used in the real data selection, and dividing this by the number of J/ψs generated in this same bin. Both numerator and denominator include a cut on the vertex being within 38 cm of z=0. The resulting efficiencies can be found in tables 3.7 and 3.8 for each bin of interest.

The systematic errors from this section and sections 3.2.4 and 3.2.5 are summarized in table 3.14 and in the next section.

Beam	Arm	Bin	Thrown	Reconstructed	1D1S	2D	$\varepsilon_{perfect}$	$\varepsilon_{\mu\mu}$	ε_{1D1S}	ε_{2D}
pp	S	All	111841	5091	3742	0	0.128	0.356	0.682	0
pp	S	y1	49193	2540	1744	0	0.128	0.403	0.687	0
pp	S	y2	62648	2551	1728	0	0.128	0.318	0.677	0
pp	N	All	126387	10896	9542	0	0.127	0.679	0.876	0
pp	N	y1	73890	6278	5506	0	0.127	0.669	0.877	0
pp	N	y2	52497	4618	4036	0	0.127	0.693	0.874	0
dAu	S	All	111841	7292	6056	3857	0.128	0.509	0.830	0.529
dAu	S	y1	49193	3437	2880	1833	0.128	0.546	0.838	0.533
dAu	S	y2	62648	3855	3176	2024	0.128	0.481	0.824	0.525
dAu	N	All	126387	11123	9734	7321	0.127	0.693	0.875	0.658
dAu	N	y1	73890	6288	5528	4067	0.127	0.670	0.879	0.647
dAu	N	y2	52497	4835	4206	3254	0.127	0.725	0.870	0.673

Table 3.7 Summary of the simulation results used to obtain the J/ψ efficiency for each bin in rapidity. For the South arm All is $-2.2 < y < -1.2$, y1 is $-2 - 2 < y < -1.7$, and y2 is $-1.7 < y < -1.2$. While for the North arm All is $1.2 < y < 2.4$, y1 is $1.2 < y < 1.8$, and y2 is $1.8 < y < 2.4$. 2D is the two-deep road trigger, while 1D1S is the one-deep and one-shallow road trigger.

3.4.3 $B_{\mu\mu}$

The particle data book lists the branching ratio for $J/\psi \to \mu^+\mu^-$ as $B_{\mu\mu} = 0.0588 \pm 0.0010$ [195]. We assign no systematic error due to this number.

3.4.4 N_{MB}

This is the number, integrated over all selected runs, of minimum-bias triggered events, included in the analysis. The luminosity numbers, calculated from the number of sampled events, for the different run periods, were given already in table 3.4.

Systematic errors

The number of background events, such as beam gas and beam scraping, was estimated to be small.

3.4.5 σ_{tot}

The total dAu cross section at $\sqrt{s} = 200\,\text{GeV}$ has not actually been measured. The HIJING value for the inelastic cross-section ($\sigma_{inel} = 2.25 \pm 0.1\,\text{b}$), with a modified description of the deuteron by B. Cole and S. Johnson.

Beam	Arm	Bin	Thrown	Reconstructed	1D1S	2D	$\varepsilon_{perfect}$	$\varepsilon_{\mu\mu}$	ε_{1D1S}	ε_{2D}
pp	S	pt1	32310	1666	1154	0	0.128	0.403	0.693	0
pp	S	pt2	52146	2478	1728	0	0.128	0.371	0.697	0
pp	S	pt3	22370	961	670	0	0.128	0.336	0.697	0
pp	S	pt4	4347	233	166	0	0.128	0.419	0.712	0
pp	N	pt1	36557	3331	2957	0	0.127	0.717	0.888	0
pp	N	pt2	59235	5236	4611	0	0.127	0.696	0.881	0
pp	N	pt3	25303	2090	1878	0	0.127	0.650	0.899	0
pp	N	pt4	4622	441	379	0	0.127	0.751	0.859	0
dAu	S	pt1	32310	2226	1843	1169	0.128	0.538	0.828	0.525
dAu	S	pt2	52146	3421	2828	1788	0.128	0.513	0.827	0.523
dAu	S	pt3	22370	1285	1074	692	0.128	0.449	0.836	0.539
dAu	S	pt4	4347	300	259	171	0.128	0.539	0.863	0.570
dAu	S	pt5	555	49	44	31	0.128	0.690	0.898	0.633
dAu	N	pt1	36557	3358	2938	2193	0.127	0.723	0.875	0.653
dAu	N	pt2	59235	5235	4578	3432	0.127	0.696	0.874	0.656
dAu	N	pt3	25303	2040	1803	1369	0.127	0.635	0.884	0.671
dAu	N	pt4	4622	427	364	291	0.127	0.727	0.852	0.681
dAu	N	pt5	569	52	42	31	0.127	0.720	0.808	0.596

Table 3.8 Summary of the simulation results used to obtain the J/ψ efficiency for each bin in p_T. The bins are $0 < p_T < 1$ (pt1), $1 < p_T < 2$ (pt2), $2 < p_T < 3$ (pt3), $3 < pT < 4$ (pt4), and $4 < p_T < 5$ (pt5). 2D is the two-deep road trigger, while 1D1S is the one-deep and one-shallow road trigger.

Some description of this and a Glauber calculation for dAu can be found in the Appendix C. The 'PHENIX standard' Glauber calculation result is 2.18 ± 0.08 b [197]. This is the value used in the calculation of ε_{BBC}^{MB} and $\varepsilon_{BBC}^{J/\psi}$ in the next two sections. See the next section for a description of the error on this quantity. The total pp cross section, based on an average of the available world data, is 42.2 ± 1.9 mb [199].

The estimated systematic error is thus about 4.5% for each of these numbers.

3.4.6 $\varepsilon_{BBC}^{J/\psi}$

$\varepsilon_{BBC}^{J/\psi}$ is the BBC trigger efficiency for J/ψ events which have a vertex that falls within a $|z| < 30$ cm. This was calculated by Monte Carlo simulations, and cross-checked with real data for the Run 2 pp analysis, and found to be 0.74 ± 0.01 (stat. only). Within systematic errors, a good agreement between the values for J/ψ's in the central and muon arms, as well as for high p_T pions in the central arms were found. This lead to the sugges-

tion that the BBC trigger efficiency for hard processes could be process independent [166].

3.4.7 ε_{BBC}^{MB}

ε_{BBC}^{MB} is the fraction of inelastic collisions that occur within X cm of $z = 0$ which will fire the minimum bias trigger (BBCLL1(> 1)) and which have their offline BBC $|z_{vtx}|$ reconstructed within 30 cm of $z = 0$. ε_{BBC}^{MB} was estimated to be about 0.885 for dAu [194] using a parametrization of BBC response, and 0.88 ± 0.04 from simulations [198] and other studies. The pp cross section, as seen by the BBC has been measured, and found to be 21.8 mb $\pm$ 9.6% [199] , and the eff. of the BBC found to be $0.516 \pm 9.8\%$. [199]

3.5 Centrality Selections

In this section, we address the way we divide the data sample in bins of centrality in order to compute the ratio of central to peripheral events (Rcp) and the ratio of the various deuteron+gold centrality classes to the proton proton data (Rda)

The centrality selections are identical to those used in the Appendix C. These selections are $0-20\%$, $20-40\%$, $40-60\%$, and $60-88\%$ centrality.

All assumptions made in the Appendix C are also assumed here. We repeat these assumptions for completeness. These include:

1. BBC South hit multiplicity is $\approx$ the number of Au participants. In d-Au collisions, ${}^{Au}N_{part} \approx N_{coll}$.

2. BBC South hit multiplicity can be described by the Negative Binomial Distribution.

3. Assuming uncorrelated hits in the BBC South, the parameters in the negative binomial distribution are proportional to the number of Au participants.

4. A Glauber model calculation can be used to determine the number of collisions, N_{coll}.

For each centrality class, there is a centrality bias caused by the neutral pion $p_T \geq 1.5$ GeV trigger. Of the minimum bias events, there is some fraction of events for which this high p_T trigger is satisfied. This correction is calculated based on negative binomial distribution fits to the N_{coll} distributions in each class. The results from the Appendix C are included below for completeness in Table 3.9.

Centrality bin	Value	Error
0-20	1.000	0.0008
20-40	0.995	0.003
40-60	0.974	0.01
60-88	0.885	0.04

Table 3.9 BBC centrality bias correction factor table.

As the muon trigger is also a high p_T trigger, we apply the same corrections to our sample in the centrality results reported here. Eventually, we should determine our own corrections based on muons detected in the muon arms as the high p_T trigger assumes a neutral pion detected in the central arms. In the notation of equation 3.2, this correction basically replaces the $\varepsilon_{BBC}^{J/\psi}/\varepsilon_{BBC}^{MB}$ ratio taken on minimum bias sample. One should note that the weighted average of the correction across centrality bins is equivalent to the minimum bias correction: $(0.2. + 0.2 \times 0.995 + 0.2 \times 0.974 + 0.28 \times 0.885)/0.88 \sim 0.96$.

The vertex range as used in Appendix C is ± 18 cm and no vertex dependence was found. At the time of this analysis, the BBC centrality was extended to the range ± 40 cm and is consistent with the ± 38 cm range used here.

For the neutron-tagged sample (the proton undergoes collisions with the Au nucleus), the average trigger efficiency is 16.8%. The same selection criteria for neutron-tagged events as used in Appendix C are also used here (namely, requiring at least an energy of 60 GeV in the North ZDC).

A Monte Carlo Glauber model calculation that includes the BBC response was used in Appendix C to determine the number of collisions for

the centrality selections. These values are summarized in Table 3.10 for completeness.

Centrality bin	$\langle N_{coll} \rangle$	Systematic Error	$\langle N_{coll} \rangle / \langle N_{coll}^{60-88} \rangle$	Systematic Error
0-20	15.0±1.0	6.6%	4.6±0.5	10.2%
20-40	10.4±0.7	6.9%	3.2±0.2	7.7%
40-60	6.9±0.6	8.5%	2.1±0.1	4.0%
60-88	3.2±0.3	9.7%	1.0±0.0	0.0%
Min Bias	8.4±0.7	(included)	–	–

Table 3.10 The N_{coll} and errors as determined using Glauber MC and the BBC response (from Appendix C).

In order to compare to theory, this same Glauber MC code is used to determine the N_{coll} for a given impact parameter range. For the ranges used in our centrality comparison to theory, these values are in Table 3.11.

Impact Parameter	N_{coll}
$0.2 < b/R$	16.9
$0.9 < b/R < 1.1$	3.5
$1.9 < b/R < 2.1$	1.3

Table 3.11 The N_{coll} using the MC Glauber calculation for a given impact parameter range (ranges as used in the paper by Klein and Vogt [65]).

The point-to-point systematic errors include those errors in both Rcp and Rda that vary in a correlated way to $\langle N_{coll} \rangle$. The BBC bias (see table 3.9) and the N_{coll} errors (see table 3.10) are the ones to be considered has point-to-point.

The errors that are independent of $\langle N_{coll} \rangle$ are considered separately. The only centrality-related uncertainty to be considered as global is when we derive the minimum bias Rda. We then need $\langle N_{coll}^{MB} \rangle$. Table 3.10 tells us that this error is $0.7/8.4 = 8.3\%$.

3.6 Summary of systematic errors

3.6.1 Analysis related systematics

- **Tube efficiency (including BLT)** - using the difference between random benefit corrected and non-random benefit corrected tube efficiencies, an average difference in tube efficiencies of approximately 0.5% gives approximately a 3% difference in J/ψ efficiency results. For the tube efficiencies, Sean estimates a systematic of -1.5% and $+1\%$. This then scales to about -9% and $+6\%$ in the J/ψ efficiency. For the ratio we assume that part of this cancels and use 1/2 this amount as shown in table 3.12.

beam or ratio	arm	systematic
pp	S	$-9, +6\%$
	N	$-9, +6\%$
dAu	S	$-9, +6\%$
	N	$-9, +6\%$
R(dAu/pp)	S	$-4.5, +3\%$
	N	$-4.5, +3\%$

Table 3.12 Estimated systematic uncertainties associated with determination of the muon identification tube efficiencies.

- **Muon tracker efficiency** - The agreement discussed in the muon tracking efficiency section earlier is close to being the same between MC and data within the statistical errors.

- **Attenuated strips** - The effect of north attenuated strips on efficiency is obtained from simulations. We take an asymmetric systematic of 5% towards larger cross section (for north only) and assume this probably cancels in a ratio of dAu/pp.

- **Fitting method** - Uncertainty due to model dependence of fitting functions and procedures. See fitting dimuon spectra section and table 3.6.

- **Double counting (ghosts)** - The number of events with more than one dimuon contributing to the J/ψ mass region has been counted (see table 3.13). They should be ghosts. For now we keep them but assign a 1.5% asymmetric systematic towards smaller cross section and smaller ratio.

beam	arm	trigger	$\mu^{\pm}\mu^{\pm}$	$\mu^{+}\mu^{-}$
pp	S	1d1s	0	0
	N	1d1s	1.3%	0.3%
dAu	S	1d1s	0.8%	1.5%
	S	2d	0.9%	0.6%
	N	1d1s	0.3%	0
	N	2d	2.6%	0.9%

Table 3.13 Upper limits for different beams, arms and triggers on the number of possible ghost pairs contributing to the J/ψ yield.

- **Combinatoric background method** - We assign a 5% systematic uncertainty, as it was described in section 3.3.7.
- **Trigger Circuit Efficiency** - negligible (the correction itself is very small, 5% or less).
- **Event mixing/embedding** - So far, no statistically significant evidence for a net non-zero effect here. Present results are statistics limited at the 3% level, so we assign a 3% systematic (see table 3.5).
- **MuTr HV state variations** (run2 3%) - - a systematic of 3%.
- **MC representation** - MC versus data distributions - use same as run 2, 5%.
- **Rapidity distribution** - use same as run 2, 3%.

  A summary of all the systematic uncertainties is in Table 3.14.

Systematic error	pp South	pp North	dAu South	dAu North	Ratio South	Ratio North
Fitting	$\pm 7.1\%$	$\pm 4.7\%$	$\pm 10.3\%$	$\pm 11.9\%$	$\pm 3.7\%$	$\pm 2.8\%$
Ghosts	-1.5%	-1.5%	-1.5%	-1.5%	-1.5%	-1.5%
Combinatorial Background	$\pm 5\%$	$\pm 5\%$	$\pm 5\%$	$\pm 5\%$	$\pm 5\%$	$\pm 5\%$
Point-to-point	$+8.7\%$ -8.8%	$+6.9\%$ -7.0%	$+11.4\%$ -11.5%	$+12.9\%$ -13.0%	$+6.4\%$ -6.4%	$+5.9\%$ -5.9%
MuID Tube Efficiency	$+6-9\%$	$+6-9\%$	$+6-9\%$	$+6-9\%$	$+3-6\%$	$+3-6\%$
MuTr Chamber Efficiency	$+6.5\%$	$+9.5\%$	$+6.5\%$	$+9.5\%$	$+3.3\%$	$+4.8\%$
MuTr Attenuated Strips	0.0%	$\pm 5\%$	0.0%	$\pm 5\%$	0.0%	$\pm 5\%$
Event Mixing Error	$\pm 3\%$	$\pm 3\%$	$\pm 3\%$	$\pm 3\%$	$\pm 3\%$	$\pm 3\%$
MuTr HV state	$\pm 3\%$	$\pm 3\%$	$\pm 3\%$	$\pm 3\%$	$\pm 3\%$	$\pm 3\%$
Arm-to-Arm	$+9.8\%$ -9.9%	$+13.0\%$ -11.1%	$+9.8\%$ -9.9%	$+13.0\%$ -11.1%	$+6.2\%$ -8.1%	$+8.7\%$ -10.1%
MuTr MC Represent.	$\pm 5\%$	$\pm 5\%$	$\pm 5\%$	$\pm 5\%$	0.0%	0.0%
Rapidity Distribution.	$\pm 3\%$	$\pm 3\%$	$\pm 3\%$	$\pm 3\%$	0.0%	0.0%
Global	$+5.8\%$ -5.8%	$+5.8\%$ -5.8%	$+5.8\%$ -5.8%	$+5.8\%$ -5.8%	0.0% 0.0%	0.0% 0.0%
SUM	$+14.3\%$ -14.5%	$+15.8\%$ -14.4%	$+16.2\%$ -16.3%	$+19.2\%$ -18.1%	$+8.9\%$ -10.3%	$+10.5\%$ -11.7%

Table 3.14 Summary of systematic errors. All errors listed are fractional errors in %. Top box are for errors to be applied independently to each point. In the middle box, are errors which depend on the arm we consider but should be the same for all points within this arm. The bottom box is for errors that are independent of any selection.

3.6.2 Absolute normalization systematics summary

- Overall abs. norm systematics: pp 12%, dAu 6% (quadrature sum of below contributions). Summarized in table 3.16.
- N_{MB} - background events negligible
- σ_{tot} - pp 42.2(1.9) mb; dAu 2.81(0.08).
- ε_{BBC}^{MB} - pp 0.516(9.8%) ; dAu 0.88(0.04)
- The product $\sigma_{tot} \times \varepsilon_{BBC}^{MB}$ is estimated to suffer a 9.6 % systematic errors.
- $\varepsilon_{BBC}^{J/\psi}$ - pp 0.74(5%) ; dAu 0.92(2%)

  Nominally ε_{BBC}^{MB} above are valid for ± 30 cm, but these efficiencies are not significantly z_{vtx} dependent in the range ± 38 cm . Also the efficiencies for two z_{vtx} ranges are equal within uncertainties. See Table 3.15.

z_{vtx}	N_{Tag}	π^0	minBias
$\pm 20cm$	72.8%	94.8%	87.5%
$\pm 30cm$	73%	94.8%	87.2%

Table 3.15 BBC efficiencies which show negligible differences between vertex ranges of $\pm 30cm$ and $\pm 20cm$.

Beam	Arm	Quantity	Value	Uncertainty
pp	S	N_{MB}	4.50×10^9	0
pp	N	N_{MB}	4.02×10^9	0
pp		ε_{BBC}^{MB}	0.516	9.8%
pp		σ_{pp}^{tot}	42.2 mb	1.9 mb
pp		$\varepsilon_{BBC}^{MB} \times \sigma_{pp}^{tot}$		9.6 %
pp		$\varepsilon_{BBC}^{J/\psi}$	0.74	5%
total				10.8 %
global			+ 5.8% =	12.3 %
dAu	S	N_{MB}	2.70×10^9	0
dAu	N	N_{MB}	3.31×10^9	0
dAu		ε_{BBC}^{MB}	0.88	0.04
dAu		σ_{dAu}^{tot}	2.18 b	0.08 b
dAu		$\varepsilon_{BBC}^{J/\psi}$	0.92	2%
total				6.2 %
global			+ 5.8% =	8.5 %

Table 3.16 Summary of common normalization factors used in the cross section calculations and their systematic uncertainties. "total" stands for the quadratic sum of these errors, while global add the other "global" uncertainties from table 3.14.

Chapter 4

Results and Discussions

4.1 J/ψ cross section in p+p : Run-II

Understanding J/ψ production mechanisms requires data over a large range of collision energies and with broad coverage in rapidity and transverse momentum (p_T). Existing data at lower energies from fixed target hadron experiments yield total cross sections and mean p_T ($\langle p_T \rangle$) values in the energy range $\sqrt{s} = 7$ - 38.8 GeV [158]. Limited kinematic coverage in collider experiments [158–160] has so far meant that total cross sections and mean p_T values could not be measured. The systematic study of J/ψ production at Relativistic Heavy Ion Collider (RHIC) energies with wide p_T and rapidity coverage should therefore provide crucial tests of J/ψ production models. In addition, the RHIC proton-proton results provide a baseline for studying cold and hot nuclear matter in proton-nucleus and nucleus-nucleus collisions using J/ψ yields as a probe.

Intense theoretical interest in the J/ψ production mechanism was stimulated when the Color Singlet Model (CSM) was found [161] to dramatically underpredict the high p_T CDF prompt J/ψ and $\psi(2S)$ cross sections [160]. Attention turned toward models in which color octet $c\bar{c}$ states can also contribute to the J/ψ yield. The Color Octet Model (COM), which is based on the Non-Relativistic QCD model [162], has been successful in reproducing the high p_T CDF prompt J/ψ cross sections, as has the more phenomenological Color Evaporation Model [163].

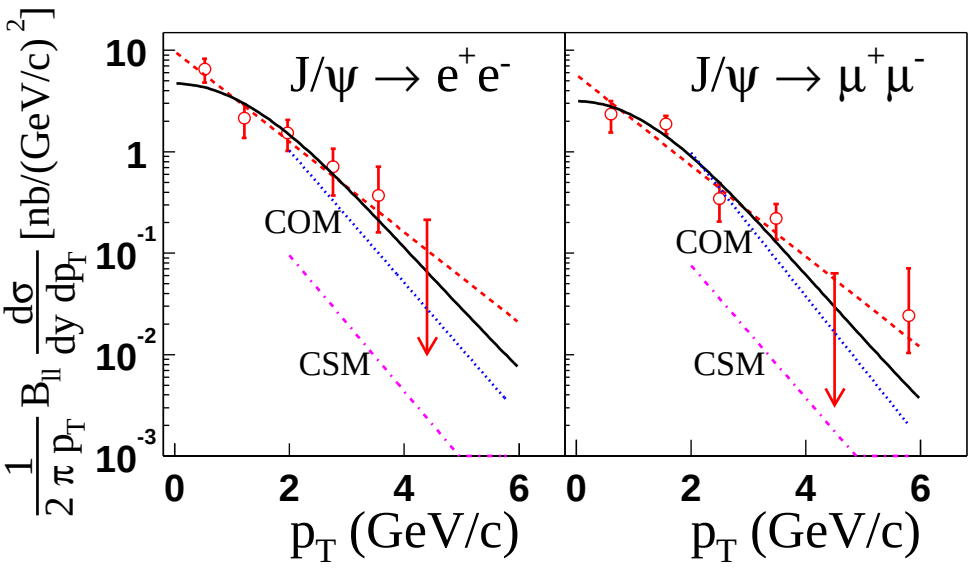

Figure 4.1 The J/ψ p_T distributions for the dielectron and dimuon measurements, with statistical uncertainties. The solid line is a phenomenological fit of the form $1/(2\pi p_T)\ d\sigma/dp_T\ =\ A\ (1+(p_T/B)^2)^{-6}$. The dashed line is an exponential fit. The CSM (dot-dashed) and COM (dotted) calculations are from [172].

The data yield the first total cross sections for J/ψ production beyond fixed target energies, and the first measurement of $\langle p_T \rangle$ beyond $\sqrt{s} = 63$ GeV. They will constrain models in the lower p_T region where gluon fusion is expected to dominate (at p_T beyond about 5 GeV/c, the direct J/ψ production cross section is expected to be dominated by fragmentation of high p_T gluons [164]).

The data were recorded during the 2001/2002 pp run at $\sqrt{s} = 200$ GeV. After quality assurance and vertex cuts ($\pm$ 35 cm for ee and $\pm$ 38 cm for $\mu\mu$), 67 nb^{-1} were used for the $J/\psi \to \mu^+\mu^-$ analysis, and 82 nb^{-1} for $J/\psi \to e^+e^-$.

The p_T distributions for $J/\psi \to e^+e^-$ and $J/\psi \to \mu^+\mu^-$ are shown in Fig. 4.1, with predictions [172] from the COM. Predictions of the CSM,

which greatly underpredicts the cross sections, are also shown. These predictions are limited to $p_T > 2$ GeV/c because parton intrinsic transverse momentum (k_T) broadening is not accounted properly in the calculation. The COM calculations do not include fragmentation contributions, which become important at around 5 GeV/c [160]. Calculations covering all p_T and including fragmentation contributions are needed. The solid lines are a phenomenological fit of a form that has been shown to fit J/ψ data well at fixed target energies [173]. The dashed line is an exponential fit. The phenomenological fits yield $\langle p_T \rangle$ values of 1.85 ± 0.46(stat) $\pm$ 0.16(sys) GeV/c (central arm) and 1.78 ± 0.27(stat) $\pm$ 0.16(sys) GeV/c (muon arm), with a combined value of 1.80 ± 0.23(stat) $\pm$ 0.16(sys) GeV/c. The systematic uncertainties were estimated from the spread in $\langle p_T \rangle$ from a weighted mean of the binned data, the phenomenological fit, and the exponential fit. An additional 3% was assigned to the muon $\langle p_T \rangle$ due to the uncertainty in momentum scale.

The J/ψ rapidity distribution obtained by combining the dielectron and dimuon measurements is shown in Fig. 4.2, with the muon arm data divided into two rapidity bins. The COM curves are theoretical shape predictions [166] using the same models as are discussed in connection with Fig. 4.4b, except that they are normalized to our data to make the shape comparison clearer. Since gluon fusion is the dominant process in all of the models, the rapidity shape depends mostly on the gluon distribution function and is not very sensitive to the production model. Most of the available PDFs are consistent with the data, and improved statistical precision will be needed to constrain them. A PYTHIA calculation that reproduces the shape of our data best is also shown in Fig. 4.2. Normalizing this to the data, the total cross section was determined to be 3.99 ± 0.61(stat) $\pm$ 0.58(sys) $\pm$ 0.40(abs) μb. The quoted systematic error of 14% was estimated by setting the measured cross sections all to their upper systematic error limits or all to their lower systematic error limits and noting how the cross section changed. The variation in the total cross section extracted if we use the same procedure with different PDF choices and models was estimated to be small (3%).

A comparison is made in Fig. 4.4a of the present $\langle p_T \rangle$ value with values from previous experiments [158]. There are no theoretical predictions that

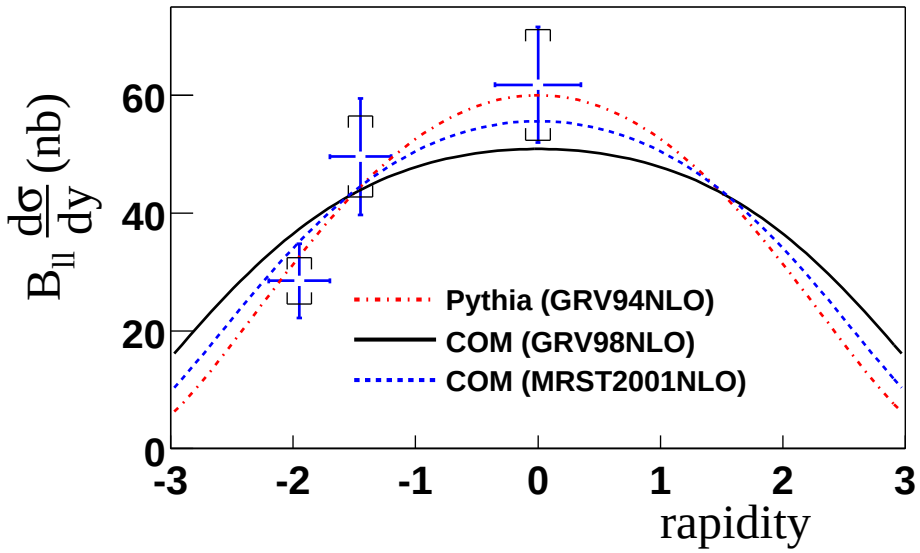

Figure 4.2 The central rapidity point is from $J/\psi \to e^+e^-$, the others from $J/\psi \to \mu^+\mu^-$. The brackets represent systematic uncertainties. All curves have their overall normalization fitted to the data. The PYTHIA shape was used to determine the cross section. There is an overall 10% absolute normalization error not shown.

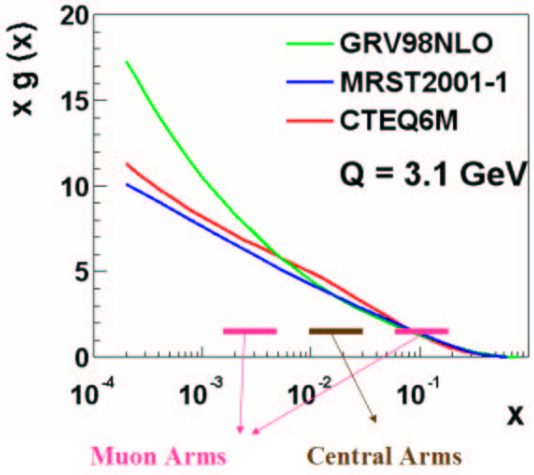

Figure 4.3 Gluon distribution function is shown in PHENIX acceptance, used in the models which is shown in Fig 4.2

we can compare with the $\langle p_T \rangle$ measurements. The total J/ψ cross section determined in this analysis is shown in Fig. 4.4b, along with cross sections determined by lower energy experiments [158] and predictions from the COM [166] using two different PDFs. The $\sqrt{s}$ dependence of the cross section is sensitive to the factorization scale Q, since the shape of the PDFs depend on Q. The values of Q (3.1 GeV for GRV98NLO and 2.3 GeV for MRST2001NLO) were chosen to give good agreement with the data. The total cross section normalization was obtained using color octet matrix elements from [174], but has large theoretical uncertainties associated with the charm quark mass and the renormalization scale. The renormalization scale was taken to be equal to the quark mass M_c, and their values (1.48 GeV for GRV98NLO and 1.55 GeV for MRST2001NLO) were chosen to give good agreement with the data. The CEM is also able to describe the total cross section data [163]. All measurements and models include feed-down from the χ_c and the ψ' to the J/ψ. We estimate [175] that B decay feed-down contributes less than 4% to the J/ψ total cross section at $\sqrt{s} =$ 200 GeV.

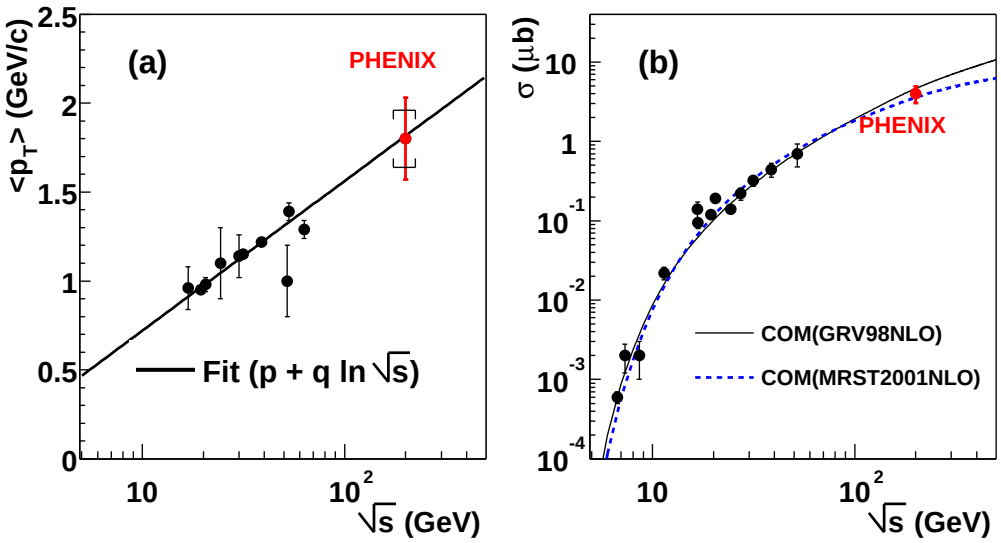

Figure 4.4 (a) The present J/ψ mean p_T value compared with previous measurements at lower energy. The linear fit parameters are $p = 0.53$, $q = 0.19$. (b) The present J/ψ total cross section compared with previous measurements at other values of $\sqrt{s}$. The curves are discussed in the text.

4.2 J/ψ cross section in p+p : Run-III

The first $pp \to J/\psi + X$ measurements from RHIC was obtained at $\sqrt{s} =$ 200 GeV with run II data [166] and gave a baseline of our analysis which was discussed in section4.1 in more details. The new run-III data analysis has been done with the improved RHIC luminosity(table 2.2), muon tracker acceptance improvement and more precise Muid efficiency calculation and gives the consistent results within the statistical and systematic errors compared with the run-II results and is used to study the nuclear modification factor in d+Au collision. The detail description of analysis method and efficiency is discussed in the section3.3.

On figure 4.5, the measured differential cross section times branching ratio as a function of rapidity in p+p collision by using run-III data set is shown. The dielectron measurement is shown as a single point at mid-rapidity. The data from each dimuon spectrometer has been split in two rapidity bins. Solid error bars represent statistical and point-to-point systematic uncertainties. The dashed error bars stand for the systematic uncertainties common to one spectrometer. An additional 12.3% global error bar is not shown.

A fit to a shape generated with PYTHIA using the GRV94HO parton distribution is performed and gives a total cross section, multiplied by the dilepton branching ratio of 5.9%, equal to:

$$\mathrm{BR} \times \sigma_{pp}^{J/\psi} = 159 \text{ nb} \pm 8.5\%(\text{fit}) \pm 12.3\%(\text{abs}) \tag{4.1}$$

where the first uncertainty comes from the fit and thus includes both the statistical and point-to-point systematics. The second uncertainty accounts for absolute systematic errors. Variations in the parton distribution functions used to determine the shape were demonstrated to be less than 3% [156] and were neglected here.

4.3 J/ψ production in deuteron+gold

In d+Au collisions at 200 GeV, J/ψ 's in the three rapidity ranges probe momentum fractions x of gluons in the gold nucleus (neglecting the emitted gluon) of: 0.05 to 0.14 (backward, negative rapidity, gold-going side),

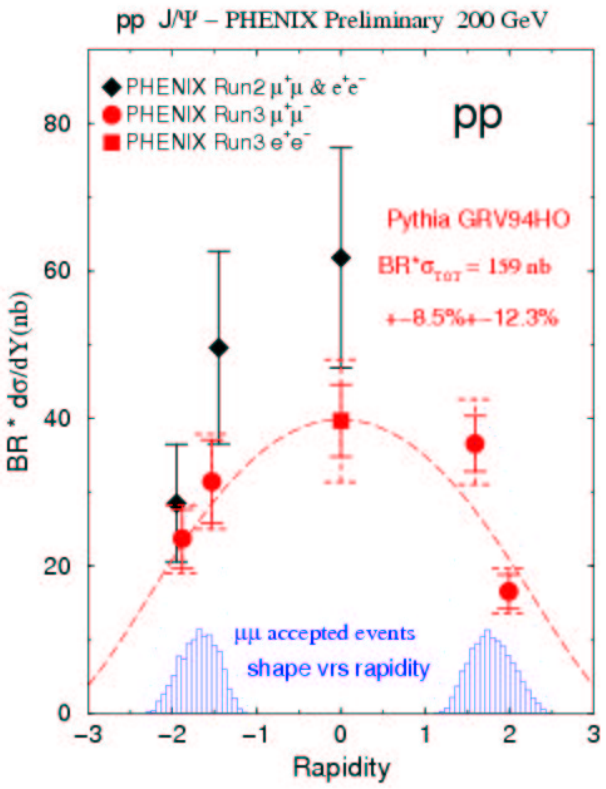

Figure 4.5 J/ψ differential cross section times dilepton branching ratio versus rapidity in p+p collision.

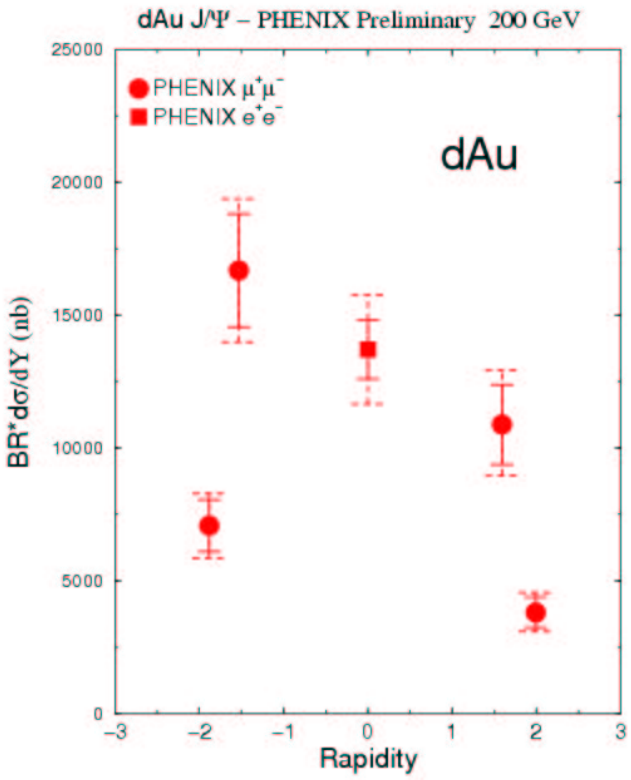

Figure 4.6 J/ψ differential cross section times dilepton branching ratio versus rapidity in d+A collision.

0.011 to 0.022 (midrapidity) and 0.0014 to 0.0047 (forward, positive rapidity, deuteron-going side). The detail kinematic distribution for PHENIX central and muon arm is shown in the Fig. 2.4.

4.3.1 Rapidity dependence

On figure 4.6, the measured differential cross section times branching ratio versus rapidity in d+Au collision is shown. The ratio between the J/ψ yields observed in d+Au collisions and p+p collisions, divided by 2×197 is shown on figure 4.7. Solid error bars represent statistical and point-to-point systematic uncertainties. The dashed error bars represent the systematic uncertainties common to one spectrometer. An additional 13.4% global error bar is not shown.

While this ratio is close to unity at backward rapidity, it is significantly lower at forward rapidity, where parton distribution are expected to be shadowed in a heavy nucleus. Theoretical predictions from Vogt [19] and Kopeliovich [20] are displayed on the figure for comparison.

4.3.2 Transverse momentum dependence

Figures 4.9 show the differential cross sections versus transverse momentum for both pp and dAu, according to equation 3.2. All the relevant numbers are reported in table 4.1.

The J/ψ p_T distributions $(d^2\sigma/dydp_T)/(2\pi p_T)$ have been fitted to the traditional $(A(1+(p_T/B)^2)^{-6}$ function. The average p_T^2 resulting from the fit is 4.47 ± 0.25 and 3.99 ± 0.25 $(GeV/c)^2$ for d+Au collisions at backward and forward rapidity, respectively, to be compared with 2.70 ± 0.24 for p+p collisions.

Figure 4.10 shows the α parameter defined as $\sigma_{dA} = \sigma_{pp} \times (2A)^{\alpha}$. Solid error bars represent statistical and point-to-point systematic uncertainties. An additional 2.2% global error bar is not shown. Results from the $\sqrt{s_{NN}} = 38$ GeV lower energy experiment E866/NuSea [18] are displayed for comparison. The observed p_T broadening is comparable for the two energies.

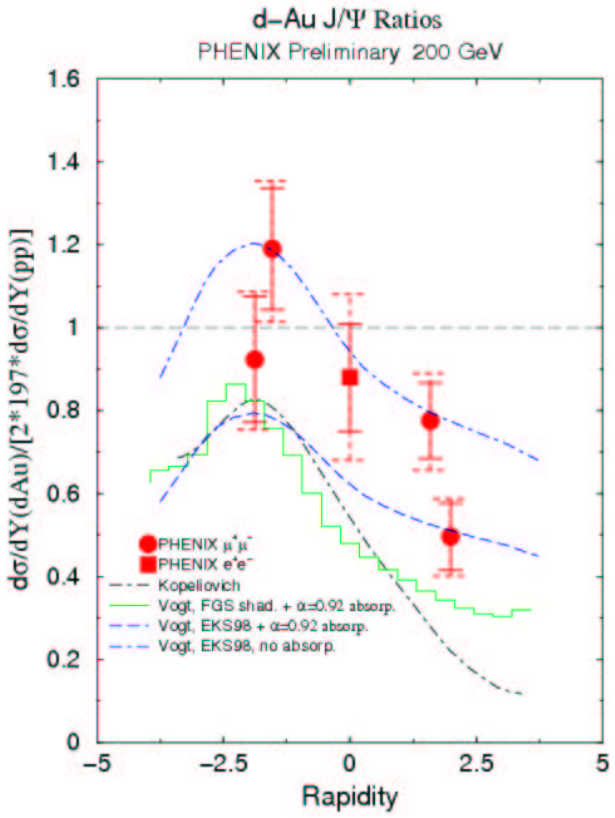

Figure 4.7 Ratio between d+Au and p+p J/ψ differential cross sections, divided by 2×197, versus rapidity.

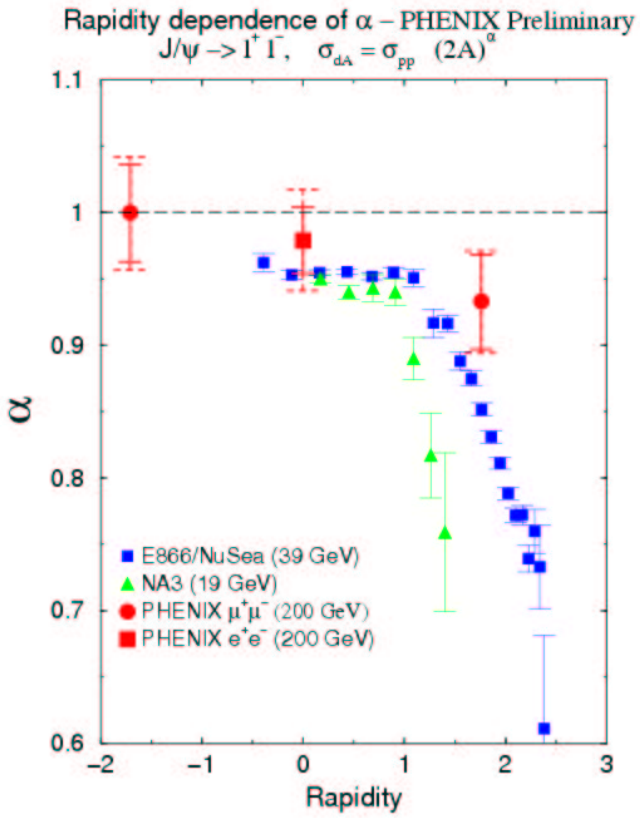

Figure 4.8 α parameter(defined as $\sigma_{dA} = \sigma_{pp} \times (2A)^{\alpha}$) versus rapidity

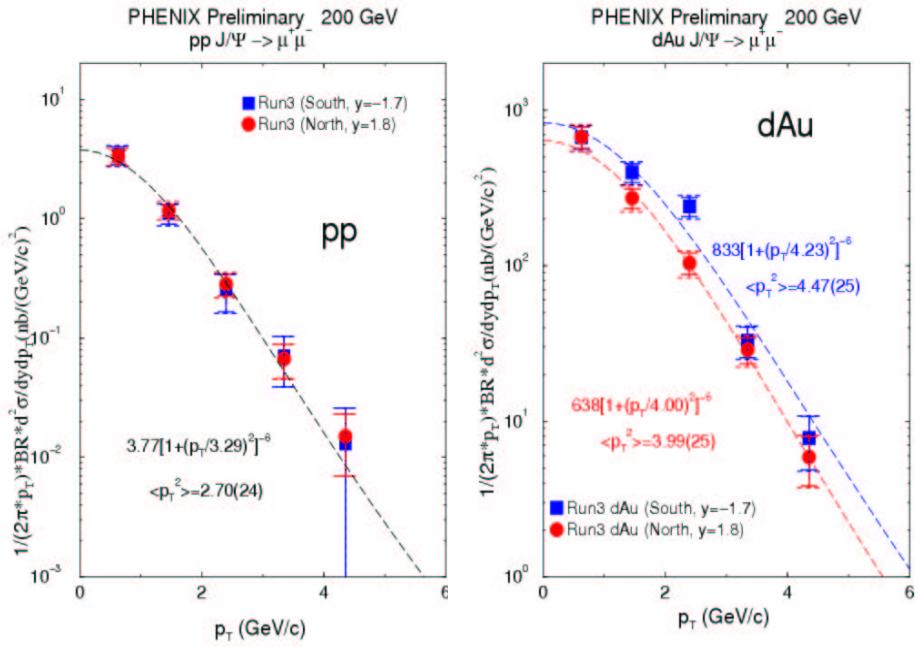

Figure 4.9 Invariant cross section for pp versus transverse momentum. Solid error bars represent statistical + point-to-point systematics and the dashed error bars include arm-to-arm errors. A global 12.3 % error bar is not displayed (see tables 3.14 and 3.16). Results from the 2002 run are shown in black for comparison.

p_T	$\#J/\psi$	ϵ_{perf}	$\epsilon_{\mu\mu}$	ϵ_{BLT}	ϵ_{TCE}	L (nb^{-1})	$\epsilon_{BBC}^{J/\psi}$	$BR \times d\sigma_{J/\psi}$ (nb)
dAu:	South							
0.63	126(14)	0.128	0.515	0.696	0.99	1.43	0.92	669(76)
1.46	214(16)	0.128	0.487	0.699	0.99	1.43	0.92	399(31)
2.40	193(14)	0.128	0.43	0.709	0.99	1.43	0.92	241.2(19.3)
3.35	46(8)	0.128	0.505	0.75	0.99	1.43	0.92	33.05(6.19)
4.35	19(6)	0.128	0.676	0.764	0.99	1.43	0.92	7.786(2.778)
dAu:	North							
0.63	253(21)	0.127	0.699	0.77	0.93	1.70	0.92	674(58)
1.46	297(18)	0.127	0.674	0.773	0.93	1.70	0.92	273(17)
2.40	175(14)	0.127	0.617	0.784	0.93	1.70	0.92	103.8(8.7)
3.35	77(10)	0.127	0.71	0.771	0.93	1.70	0.92	28.83(4.09)
4.35	18(5)	0.127	0.706	0.69	0.93	1.70	0.92	5.891(1.922)
pp:	South							
0.63	48(7)	0.128	0.348	0.658	0.99	208	0.74	3.420(511)
1.46	43(7)	0.128	0.324	0.654	0.99	208	0.74	1.103(182)
2.40	15(5)	0.128	0.293	0.659	0.99	208	0.74	0.253(085)
3.35	7(3)	0.128	0.359	0.64	0.99	208	0.74	0.071(031)
4.35	2(2)	0.128	0.465	0.606	0.99	208	0.74	0.013(013)
pp:	North							
0.63	121(12)	0.127	0.675	0.86	0.95	185	0.74	3.354(339)
1.46	124(12)	0.127	0.655	0.862	0.95	185	0.74	1.178(115)
2.40	47(9)	0.127	0.614	0.87	0.95	185	0.74	0.283(055)
3.35	17(5)	0.127	0.693	0.843	0.95	185	0.74	0.067(020)
4.35	4(2)	0.127	0.623	0.778	0.95	185	0.74	0.015(008)
pp:	Mean							
0.63								3.374(393)
1.46								1.158(133)
2.40								0.276(062)
3.35								0.068(024)
4.35								0.014(009)

Table 4.1 Calculation of the cross sections and ratios versus p_T for the two muon arms. The pp average cross section used to form the ratios assuming symmetry around y=0 is shown at the bottom. The quantities in the third and fourth columns are from 3.8, ε_{BLT} is the luminosity weighted average of the 1D1S and 2D trigger efficiencies, and L is the total luminosity for both triggers. The differential cross section shown is $1/(2\pi p_T) * BR * d^2\sigma/dydp_T$ in $nb/(GeV/c)^2$.

4.3.3 Centrality dependence

Figure 4.12 shows the ratio of the dAu cross sections between more central and the most peripheral centrality bin, while 4.11 shows the dependence on centrality of the dAu/pp ratio.

The dAu/pp ratio is computed from the quantities reported in table 4.2 with Equation 4.2:

$$\mathcal{R}(N_{coll}) = \frac{d\sigma^{J/\psi}_{dAu}/dY}{AB \times d\sigma^{J\psi}_{pp}/dY} \Big/ \frac{N_{coll} \times \sum width}{N^{MB}_{coll} \times width} \tag{4.2}$$

where

1. $AB = (2)(197)$ is the total number of nucleons in the dAu collision system,

2. N^{MB}_{coll} is the number of collisions in minimum bias events 8.4 ± 0.7 from table 3.10,

3. Σwidth $= 0.88$ is the total sum of the centrality bin widths, while *width* is the width of the centrality bin (0.20 or 0.28). This is to normalized to the correct partial luminosity.

4. The $d\sigma^{J/\psi}_{dAu}/dY$ computation is done as in equation 3.2, the ratio of BBC efficiencies being the *bias* number from table 3.9.

Again, this is not the usual PHENIX standard, but it can simply be obtained by $R_{dAu} = (0.91 \pm 0.09)\mathcal{R}$. The right axis stands for it on figure 4.11.

The Rcp is also tabulated and is determined using Equation 4.3,

$$R_{cp} = \frac{N_{J/\psi}/N_{coll}}{N^{60-88\%}_{J/\psi}/N^{60-88\%}_{coll}} \tag{4.3}$$

For d+Au collisions, the centrality was measured by counting the charge deposited in the beam-beam counter towards which the gold beam points. Centrality is then related to the average number of nucleon+nucleon collisions $< N_{coll} >$ through a Glauber computation. The ratio R_{dA} of J/ψ

Bin	N_{coll}	$N_{J/\psi}$	Width	Bias	L (nb^{-1})	$BR * d\sigma_{J/\psi}$ (nb)
dAu:	South					
MB	8.4	578(27)	1	1	1.43	10.48(49)
0-20%	15	288(20)	0.2	1	1.43	26.11(1.81)
20-40%	10.4	168(14)	0.2	0.995	1.43	15.31(1.28)
40-60%	6.9	81(11)	0.2	0.974	1.43	7.540(1.024)
60-88%	3.2	50(9)	0.28	0.885	1.43	3.659(659)
NTag	3.6	58(8)	0.168		1.43	6.260(863)
dAu:	North					
MB	8.4	784(31)	1	1	1.70	7.012(277)
0-20%	15	287(19)	0.2	1	1.70	12.834(850)
20-40%	10.4	241(17)	0.2	0.995	1.70	10.831(764)
40-60%	6.9	146(14)	0.2	0.974	1.70	6.703(643)
40-60%	6.9	81(11)	0.2	0.974	1.43	7.540(1.024)
60-88%	3.2	50(9)	0.28	0.885	1.43	3.659(659)
NTag	3.6	58(8)	0.168		1.43	6.260(863)
dAu:	North					
MB	8.4	784(31)	1	1	1.70	7.012(277)
0-20%	15	287(19)	0.2	1	1.70	12.834(850)
20-40%	10.4	241(17)	0.2	0.995	1.70	10.831(764)
40-60%	6.9	146(14)	0.2	0.974	1.70	6.703(643)
60-88%	3.2	117(12)	0.28	0.885	1.70	4.223(433)
NTag	3.6	80(10)	0.168		1.70	0.949(119)
pp:	South					
		118(12)			208	0.734(184)
pp:	North					
		290(19)			185	0.677(161)
pp:	Mean					
						0.692(163)

Table 4.2 Calculation of the cross sections and ratios versus centrality for the two muon arms using Equation 4.2. The pp average cross section used to form the ratios assuming symmetry around y=0 is shown at the bottom.

yields in d+Au and p+p normalized by the $< N_{coll} >$ is shown on figure 4.11, for four centrality classes corresponding to $< N_{coll} >= 3.2 \pm 0.3$, 6.9 ± 0.6, 10.4 ± 0.7 and 15.0 ± 1.0, and for minimum bias collisions corresponding to an average value of N_{coll} equal to 8.4 ± 0.7. Solid error bars represent statistical and point-to-point systematics and the dashed error bars are common to one spectrometer. An additional 13.4% global error bar is not shown.

At forward rapidity (small x values in the gold nucleus, or the shadowing region), no strong dependence is observed, while a strong enhancement from peripheral to central collisions is observed at backward rapidity. The theoretical curves on figure 4.11 correspond to different amounts of inhomogeneous shadowing and antishadowing at these rapidities from [19]. The predictions are qualitatively consistent with the data at forward rapidity, while they do not show the observed steep rising shape at backward rapidity. For now, there is no interpretation to this unexpected behavior, but speculate that it is related to the fact that these J/ψ 's are closer to the gold nucleus rest frame. It might be a evidence in favor of Color Glass Condensate(whose theoretical overview with some experimental results is discussed in section1.3) in our backward rapidity region.

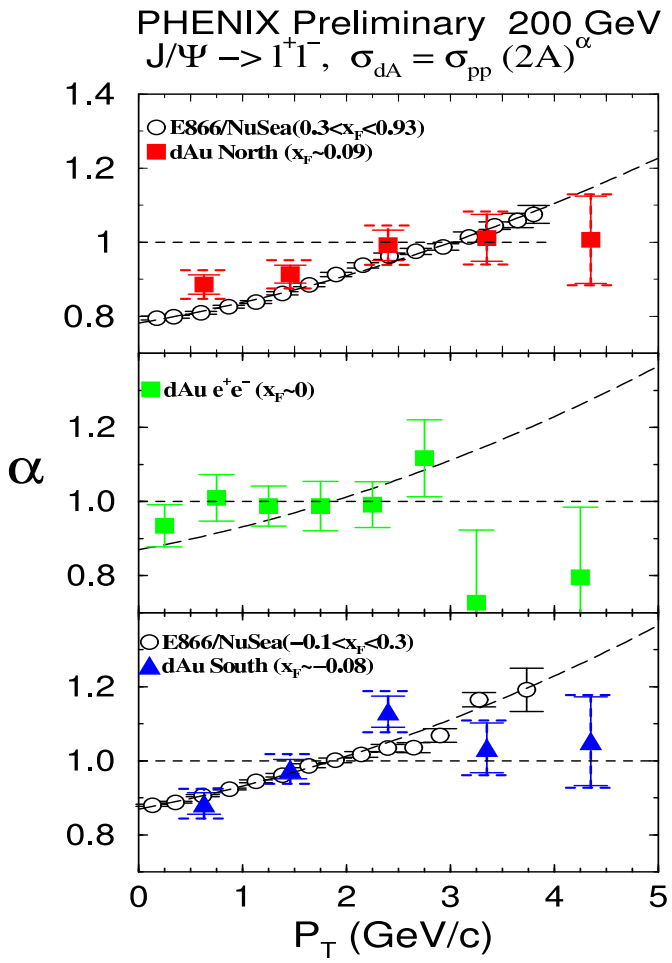

Figure 4.10 α parameter(defined as $\sigma_{dA} = \sigma_{pp} \times (2A)^{\alpha}$) versus p_T compared to lower energy measurements.

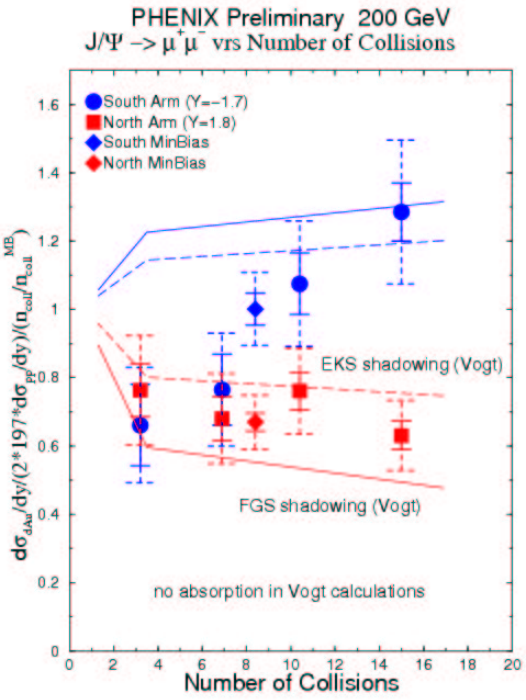

Figure 4.11 Nuclear modification factor versus number of collisions : Ratio of per nucleon cross sections versus centra lity as indicated by number of collisions. Solid error bars represent statistical + point-to-point systematics, while the dashed error bars include arm-to-arm errors. A global 13.4 % error bar is not displayed (see tables 3.14, 3.16 and section 3.5).

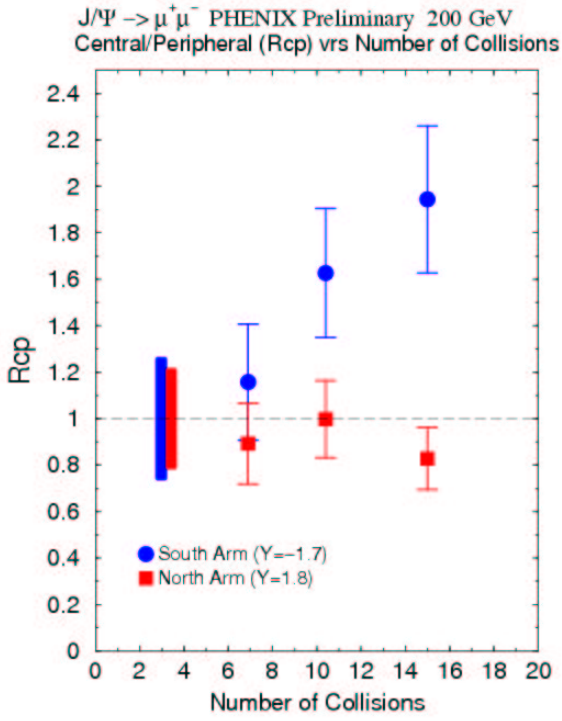

Figure 4.12 Ratio of cross sections between J/ψ's from more central bins in centrality and the most peripheral bin versus number of collisions. Solid error bars represent statistical + point-to-point systematics, while the dashed error bars include arm-to-arm errors. There is no global error since it cancels in the peripheral/central ratio (see tables 3.14, 3.16 and section 3.5).

Chapter 5

Conclusion

Measurements of J/ψ mesons in p+p and d+Au collisions at RHIC provide useful information on both the perturbative and non-perturbative aspects of QCD. They also play crucial roles in both QGP searches and spin studies expected at RHIC. In addition to their connection to Au+Au collision, d+Au measurement is crucial to understand cold nuclear matter effects such as gluon shadowing, transverse momentum broadening, parton energy loss or absorption.

The first $pp \to J/\psi + X$ measurements from RHIC is obtained at $\sqrt{s} =$ 200 GeV with run-II data. The transverse momentum distributions above 2 GeV/c are reasonably well described by the Color Octant Model(COM). The p_T distributions for $J/\psi \to e^+e^-$ and $J/\psi \to \mu^+\mu^-$ are shown in Fig. 4.1 together with predictions [172] from the COM. Predictions of the Color Singlet Model(CSM), which greatly underpredicts the cross sections, are also shown. These predictions are limited to $p_T > 2$ GeV/c because parton intrinsic transverse momentum (k_T) broadening is not accounted properly in the calculation. The COM calculations do not include fragmentation contributions, which become important at around 5 GeV/c [160]. From the phenomenological fits covering all p_T, $\langle p_T \rangle$ values of 1.85 $\pm$ 0.46(stat) $\pm$ 0.16(sys) GeV/c (central arm) and 1.78 $\pm$ 0.27(stat) $\pm$ 0.16(sys) GeV/c (muon arm), with a combined value of 1.80 $\pm$ 0.23(stat) $\pm$ 0.16(sys) GeV/c are obtained.

The J/ψ rapidity distribution obtained by combining the dielectron and

dimuon measurements is shown in Fig. 4.2, with the muon arm data divided into two rapidity bins. The COM curves are theoretical shape predictions [166] using the same models as are discussed in connection with Fig. 4.4b, except that they are normalized to our data to make the shape comparison clearer. Since gluon fusion is the dominant process in all of the models, the rapidity shape depends mostly on the gluon distribution function and is not very sensitive to the production model. Most of the available PDFs are consistent with the data, and improved statistical precision will be needed to constrain them. A PYTHIA calculation that reproduces the shape of our data best is also shown in Fig. 4.2. The total cross section was determined to be $3.99 \pm 0.61(\text{stat}) \pm 0.58(\text{sys}) \pm 0.40(\text{abs})$ μb from the fit of the rapidity distribution. COM calculations are able to reproduce the $\sqrt{s}$ dependence of the cross section using color octet matrix elements found in the literature, with a reasonable choice of QCD parameters. The new run-III p+p results at the same energy with the improved RHIC luminosity, muon tracker acceptance improvement and more precise MuID efficiency calculation are consistent with the run-II results within the statistical and systematic errors and used to study the nuclear modification factor in d+Au collisions.

The PHENIX experiment was able to measure J/ψ production at forward, backward and central rapidities in d+Au collisions. The ratio of J/ψ production in d+Au collisions to p+p collisions, as a function of rapidity is shown in Fig. 4.7, along with few theoretical predictions. The shape is consistent with shadowing at low x and less suppression at larger x. The p_T differential cross section shapes exhibit broadening which comparable with the results from the $\sqrt{s_{NN}} = 38$ GeV lower energy experiment E866/NuSea [18] which is shown in Fig. 4.9. Also centrality dependence has been studied. At forward rapidity (small x values in the gold nucleus, or the shadowing region), no strong dependence is observed, while a strong enhancement from peripheral to central collisions is observed at backward rapidity. The theoretical curves on figure 4.11 correspond to different amounts of inhomogeneous shadowing and antishadowing at these rapidities from [19]. The predictions are qualitatively consistent with the data at forward rapidity, while they do not show the observed steep rising shape at backward rapidity. For now, there is no interpretation to this unexpected behavior. It

might be a evidence in favor of Color Glass Condensate(whose theoretical overview with some experimental results is discussed in section1.3) in our backward rapidity region.

Chapter 6

Outlook

The J/ψ production is one of the most celebrated and also earliest signatures of deconfinement [1] that has provided one of the most exciting results of the SPS program. The story culminated with the observation by the NA50 experiment of an anomalous suppression of J/ψ in central Pb-Pb collisions at 158 A GeV [2]. The suppression is of the order of 25% with respect to the normal suppression in nuclear matter and it prompted the authors to claim that "the J/ψ suppression pattern observed in our data provides significant evidence for deconfinement of quarks and gluons in the Pb-Pb collisions probed by NA50". This is the only claim in the refereed literature of QGP discovery.

The theoretical expectations at RHIC energies are not at all clear and range from total suppression in the traditional Debye screening scenario to enhancement if $c\overline{c}$ pairs are copiously produced such that J/ψ could be formed by the coalescence of uncorrelated c and $\overline{c}$ quarks [82](which is discussed in the section 1.2.5). The latter scenario seems disfavored from our very limited data set of run 2, but this needs to be confirmed by the much larger data set of run 4.

PHENIX has unprecedented capabilities for the study of the J/ψ in Au-Au collisions. The J/ψ can be measured via its $\mu^+\mu^-$ decay channel at forward and backward rapidities in the muon spectrometers and via its e^+e^- decay channel at mid-rapidity in the central arm spectrometers. The clear J/ψ signal has been reconstructed from the central arm which is shown in

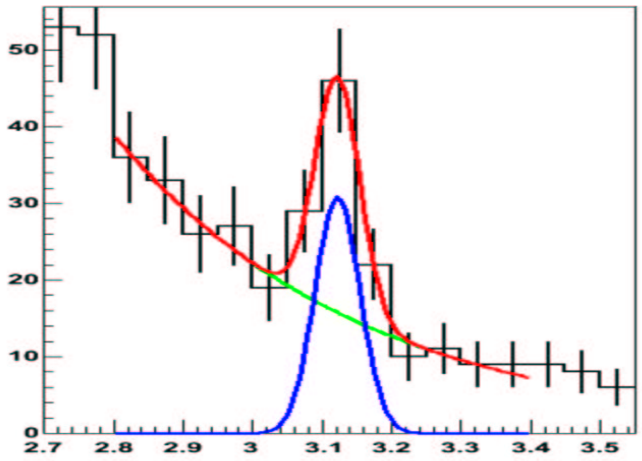

Figure 6.1 The J/ψ signal from run 4 AuAu collision via its e^+e^- decay channel at mid-rapidity in the central arm spectrometers.

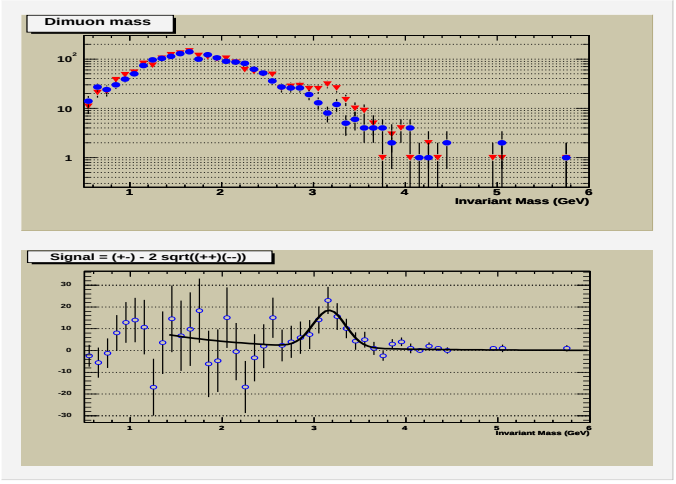

Figure 6.2 The J/ψ signal from run 4 AuAu collision via its $\mu^+\mu^-$ decay channel at forward and backward rapidities in the muon spectrometers.

Fig.6.1 and from the muon arm in Fig.6.2 with small fraction of run 4 data set. From the recorded luminosity of run 4, we expect 2000 and 700 J/ψs in the muon and central arms, respectively. This data set will allow us to look at the J/ψ production pattern in Au-Au collisions at RHIC. However, it might be marginal for a complete characterization as function of centrality and p_t. Further higher luminosity runs will be needed for that. Also the pp and dAu baseline measurements performed in runs 2 or 3 have large uncertainties, and higher statistics runs will be needed. A high luminosity pp run is planned for run 5 and a high luminosity dAu or pAu is still to be scheduled in the next years. As shown in Fig.6.3, the RHIC performance is getting better recently, it is a very promising factor to get more data in the future.

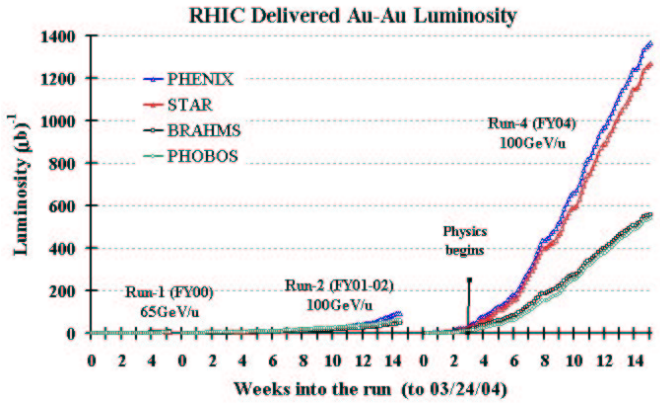

Figure 6.3 The very sharp rise in the luminosity of the gold-ion beam collisions delivered to the four experiments PHENIX, STAR, BRAHMS, and PHOBOS at the Relativistic Heavy Ion Collider, during the run of fiscal year (FY) 2004, and in contrast to the runs of FY 2001-02 and FY 2000. In FY 2000 beams collided at 65 GeV/u (100 billion electron-volt per nucleon), in the later two runs at 100 GeV/u.

The event distribution as a function of x_F, p_T and x_2 for approximately 15,000 J/ψs reconstructed for the two muon arms and about 2,000 J/ψs in the central arm are shown in Fig. 6.4. This corresponds to an integrated

d+Au luminosity of approximately $20nb^{-1}$. The coverage in p_T and x_2 is quite broad, allowing a detailed study of the J/ψ production as a function of these variables. Of course the level of statistical precision needed in a p+A run for J/ψ observables should match or exceed the levels that will be achieved in the corresponding Au+Au or p+p runs.

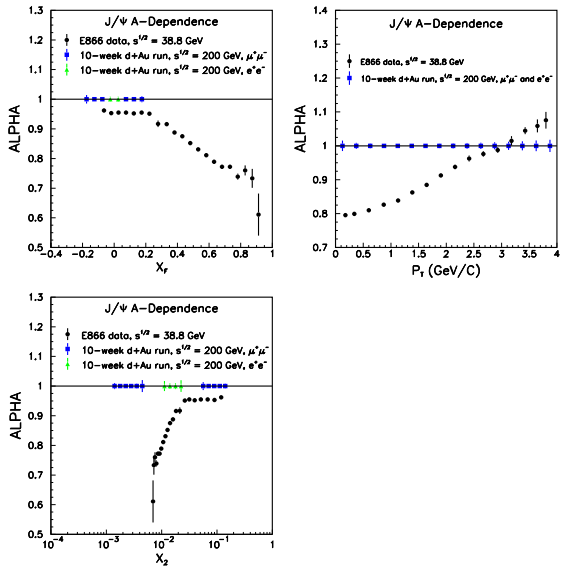

Figure 6.4 Expected statistical precision for measuring the nuclear dependence parameter α from a 20 nb^{-1} d+Au run at PHENIX. Data from a fixed-target experiment at $\sqrt{s} = 38.8$GeV

Appendix

Appendix A The J/ψ

The J/ψ is an hadronic resonance. It was discovered in 1974 simultaneously at the Brookhaven national Laboratory(BNL) and the Sandford Linear Accelerator Center(SLAC). Hence the two names; it was christened J at BNL and ψ at SLAC.

It is a bound state of charm and anti-charm quarks in a 1S triplet state with mass 3096.87 +- 0.04MeV. It is very stable because it cannot decay into charmed mesons because of energy conservation.

The $c\bar{c}$ states form a wide spectrum of bound states with different quantum numbers. So the ψ named $\psi_\prime$ and the X(1P) states that are called X_c in the paper are important.

The characteristics of the charmonium bound states and their main decay modes are shown in Table A.1.

Appendix B Estimation of various contributions to the inclusive J/ψ yield

J/ψ mesons can be produced either directly or via decays from higher state charmonia (χ_c and ψ') as well as from b-quarks. Our measurement is inclusive and it is not possible to separate each contribution from others. We will estimate fractions of each contribution taking into account results of both higher and lower energy experiments.

Resonance	Mass (MeV)	Full width (MeV)	Decay	Branching ratios (%)
J/ψ	3096.87 ± 0.04	0.087± 0.005	hadrons	87.7 ± 0.5
			e^+e^-	5.93 ± 0.10
			$\mu^+\mu^-$	5.88 ± 0.10
ψ'	3685.96 ± 0.09	0.300 ± 0.025	hadrons	98.10± 0.30
			e^+e^-	0.73 ± 0.04
			$\mu^+\mu^-$	0.70 ± 0.09
			J/ψ + X	55.7 ± 2.6
χ_{c0}	3415.0 ± 0.8	14.9 ± 2.6	$J/\psi + \gamma$	0.66 ± 0.18
χ_{c1}	3510.51± 0.12	0.92 ± 0.13	$J/\psi + \gamma$	31.6 ± 3.2
χ_{c2}	3556.18± 0.13	2.08 ± 0.17	$J/\psi + \gamma$	18.7 ± 2.0

Table A.1 Characteristics of the charmonium bound states and their main decay modes.

b-quarks

Contribution from b-quark decays is energy-dependent. Production cross section for a $b\bar{b}$ pair times the branching fraction for a b (or $\bar{b}$)-quark decaying into a J/ψ meson in p (or $\bar{\text{p}}$)+N collisions $\sigma(\text{p}(\bar{\text{p}})\text{N} \to b\bar{b}X)Br(b\bar{b} \to J/\psi X)$ has been measured in p+Au collisions at $\sqrt{s} = 38.8$ GeV by the FNAL-E789 experiment [115] and the result is 148 ± 34 (stat.) ± 28 (syst.) pb/nucleon. It has been also measured in p+$\bar{\text{p}}$ collisions at $\sqrt{s} = 630$ GeV by the CERN-UA1 experiment [121] and 32.7 ± 2.6 (stat.) ± 13.4 (syst.) nb has been obtained with $p_T^{J/\psi} > 5$ GeV/c and $|y^{J/\psi}|$ <2.0 cuts. The ratio of those results is consistent with a perturbative QCD prediction using PYTHIA. It is extrapolated to $\sqrt{s} = 200$ GeV and $\sigma(\text{p+p} \to b\bar{b}X)Br(b\bar{b} \to J/\psi X) =$ 40 nb is obtained which is about 1% of our inclusive result.

ψ'

Production cross sections for ψ', or ψ (2S) mesons, have been also measured by the FNAL-E789 [115] experiment. The relative production cross section times the branching fraction to a muon pair for a ψ' to that for a J/ψ,

$R \equiv Br(\psi' \rightarrow \mu^+\mu^-)\sigma_{\psi'}/Br(J/\psi \rightarrow \mu^+\mu^-)\sigma_{J/\psi} = 0.018 \pm 0.001$ (stat.) $\pm$ 0.002 (syst.) has been obtained. This ψ' fraction can contribute to our J/ψ measurement because of the poor mass-resolution (200 to 300 MeV/c^2) currently observed. Using the branching fractions $Br(\psi' \rightarrow \mu^+\mu^-) = (7.0 \pm 0.9) \times 10^{-3}$ and $Br(J/\psi \rightarrow \mu^+\mu^-) = 5.88 \pm 0.10$ % [139], $\sigma_{\psi'}/\sigma_{J/\psi}$ is determined to be 0.15 $\pm$ 0.03. Contribution of $\psi' \rightarrow J/\psi \rightarrow \mu^+\mu^-$ to inclusive J/ψ yield is therefore expected to 15% $\times$ 0.55 ($Br(\psi' \rightarrow J/\psi X)$) $\sim$ 8%. The color evaporation model expects energy and process independence of the fractions of ψ' and χ_c to the inclusive J/ψ yield. Slightly higher or consistent R values have been obtained by the UA1 ($R = 0.029 \pm 0.010$ (stat.) $\pm$ 0.007 (syst.) with $p_T > 5$ GeV/c and $|y| < 2.0$ cuts) [121] and CDF ($R = 0.033 \pm 0.002$ (stat.) $^{+0.007}_{-0.008}$ (syst.) nb with $p_T > 5$ GeV/c and $|\eta| < 0.6$ cuts) [122] experiments.

χ_c

The fraction of the inclusive J/ψ yield from radiative χ decays has been determined to be (30 $\pm$ 4) % by the FNAL-E705 experiment in p+Li collisions at $\sqrt{s} = 23.8$ GeV [110]. A consistent value, (29.7 $\pm$ 1.7 (stat.) $\pm$ 5.7 (syst.))% was obtained in p+$\bar{\text{p}}$ collisions at $\sqrt{s} = 1.8$ TeV by the CDF experiment at Fermilab [123].

In summary, the fractions of b-quark, ψ' and χ contributions to inclusive J/ψ yield at RHIC energy are expected to be 1%, 10-15% and 30% respectively. The remains are ascribed to the direct production. The fractions of ψ' and χ_c contributions do not agree with the color-singlet model prediction. Including color-octet contributions, they are successfully explained [100]. The color-evaporation model can not predict their fractions. However, small $\sqrt{s}$ dependence of them in nucleon-nucleon collisions is consistent with its assumption that they are process-independent.

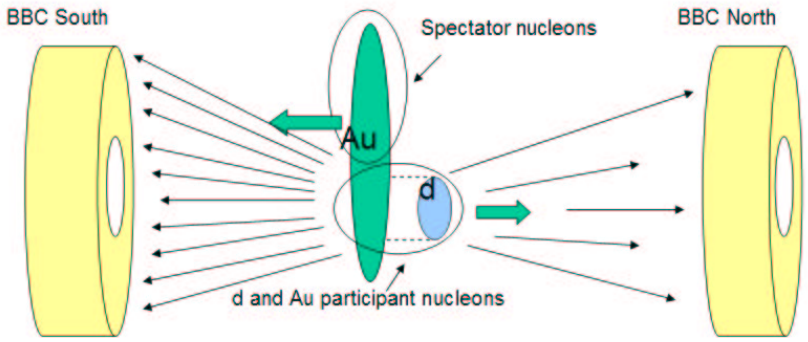

Figure C.1 The cartoon of the d+Au collision

Appendix C Centrality determination for d+Au collisions

A deuteron is a loosely bound system of one neutron and one proton. It's binding energy is only 2.24 MeV, thus the size of the deuteron is large. From the wave function from Hulthen [181], one obtains the following probability distribution for r_{np}

$$P_d(r_{pn}) = \frac{2\alpha\beta(\alpha+\beta)}{(\alpha-\beta)^2}(e^{-2\alpha r_{pn}} + e^{-2\beta r_{pn}} - 2e^{-2(\alpha+\beta)r_{pn}}). \quad \text{(C.1)}$$

with $\alpha = 0.228fm^{-1}$ and $\beta = 1.18fm^{-1}$, where r_{np} is the distance between the proton and the neutron. The distance distribution r_{np} and the momentum distribution of nucleons inside the deuteron is shown in Fig.C.2.

The BBC trigger efficiency for events with is found to be 88% $\pm$ 1%. This efficiency is lower than that in Au+Au collisions due to a smaller dN/dy in the BBC acceptance in d+Au collisions. The centrality selection techniques [179, 183] are different from those used for Au+Au collisions. Only the south BBC (BBCS)(Au ions go towards south) is used to define the centrality selection(see the cartoon in Fig.C.1). The same Glauber code

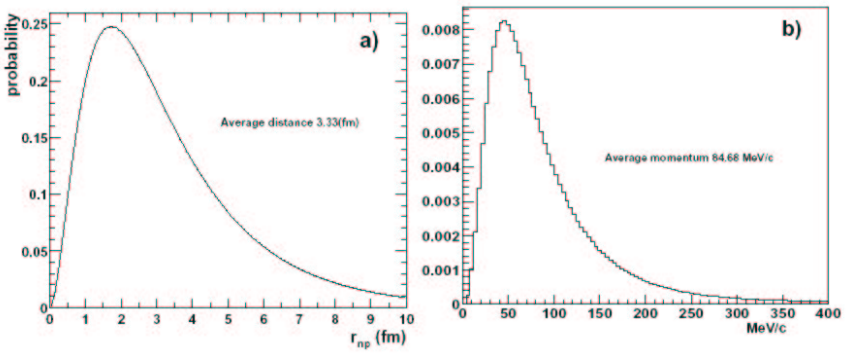

Figure C.2 a) Distance distribution between the neutron and the proton inside a deuteron. b) The momentum distribution of the nucleons inside a deuterons [182]

as for Au is used to determine the number of participants in the gold nucleus. The following assumptions are made about the BBCS response [180]:

- The number of hits in the BBCS (NBBCS hits) follows a Negative Binomial Distribution (NBD) given by the formula,

$$P(n,\mu,k) = \frac{\Gamma(n+k)}{\Gamma(k)n!}\frac{(\mu/k)^n}{(1+\mu/k)^{n+k}} \tag{C.2}$$

  where μ is NBBCS hits for one participant, k is related to the width of the distribution by $(\sigma/\mu)^2 = 1/k + 1/\mu$.

- The observed NBBCS hits is proportional to the number of participants in the Au ion, $\mu \propto N_{part}^{Au}$.

Since both N_{part}^{Au} and the BBC multiplicity are small, the NBD distribution is necessary in order to taken into account the event-by-event fluctuation. The centrality classes are defined by slicing the NBBCS hits distribution into bins containing equal number of events. Each bin is then assigned a percentage range within [0-88%], where 88% is the overall BBC trigger efficiency. These bins are then grouped to form larger centrality bins. Fig.C.3

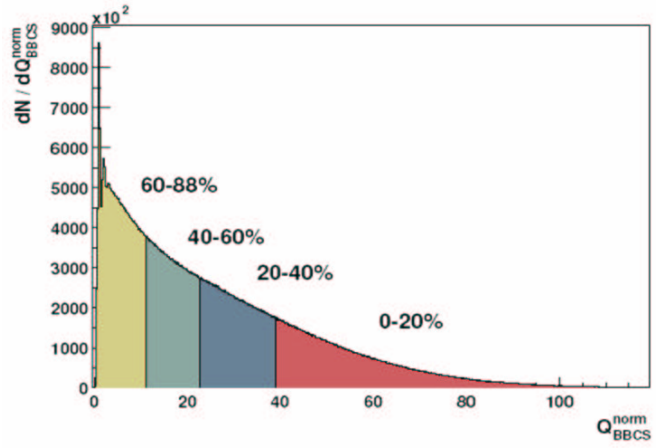

Figure C.3 The four centrality classes used in the d+Au analysis

shows the BBCS multiplicity distribution for the 4 centrality classes used in the d+Au analysis.

For each centrality class, the corresponding N_{part}^{Au} and N_{coll} are determined from the Glauber simulation. The procedure is the following: i) For a collision with a given impact parameter, N_{part}^{Au} and N_{coll} are calculated in the Glauber model. The corresponding number of BBC hits is calculated according to a NBD distribution with parameters $\mu x N_{part}^{Au}$ and $k x N_{part}^{Au}$. ii) The simulated BBCS hit distribution is then fitted to the data to obtain the coefficients μ and k. iii) Combined with the Glauber model, these μ and k values are then used to determine $< N_{part} >$ and $< N_{coll} >$. An example of the NBD distribution from simulation and the number of hits in BBCS from data for different number of PC1 hits is shown in Fig.C.4. PC1 is used as a simple way to select centrality for real data. The measured distribution is broader than the simulated distribution due to additional fluctuations from the PC1, but the general trend agrees very well.

The simulated NBD distributions are then fitted to the data. FigC.5 shows the fit to the BBCS hits distribution for minimum bias collisions. The general agreement is good. However, the simulated NBD distribution is above the data for a small BBCS signal. This difference indicates an

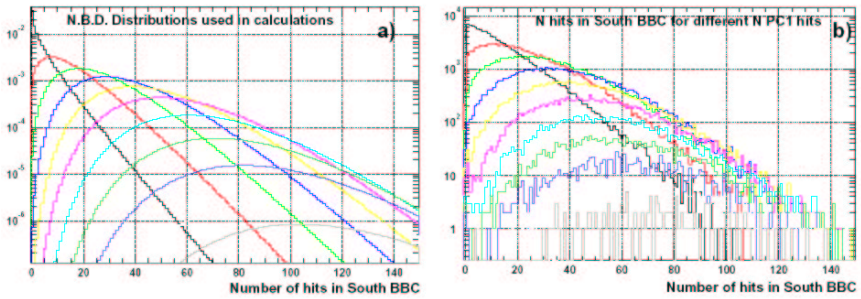

Figure C.4 a) NBD distribution for BBC south hits from simulation. b) The BBC south hit distribution from real data, different curves represents events with different number of PC1 hits from real data.

inefficiency of the BBCS for events with small multiplicities. By dividing the data by the simulated NBBCS hits distribution, we obtained the BBC efficiency as function of NBBCS hits . This is shown in Fig.C.6a. Since for each NBBCS hits value, we have a number for N_{coll} from the Glauber simulation, the efficiency can also be plotted as function of N_{coll}. This is shown in Fig.C.6b.

For $N_{coll} = 1$, the efficiency is equal to 57% which is close to 52% measured in p+p collisions [178]. This efficiency distribution results into an 88.5% efficiency for minimum bias spectra with $< N_{coll} > = 8.4$, consistent with the efficiency value obtained in [183]. The NBD distributions as function of N_{coll} for the centrality classes defined in Fig.C.3 are then plotted in Fig.C.7.

Centrality	$< N_{coll} >$	Ratio to most peripheral bin	Bias correction
0-88	8.5±0.4	-	> 0.99
0-20	15±1	4.6±0.5	> 0.99
20-48	10.4±1.7	3.2±0.2	> 0.99
40-68	6.9±0.6	2.1±0.1	0.974±0.01
60-88	3.2±0.3	1.0	0.885±0.04

Table C.1 $< N_{coll} >$,it's error and BBC trigger bias for minimum bias collisions for the four centrality bin shown in Fig.C.3.

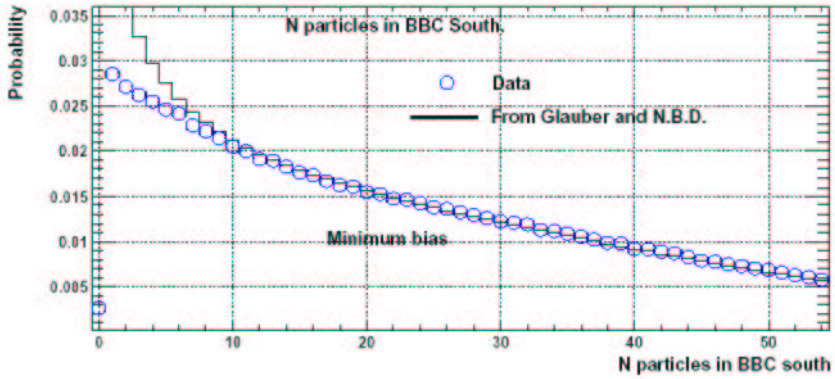

Figure C.5 Results of NBD fits to BBC south charges for minimum bias data.

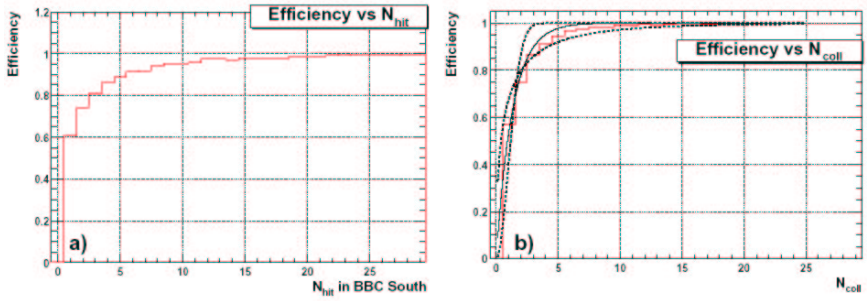

Figure C.6 a) Minimum bias trigger efficiency given by measured over calculated N_{hits}^{BBCS} distribution. b) Efficiency as a function of N_{coll}.

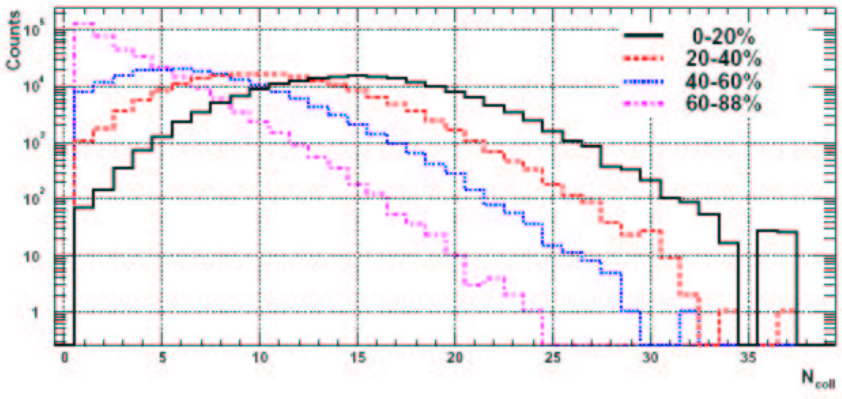

Figure C.7 N_{coll} distributions for different centrality classes.

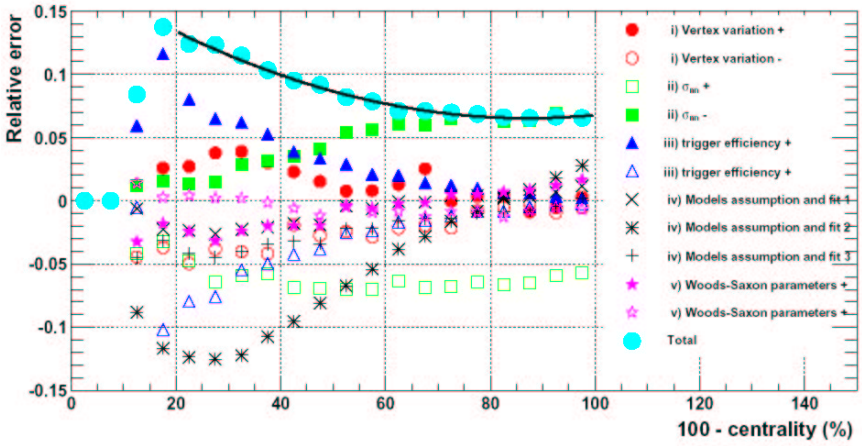

Figure C.8 Relative errors introduced by different systematic errors as function of centrality for most peripheral(left panel) and for most central(right panel) collisions.

The final values for all centrality classes used in the d+Au analysis are summarized in TableC.1. The system- atic error quoted comes from i) vertex dependence of the BBCS trigger efficiency, ii) dependence on nucleon cross section, σ_{nn}, iii) centrality dependence of the BBCS trigger efficiency, iv) model assumptions and NBD fits, and v) variation of Woods-Saxon parameters [179, 180]. The results of the systematic variations are shown in Fig.C.8. The solid line shows the sum of all different types of variations. Finally, the Glauber model also determines the total cross section in d+Au collisions [183] to be

$$\sigma_{dAu}^{total} = 2.25 \pm 0.1b \tag{C.3}$$

assuming an N+N cross section of $\sigma_{nn} = 42mb$. In peripheral d+Au collisions, events with the same N_{coll} can have very different multiplicity. This event-by-event fluctuation of the number of charged tracks in the BBC acceptance leads to a trigger bias, where events with the same N_{coll} but larger multiplicity have a higher probability to be triggered by the BBCS. This bias effect was first studied in p+p collisions using high pT π^0 triggers (ERT trigger) [177]. It triggers on the events with high p_T photons from $\pi^0 \to \gamma\gamma$ decays independent of the BBC trigger decision. It was found that the BBC triggers on $e_{trig}^{BBC} \sim 50$ % of of the inelastic collisions, but these collisions include a higher fraction ($e_{\pi^0}^{BBC} \sim 75$ of the events for which a π^0 is detected by the ERT trigger. $e_{\pi^0}^{BBC}$ was found to be constant at pT ¿ 1.5 GeV/c, and slightly decreases towards lower p_T . A similar study was performed later for charged hadrons. The efficiency of the BBC trigger for charged hadrons ($e_{h^\pm}^{BBC}$) was found to be almost identical to that for π^0s. Fig.C.9 shows the efficiency of the BBC trigger for π^0(left) and $h^+ + h^-$(right) in the central arms. The correction factor for the p+p case, where $N_{coll} = 1$, is simply,

$$c1 = \frac{e_{trig}^{BBC}}{e_{h^\pm}^{BBC}} = \frac{0.5}{0.75} = 0.667 \tag{C.4}$$

For the case where $N_{coll} =$ n, the BBC trigger efficiency can be calculated according to simple binomial statistics. The efficiency of the BBC trigger for inelastic collisions is $1 - (1 - e_{trig}^{BBC})^n$, and the efficiency for charged hadrons is $1 - (1 - e_{h^\pm}^{BBC})(1 - e_{trig}^{BBC})^n$ The correction factor then is,

$$c_n = \frac{1 - (1 - e_{trig}^{BBC})^n}{1 - (1 - e_{h^\pm}^{BBC})(1 - e_{trig}^{BBC})^n} \tag{C.5}$$

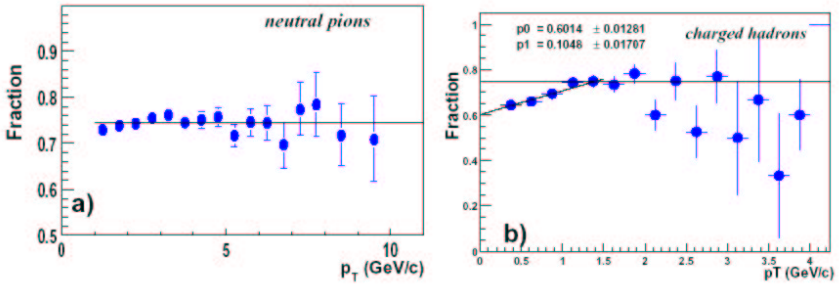

Figure C.9 Efficiency of the BBC trigger for π^0(left) [195] and charged hadrons(right).

The final correction for a given centrality class is calculated as the weighted average from the N_{coll} distribution in Fig.C.7, with the weight given by Eq.C.5. The calculated correction values for all centrality classes are shown in the last column of Table.3.10.

Bibliography

[1] T. Matsui and H. Satz, Phys. Lett. B**178**, 416 (1986).

[2] NA50 collaboration, Phys. Lett. B 477 (2000) 28.

[3] M.C. Abreu et al.(NA50), Phys.Lett.B477,28(2000)

[4] A. Ali Khan et al. (CP-PACS), *Equation of state in finite temperature QCD with two flavors of improved Wilson quarks*, hep-lat/0103028.

[5] P.F.Kolb, nucl-th/0304036

[6] Helmut Satz hep-th/9706342

[7] M.C.Abreu et al. Nucl.Phys. A 610(1996) 331c.

[8] J.D. Bjorken, Phys. Rev. D27(1983) 140.

[9] T.Alber et al. Phys. Rev. Lett.75,21(1995) 3814.

[10] F.Karsh, Nucl. Phys. B 83-84(2000) 14.

[11] R.J Glauber "High Energy Collision Theory" in Lectures in Theoretical Physics vol.1 W.E. Brittin and L.G. Duham(eds.) Interscience. New York,1959

[12] V.A. Abramovsky, V.N Gribov and O.V.Kancheli, Yad.Fiz. 18, 595(1973)[Sov J.Nucl.Phys. 18,308(1973)]

[13] V.N. Gribov, Sov. Phys. JETP 29,483(1969)

[14] D.Kharzeev and M. Nardi, Phys. Lett. B 507(2001) 121, hep-ph/0012025

[15] D.Kharzeev and E. Levin Phys. Lett. B523(2001) 79, hep-th/0108006

[16] A.Bialas, M.Bleszynski and W. Czyz, Nucl. Phys. B 111(1976) 461

[17] U. Heinz, Nucl. Phys. A610 (1996) 264c

[18] E866/NuSea collaboration, Phys. Rev. Lett. 84 (2000) 3256.

[19] S.R. Klein and R. Vogt, Phys. Rev. Lett. 91 (2003) 142301.

[20] B. Kopeliovich, A. Tarasov and J. Hufner, Nucl. Phys. A696 (2001) 669-714.

[21] K.J. Eskola, V.J. Kolhinen and P.V. Ruuskanen, Nucl. Phys. **B535** (1998) 351.

[22] K.J. Eskola, V.J. Kolhinen and C.A. Salgado, Eur. Phys. J. **C9** (1999) 61.

[23] L. Frankfurt and M. Strikman Eur. Phys. J. A5 (1999) 293.306 ,hep-ph/9812322.

[24] L. D. McLerran and R. Venugopalan Phys. Rev. D49 (1994) 2233.2241

[25] A. H. Mueller and J.-W. Qiu Nucl. Phys. B268 (1986) 427.

[26] L. V. Gribov, E. M. Levin and M. G. Ryskin Phys. Rept. 100 (1983) 1.150.

[27] F. Karsch, E. Laermann and A. Peikert, Phys. Lett. **B478**, 447 (2000)

[28] M.L. Mangano, hep-ph/9711337.

[29] E772 *Phys. Rev. Lett.* **66**, 133 (1991).

[30] R. Debbe for BRAHMS collaboration, Quark matter 2004 and DNP 2003.

[31] L. D. McLerran and R. Venugopalan, Phys. Rev. D **49**, 2233 (1994), Phys. Rev. D **49**, 3352 (1994), Phys. Rev. D **59**, 094002 (1999); Y. V. Kovchegov, Phys. Rev. D **54**, 5463 (1996), Phys. Rev. D **55**, 5445 (1997).

[32] L. V. Gribov, E. M. Levin and M. G. Ryskin, Phys. Rept. **100** (1983) 1.

[33] A. H. Mueller and J. W. Qiu, Nucl. Phys. B **268**, 427 (1986).

[34] E. L. Berger *et al.*, in *Proc. of the APS/DPF/DPB Summer Study on the Future of Particle Physics (Snowmass 2001)* ed. N. Graf, eConf **C010630**, P5001 (2001).

[35] D. Kharzeev, E. Levin and M. Nardi, hep-ph/0111315, Nucl. Phys. A **730**, 448 (2004); J. Jalilian-Marian, nucl-th/0212018.

[36] M. Gyulassy and X. N. Wang, Nucl. Phys. B **420**, 583 (1994); M. Gyulassy, I. Vitev and X. N. Wang, Phys. Rev. Lett. **86**, 2537 (2001); X. N. Wang, Phys. Lett. B **579**, 299 (2004); M. Gyulassy, P. Levai and I. Vitev, Phys. Rev. D **66**, 014005 (2002), Nucl. Phys. B **594**, 371 (2001); S. Jeon, J. Jalilian-Marian and I. Sarcevic, Nucl. Phys. A **715**, 795 (2003), Phys. Lett. B **562**, 45 (2003), Nucl. Phys. A **723**, 467 (2003); J. Jalilian-Marian, K. Orginos and I. Sarcevic, Nucl. Phys. A **700**, 523 (2002), Phys. Rev. C **63**, 041901 (2001); A. Kovner and U. A. Wiedemann, hep-ph/0304151; C. A. Salgado and U. A. Wiedemann, Phys. Rev. D **68**, 014008 (2003).

[37] A. Dumitru and J. Jalilian-Marian, Phys. Lett. B **547**, 15 (2002), Phys. Rev. Lett. **89**, 022301 (2002).

[38] D. Kharzeev, Y. V. Kovchegov and K. Tuchin, Phys. Rev. D **68**, 094013 (2003),

[39] J. L. Albacete, N. Armesto, A. Kovner, C. A. Salgado and U. A. Wiedemann, hep-ph/0307179.

[40] J. Jalilian-Marian, Y. Nara and R. Venugopalan, Phys. Lett. B **577**, 54 (2003).

[41] I. Vitev, Phys. Lett. B **562**, 36 (2003); A. Accardi and M. Gyulassy, nucl-th/0308029.

[42] F. Gelis and J. Jalilian-Marian, Phys. Rev. D **66**, 014021 (2002), Phys. Rev. D **66**, 094014 (2002), Phys. Rev. D **67**, 074019 (2003).

[43] B. Z. Kopeliovich, J. Raufeisen, A. V. Tarasov and M. B. Johnson, Phys. Rev. C **67**, 014903 (2003), M. B. Johnson *et al.*, Phys. Rev. C **65**, 025203 (2002), B. Z. Kopeliovich, J. Raufeisen and A. V. Tarasov, Phys. Lett. B **503**, 91 (2001); S. J. Brodsky, A. Hebecker and E. Quack, Phys. Rev. D **55**, 2584 (1997).

[44] M. Gluck, E. Reya and A. Vogt, Eur. Phys. J. C **5**, 461 (1998).

[45] M. Hirai, S. Kumano and M. Miyama, Phys. Rev. D **64**, 034003 (2001).

[46] A. Ayala, J. Jalilian-Marian, L. D. McLerran and R. Venugopalan, Phys. Rev. D **52**, 2935 (1995), Phys. Rev. D **53**, 458 (1996); J. Jalilian-Marian, A. Kovner, A. Leonidov and H. Weigert, Nucl. Phys. B **504**, 415 (1997), Phys. Rev. D **59**, 014014 (1999), Phys. Rev. D **59**, 034007 (1999), [Erratum-ibid. D **59**, 099903 (1999)]; J. Jalilian-Marian, A. Kovner and H. Weigert, Phys. Rev. D **59**, 014015 (1999); A. Kovner, J. G. Milhano and H. Weigert, Phys. Rev. D **62**, 114005 (2000); A. Kovner and J. G. Milhano, Phys. Rev. D **61**, 014012 (2000); E. Iancu, A. Leonidov and L. D. McLerran, Nucl. Phys. A **692**, 583 (2001), hep-ph/0202270, Phys. Lett. B **510**, 133 (2001); E. Iancu and L. D. McLerran, Phys. Lett. B **510**, 145 (2001); E. Ferreiro, E. Iancu, A. Leonidov and L. McLerran, Nucl. Phys. A **703**, 489 (2002); E. Iancu and R. Venugopalan, hep-ph/0303204.

[47] K. Rummukainen and H. Weigert, hep-ph/0309306.

[48] Y. V. Kovchegov, Phys. Rev. D **60**, 034008 (1999), Phys. Rev. D **61**, 074018 (2000); I. Balitsky, Nucl. Phys. B **463**, 99 (1996).

[49] K. Golec-Biernat and A. M. Stasto, Nucl. Phys. B **668**, 345 (2003); E. Gotsman, M. Kozlov, E. Levin, U. Maor and E. Naftali, hep-ph/0401021.

[50] E. Iancu, K. Itakura and S. Munier, hep-ph/0310338.

[51] J. Kwiecinski and A. M. Stasto, Phys. Rev. D **66**, 014013 (2002).

[52] E. Iancu, K. Itakura and L. McLerran, Nucl. Phys. A **708**, 327 (2002), hep-ph/0205198.

[53] K. Golec-Biernat and M. Wusthoff, Phys. Rev. D **59**, 014017 (1999), Phys. Rev. D **60**, 114023 (1999).

[54] A. Freund, K. Rummukainen, H. Weigert and A. Schafer, Phys. Rev. Lett. **90**, 222002 (2003).

[55] J. Jalilian-Marian, work in progress.

[56] A. Kovner, L. D. McLerran and H. Weigert, *Phys. Rev.* **D52**, 6231 (1995); 3809 (1995); A. Krasnitz and R. Venugopalan, *Phys. Rev. Lett* **84**, 4309 (2000); *Nucl. Phys.* **B557**, 237 (1999); A. Krasnitz, Y. Nara and R. Venugopalan, *Phys. Rev. Lett.* **87** , 192302 (2001).

[57] M. Gazdzicki and M.I.Gorenstein,Phys. Rev.Lett.83,4009,4009(1999), hep-ph/9905515

[58] P. Braun-Munzinger and J. Stachel, Nucl. Phys. A690, 119 (2001), nucl-th/0012064.

[59] R. L. Thews, M. Schroedter, and J. Rafelski, Phys. Rev. C63, 054905 (2001), hep-ph/0007323.

[60] L. Grandchamp and R. Rapp, Nucl. Phys. A709, 415 (2002), hep-ph/0205305.

[61] L.Grandchamp and R.Rapp, Nucl.Phys.A709,415(2002),hep-th/0205305

[62] A. Capella, D. Sousa nucl-th/0303055

[63] Shi-yuan Li, Xin-Nian Wang Phys.Lett.B527:85-91,2002, nucl-th/0110075

[64] X.N. Wang and M. Gyulassy, Phys. Rev. Lett. 86(2001) 3496

[65] nucl-th/0305046

[66] S.Gavin and R.Vogt, Nucl.Phys. B345(1990) 104

[67] Topor Pop, V. and others Phys. Rev. C68 2003 054902 nucl-th/0209089

[68] Kharzeev, Dmitri and Nardi, Marzia Phys. Lett.B507 2001 121-128 nucl-th/0012025

[69] Eskola, K. J. and Kajantie, K. and Ruuskanen, P. V. and Tuominen, K Nucl. Phys. B570 2000 379-389 hep-ph/9909456

[70] Eskola, K. J. and Ruuskanen, P. V. and Rasanen, S. S. and Tuominen, K Nucl. Phys. A696 2001 715-728 hep-ph/0104010

[71] R.Vogt, Phys.Lett. B 430(1998) 15

[72] S.Gavin and R.Vogt, Nucl. Phys. A610(1996) 442c

[73] J.P.Blaizot and J.Y.Ollitrault, Phys. Rev. D 39(1989) 232

[74] J.Geiss, Phys.Lett.B 447 (1999) 31

[75] M.C. Abreu et al.Nucl.Phys.A 661(1999) 93c

[76] J.Qiu, J.P.Vary and X.Zhang, hep-ph/9809442

[77] R.C.HWa and J.Pisut,Phys. Rev.C 58(1998) 434

[78] S.S. Adler et al., Phys. Rev. C 69, 014901 (2004). ,nucl-ex/0305030

[79] J. J. Aubert *et al.*, Phys. Rev. Lett. **33**, 1404 (1974).

[80] J. E. Augustin *et al.*, Phys. Rev. Lett. **33**, 1406 (1974).

[81] R. Vogt, Phys. Rept. **310**, 197 (1999).

[82] R.L. Thews *et al.*, Phys. Rev. C**63**, 054905 (2001).

[83] M. J. Alguard *et al.*, Phys. Rev. Lett. **37**, 1258 (1976), M. J. Alguard *et al.*, Phys. Lett. B**206**, 364 (1988), B. Adeva *et al.*, Phys. Lett. B**320**, 400 (1994), D. Adams *et al.*, Phys. Lett. B**329**, 399 (1994), Phys. Lett. B**336**, 125 (1994) and Phys. Lett. B**357**, 248 (1995), P. L. Anthony *et al.*, Phys. Rev. Lett. **71**, 959 (1993).

[84] Ya. S. Derbenev and A. M. Kondratenko, Part. Accel. **8**, 115 (1978).

[85] For example, N. Saito *et al.*, Nucl. Phys. Proc. Suppl. **105**, 47 (2002).

[86] FNAL-E704 experiment. For example, D. L. Adams *et al.*, Phys. Lett. B**261**, 197 (1991).

[87] For example, Y. Goto *et al.*, Nucl. Phys. Proc. Suppl **79**, 588 (1999).

[88] J.C. Collins and D.E. Soper, Ann. Rev. Nucl. Part. Sci. **37**, 383 (1987).

[89] F. Halzen, Phys. Lett. B**69**, 105 (1977).

[90] H. Fritzsch, Phys. Lett. B**67**, 217 (1977).

[91] J. F. Amundson *et al.*, Phys. Lett. B**390**, 323 (1997).

[92] R. Baier and R. Ručkl, Z. Phys. C**19**, 251 (1983).

[93] G. A. Shuler, CERN-TH-7170-94, unpublished.

[94] G. Bodwin, E. Braaten, and G. Lepage, Phys. Rev. D**51**, 1125 (1995).

[95] G. T. Bodwin, E. Braaten and G. P. Lepage, Phys. Rev. D**51**, 1125 (1995).

[96] P. Cho and A. K. Leivovich, Phys. Rev. D**53**, 6203 (1996).

[97] H. Cano-Coloma and M. A. Sanchis-Lazano, Nucl. Phys. B**508**, 753 (1997).

[98] T. Sakuma, Master Thesis (in Japanese), Tokyo Institute of Technology, January, 1999.

[99] S. Gupta and K. Sridhar, Phys. Rev. D**54**, 5545 (1996).

[100] M. Beneke and I. Z. Rothstein, Phys. Rev. D**54**, 2005 (1996).

[101] W.-K. Tang and M. Vänttinen, Phys. Rev. D**54**, 4349 (1996).

[102] S. C. C. Ting, Proc. Int. Symp. on Lepton and Photon Int. at High Energies, Stanford University, Stanford, USA (1975) p.155.

[103] A. Bamberger *et al.*, Nucl. Phys. **B134**, 1 (1978).

[104] M.J. Corden *et al.*, Phys. Lett. B**98**, 220 (1981).

[105] Yu. M. Antipov *et al.*, Phys. Lett. B**60**, 309 (1976).

[106] K. J. Anderson *et al.*, Phys. Rev. Lett. **37**, 799 (1976).

[107] J. Badier *et al.*, Z. Phys. C**20**, 101 (1983).

[108] K.J. Anderson *et al.*, Phys. Rev. Lett. **42**, 944 (1979).

[109] L. Antoniazzi *et al.*, Phys. Rev. D**46**, 4828 (1992).

[110] L. Antoniazzi *et al.*, Phys. Rev. Lett. **70**, 383 (1993).

[111] C. Morel *et al.*, Phys. Lett. B**252**, 505 (1990).

[112] H. D. Snyder *et al.*, Phys. Rev. Lett. **36**, 1415 (1976).

[113] V. Abramov *et al.* FERMILAB-PUB-91/62-E (Unpublished).

[114] M. H. Schub *et al.*, Phys. Rev. D**52**, 1307 (1995), D**53**, 570 (1996).

[115] D. M. Jansen *et al.*, Phys. Rev. Lett. **74**, 3118 (1995).

[116] A. Gribushin *et al.*, Phys. Rev. D**62**, 012001 (2000).

[117] E. Nagy *et al.*, Phys. Lett. B**60**, 96 (1975).

[118] J. H. Cobb *et al.*, Phys. Lett. B**68**, 101 (1977).

[119] C. Kourkoumelis *et al.*, Phys. Lett. B**91**,481 (1980).

[120] T.-H. Chang, Ph.D Thesis, New Mexico State University, July 1999, C. Akerlof *et al.*, Phys. Rev. D**48**, 5067 (1993), A. Gribushin *et al.*, Phys. Rev. D**53**, 4723 (1996), T. Alexopoulos *et al.*, Phys. Rev. D**55**, 3927 (1997), C. Biino *et al.*, Phys. Rev. Lett. **58**, 2523 (1987).

[121] C. Albajar *et al.*, Phys. Lett. B**256**, 112 (1991).

[122] F. Abe *et al.*, Phys. Rev. Lett. **69**, 3704 (1992), Phys. Rev. Lett. **79**, 572 (1997).

[123] F. Abe *et al.*, Phys. Rev. Lett. **79**, 578 (1997).

[124] T. Affolder *et al.*, Phys. Rev. Lett. **85**, 2886 (2000).

[125] S. Abachi *et al.*, Phys. Lett. B**370**, 239 (1996), B. Abbott *et al.*, Phys. Rev. Lett. **82**, 35 (1999).

[126] J. T. Mitchell *et al.*, Nucl. Instr. Meth. A**482**, 498 (2002).

[127] T. C. Awes *et al.*, Submitted to Nucl. Instr. Meth. February 2002.

[128] J. Burward-Hoy, Ph.D Thesis, SUNY Stony Brook, December 2001.

[129] J. Nagle *et al.*, The XVI International Conference on Ultrarelativistic Nucleus-Nucleus Collisions (Quark Matter 2002), to be published in Nucl. Phys. A, NUCL-EX/0209016.

[130] C. Adler, A. Denisov, E. Garcia, M. Murray, H. Strobele and S. White, Nucl. Instr. Meth. A**461**, 337 (2001).

[131] K. Ikematsu *et al.*, Nucl. Instr. Meth. A**411**, 238 (1998).

[132] B. Fox, private communication.

[133] H. Akikawa *et al.*, to be submitted to Nucl. Instr. Meth. A.

[134] H. Sato (H. D. Sato), Master Thesis (in Japanese), Kyoto University, February, 1998.

[135] GEANT User's Guide, 3.15, CERN Program Library.

[136] E. Mathieson, Nucl. Instr. Meth. A**270**, 602 (1988).

[137] R. Kalman, Trans. ASME D**82**, 35 (1960), P. Billoir, Nucl. Instr. Meth. **225**, 352 (1984), P. Billoir, R. Fruhwirth and M. Regler, Nucl. Instr. Meth A**241**, 115 (1985), P. Billoir and S. Qian, Nucl. Instr. Meth. A**294**, 219 (1990), P. Billoir and S. Qian, Nucl. Instr. Meth. A**295**, 492 (1990), D. Stampfer, M. Regler and R. Fruhwirth, Comput. Phys. Commun. **79**, 157 (1994), M. Regler, R. Fruhwirth and W. Mitaroff, J. Phys. G G22, 521 (1996).

[138] T. Sjöstrand, Comp. Phys. Comm. **82**, 74 (1994).

[139] K. Hagiwara *et al.*, Phys. Rev. D**66**, 010001 (2002).

[140] C. Albajar *et al.*, Nucl. Phys. B**335**, 261 (1990).

[141] H. Torii *et al.* (PHENIX Collaboration), NUCL-EX/0210005, to be published in Nucl. Phys. A.

[142] G. J. Alner *et al.*, Z. Phys. C**33**, 1 (1986).

[143] R. V. Gavai *et al.*, Int. J. Mod. Phys. A**10**, 2999 (1995).

[144] H.-L. Lai and H.-n. Li, Phys. Rev. D**58**, 114020 (1998).

[145] B. Cox and P.K.Malhotra, Phys. Rev. D**29**, 63 (1984).

[146] W.J. Metcalf *et al.*, Phys. Lett. B91, 275 (1980).

[147] A. S. Ito *et al.*, Phys. Rev. Lett. **47**, 12 (1981).

[148] S. Gupta and P. Mathews, Phys. Rev. D**55**, 7144 (1997).

[149] S. Gupta and H.Satz, Z.Phys. C 55(1992) 391.

[150] A. L. Deshpande, Nucl. Phys. Proc. Suppl. **105**, 178 (2002).

[151] M. Cacciari and M. Krämer, Phys. Rev. Lett. **76**, 4128 (1996).

[152] M. Mangano and A. Petrelli, Phys. Lett. B**352**, 445 (1996).

[153] O. Teryaev and A. Tkabladze, Phys. Rev. D**56**, 7331 (1997).

[154] T. Gehrmann and W.J. Stirling, Phys. Rev. D**53**, 6100 (1996).

[155] L. McLerran, R. Venugopalan, Phys. Rev. D 49 (1994) 2233.

[156] PHENIX collaboration, Phys. Rev. Lett. 92 (2004) 051802.

[157] PHENIX collaboration, Phys. Rev. C 69 (2004) 014901.

[158] R. Vogt, Phys. Repts. **310**, 197 (1999); G A. Schuler, hep-ph/9403387, and references therein.

[159] F. Abe *et al.*, Phys. Rev. Lett. **69**, 3704 (1992); F. Abe *et al.*, Phys. Rev. **D66**, 092001 (2002); S. Abachi *et al.*, Phys. Lett. **B370**, 239 (1996); B. Abbot *et al.*, Phys. Rev. Lett. **82**, 35 (1999).

[160] F. Abe *et al.*, Phys. Rev. Lett. **79**, 572 (1997).

[161] E. Braaten *et al.*, Ann.Rev.Nucl.Part.Sci. **46**, 197 (1996).

[162] G. T. Bodwin *et al.*, Phys. Rev. **D51**, 1125 (1995); erratum Phys. Rev. **D55**, 5853 (1997).

[163] J. F. Amundson *et al.*, Phys. Lett. **B390**, 323 (1997), and private communication.

[164] E. Braaten *et al.*, Phys. Rev. Lett. **71**, 1673 (1993).

[165] K. Adcox *et al.*, Nucl. Instr. Meth. **A499**, 469 (2003).

[166] H. D. Sato, Ph.D Thesis, hep-ph/0305239.

[167] Particle Data Group, Phys. Rev. **D66**, 010001 (2002).

[168] S. S. Adler *et al.*, hep-ex/0304038.

[169] T. Sjöstrand, Comp. Phys. Comm. **135**, 238 (2001).

[170] R. Kephart *et al.*, Phys. Rev. **D14**, 2909 (1976).

[171] T. Affolder *et al.*, Phys. Rev. Lett. **85**, 2886 (2000); E. Braaten *et al.*, Phys. Rev. **D62**, 094005 (2000).

[172] Gouranga C. Nayak *et al.*, hep-ph/0302095.

[173] A. Gribushin *et al.*, Phys. Rev. **D62**, 012001 (2000) and references therein.

[174] M. Beneke and I. Z. Rothstein, Phys. Rev. **D54**, 2005 (1996).

[175] S. S. Adler *et al.*, submitted to Phys. Rev. C, nucl-ex/0305030.

[176] http://pdg.lbl.gov/2002/m070.pdf.

[177] S. Bazilevsky, PHENIX internal analysis note 143 and 176.

[178] S.S. Adler et al., [PHENIX Collaboration], hep-ex/0304038

[179] A. Milov, et al., PHENIX internal analysis note 201.

[180] A. Drees, et al., PHENIX internal analysis note 210.

[181] P.E. Hodgson. Nuclear Reactions and Nuclear Structure. Clarendon Press, Oxford, 1971.

[182] M. Lacombe et al., Phys. Lett. B101, 139 (1981).

[183] K. Homma, PHENIX internal analysis note 211.

[184] D. Morrison, PHENIX internal analysis note 165.

[185] PHENIX Analysis Note 194.

[186] PHENIX Analysis Note 163.

[187] PHENIX Technical Note 395.

[188] http://www.phenix.bnl.gov/phenix/WWW/p/draft/djkim/run3pp/

[189] http://www.phenix.bnl.gov/phenix/WWW/p/draft/silvermy/dAu/

[190] MUID software description reference

[191] PHENIX Technical Note 403, 2003.

[192] H. D. Sato, Kyoto Univ., (PHENIX) Thesis.

[193] PHENIX Analysis Note 209.

[194] PHENIX Analysis Note 210.

[195] http://pdg.lbl.gov/2002/m070.pdf

[196] PHENIX Analysis Note 216.

[197] K. Reygers, private communication.

[198] PHENIX Analysis Note 211.

[199] PHENIX Analysis Note 184.

[200] NUCL-TH/0305046.S.R.Klein, R.Vogt, PRL 91, 142301 (2003).

[201] E866/NuSea: M.J. Leitch et al, PRL 84, 3256 (2000)

[202] NA3: J.Badier et al Z. Phys. C20, 101 (1983)

[203] PHENIX Analysis Note 258. Xie Wei. $J/\psi \to e^+e^-$ analysis in RUN3 d-Au and RUN3 p-p for QM04.

[204] hep-ex/0307019. PHENIX. J/ψ production from proton-proton collisions at sqrt(s) = 200 GeV.

국 문 요 약

d+A 와 p+p 충돌에서의 J/Ψ 생성 메커니즘의 이해

J/Ψ 측정이 RHIC 가속기의 $\sqrt{s}$ = 200 GeV d+Au 와 p+p충돌을 통하여 이루어졌다. J/Ψ입자는 PHENIX 실험에서 뮤온과 전자 검출을 이용하여 측정되어진다. 2003년 RHIC 가속기에서 받은 데이터(d+Au 충돌로부터 2.74 nb^{-1}, p+p 충돌로부터 350 nb^{-1})를 바탕으로 주로 뮤온 붕괴를 통한 J/Ψ입자 검출에 대한 자세한 분석과정이 논문을 통하여 기술된다.

p+p 충돌에서 P_T 2 GeV/c 이상인 J/Ψ 의 P_T 분포는 Color-Octant Model(COM)에 의해서 잘 기술되어진다. J/Ψ의 평균 P_T , $\langle P_T \rangle$ 값은 p+p 충돌에서 1.80 ± 0.23(stat) ± 0.16(sys) GeV/c 로 측정되었다. Differential Cross section이, 뮤온과 전자 붕괴 채널을 통해 측정되어졌고, 이 값들을 fitting 함으로써 Total Cross section, $\sigma_{J/\Psi}$ = 3.99 ± 0.61(stat) ± 0.58(sys) ± 0.40(abs)이 결정되었다. Rapidity 분포는 현재 계산된 모든 Parton Distribution Function(PDF)들로 설명이 가능하며, COM 계산은 타당한 color-octant matrix를 사용함으로 $\sqrt{s}$ 의존성을 잘 보여준다.

p+p 충돌에 대한 d+Au 충돌에서의 J/Ψ 생성의 비가 Rapidity의 함수로 측정되었으며, 작은 x 에서 shadowing 현상을, 큰 x 에서 suppression 이 덜 일어남을 보여준다. Peripheral 충돌에 관한 Central 충돌의 비가 측정되었는데, forward rapidity 영역에서는 강한 centrality 의존성이 보이지 않은 반면, backward rapidity 영역에서는 centrality가 증가함에 따라 그 비가 매우 빠르게 증가함이 관측되었다.

핵심되는 말 : J/Ψ, RHIC 가속기, PHENIX 실험, Color-octant Model, Shadowing